MAGNETIZED PLASMA JETS IN EXPERIMENT AND SIMULATION

A Dissertation

Presented to the Faculty of the Graduate School

of Cornell University

in Partial Fulfillment of the Requirements for the Degree of

Doctor of Philosophy

by

Peter Clark Schrafel

August 2014

MAGNETIZED PLASMA JETS IN EXPERIMENT AND SIMULATION

Peter Clark Schrafel, Ph.D.

Cornell University 2014

Over five years, this experimental campaign has investigated novel configurations of thin aluminum (Al) foils exploded with intense electric current pulses. These experiments allow for the study of the ablation of thin foils and liners, produce extreme conditions possibly relevant to laboratory astrophysics, and aid in computational code validation. They were carried out with Cornell's COBRA pulser, which drives $1\,\mathrm{MA}$ into inductive loads with $100\,\mathrm{ns}$ rise time. In these experiments, Ohmic heating of the foil leads to the production of ablated surface plasma (ASP) around the foil. This ASP ($n_e \sim 10^{24}\,\mathrm{m}^{-3}$) near the foil carries some of the load current and develops an overheating-filamentation instability which leads to the development of many (~ 20) warm ($\sim 10\,\mathrm{eV}$) plasma tendrils near the foil. This work demonstrates that applying a static or slow magnetic field (up to $1.5\,\mathrm{T}$ over $120\,\mu\mathrm{s}$) can deflect or suppress these tendrils which carry currents of $\sim 10\,\mathrm{kA}$. The outflow of ASP (with supersonic axial velocities approaching $300\,\mathrm{km\,s}^{-1}$) also leads to the creation of a strongly collimated hydrodynamic jet (n_e up to $10^{26}\,\mathrm{m}^{-3}$) on the axis of symmetry. In experiments with an applied axial field, this outflow compresses the applied B_z on axis (by a factor of 4 in simulation). Compared to the regular jet, the magnetized jet develops more slowly, has a greater angular divergence, and is hollowed on axis (by an order of magnitude). The jet has a radius $\sim 1\,\mathrm{mm}$ and an axial extent $\sim 25\,\mathrm{mm}$. This jet behavior has been observed with time-gated pinhole extreme-ultraviolet emission imaging and $532\,\mathrm{nm}$ laser interferometry. A spec-

troscopic diagnostic observes Doppler shifts (up to 1 Å) in spectral lines (580 nm C-IV doublet) emitted by carbon-seeded ASP 5 mm above the foil ($n_e \sim 10^{23}$ m^{-3}) which indicates rotation speeds approaching 50 km s^{-1} with a 1 T applied axial field. Results from extended-magnetohydrodynamic simulations with the code PERSEUS closely match the experimental results.

BIOGRAPHICAL SKETCH

Peter Clark Schrafel was born in Mineola, NY. He grew up nearby and attended Garden City High School where his inquisitive nature and desire for orderliness led him to excel in his studies of physics and German. Naturally he pursued an engineering major as an undergraduate. He began working with the Laboratory of Plasma Studies at Cornell University in the summer of 2006. His undergraduate research involved using interferometric methods for studying the plasma surrounding exploding wires. He received his BS in Engineering Physics in 2008 and his MS in Electrical & Computer Engineering in 2012.

For my parents.

ACKNOWLEDGEMENTS

I am very grateful for the useful guidance offered by my special committee: Professors Bruce Kusse, David Hammer, and Richard Lovelace. The support and encouragement of fellow and former graduate students has also been invaluable. Thanks are due to Ryan McBride, Pat Knapp, Matt Martin, David Chalenski, Isaac Blesener, Cad Hoyt, Adam Cahill, Laura Johnson, and Levon Atoyan. Thanks to John Greenly, Sergei Pikuz, and Tania Schelkovenko for their mentorship and many insightful discussions. The highly competent technical staff, Todd Blanchard and Harry Wilhelm, made component fabrication and machine operation go so smoothly. Special thanks go to Kate Blesener for her assistance with optical spectroscopic measurements and to Professor Charles Seyler for his computer simulation work which has been crucial to these experiments. Thanks to Phil DeGrouchy for helpful discussion on Abel inversion concepts.

This work has been financially supported by the Stewardship Sciences Academic Alliances program of the National Nuclear Security Administration and by the National Science Foundation. I am grateful to the responsible entities for giving me the opportunity to spend a significant amount of time learning physics and applying this knowledge in a supportive and hands-on laboratory environment.

Thank you Sarah for your support and patience through many hours of revision.

TABLE OF CONTENTS

LIST OF TABLES

LIST OF FIGURES

LIST OF SYMBOLS

$\mathbf{r}$, $\mathbf{E}$, $\mathbf{B}$	vectors
∇	gradient operator
$\nabla\cdot$	divergence operator
$\nabla\times$	curl operator
e	elementary charge
e	base of the natural logarithm / Euler number
$i(t)$	electric current as a function of time
i	imaginary constant ($\sqrt{-1}$)
m_e	electron mass
n_e	electron number density
ω_{pe}	plasma frequency
$\phi(\mathbf{r}, t)$	phase as a function of position and time
$\mathbf{J}$	electric current density
η	plasma resistivity
k	wavenumber
a	coil radius
N	number of turns
t	time after current onset
t_{LP}	time after long pulse current onset
L	inductance

CHAPTER 1

INTRODUCTION

High energy density physics (HEDP) [6] studies involving exploding radial foils driven by high-current ($\sim$1 MA) pulsed-power machines are of interest for their relevance to: the ablation physics of thin foils and liners, the laboratory study of plasma dynamics comparable (with appropriate scaling [28]) to astrophysical phenomena like jets, and the validation of new computer codes developed to simulate ever-widening swaths of plasma physics. In this context, a *radial foil* is a thin (of order 10 µm), metal disk that makes contact with a current source near the center of the foil and is grounded at an outer annulus. Experiments with radial foils have a history with wire array z-pinches [26], conical wire arrays [1], and radial wire arrays [18].

1.1 Motivation

Apart from producing many pretty pictures, this work is scientifically motivated by three main factors, outlined below.

1.1.1 Ablation Physics

In the early stages of metal foil or liner ablation, small perturbations in density result in different regions of plasma having different conductivities. If the plasma is in a regime where conductivity increases with rising temperatures, this positive feedback leads to the development of discrete paths of enhanced current flow. We will refer to the process that creates these distinct current paths as an electrothermal-filamentation instability. These asymmetric current channels can seed the development of other instabilities like the magneto-Rayleigh-Taylor instability (MRT) [22]. Understanding the origins and development of

these instabilities can lead to better methods for mitigating their undesirable effects.

Basic physics experiments with university-scale pulsed-power devices like Cornell's COBRA (see Chapter 4) are valuable because of the experimental flexibility of these machines compared to massive facilities like Sandia's Z-Machine. Although it cannot produce nearly the same energy densities, COBRA can relatively quickly probe a subset of parameter space that may be relevant to, and that could guide the experimental design of, campaigns on larger devices.

1.1.2 Laboratory Astrophysics

Recent developments in pulsed-power technology have expanded the possibilities for creating laboratory experiments relevant to astrophysical processes. Scaling arguments [7, 8, 15, 36, 27] allow us to make reasonable comparisons between lab-scale and astro-scale plasmas if certain dimensionless parameters are sufficiently similar. Extending the parameter space that laboratory experiments can access increases the likelihood that we can produce results of wide interest.

Jets are of particular interest for their astrophysical ubiquity and dynamic properties. Exploding radial foils provide a fertile playground for exploring jet dynamics.

1.1.3 Computer Simulation

Over the past few decades, the computational capacity for numerical simulations of useful complexity has tremendously increased. Single-fluid magnetohydrodynamics (MHD) models are highly favored for their simplicity and efficiency, although they may leave out important physics in certain situations.

PERSEUS [30], an extended MHD (XMHD) code, retains the Hall term (among others) in Ohm's law, allowing for the accurate simulation of high-density pulsed power loads like wires and foils without invoking artificial vacuum resistivity models. New experiments provide new bases for comparison between physical models and the real thing.

1.2 This Work in Context

There has been much interest in recent years in experiments involving radial foils for the reasons outlined above. Previous investigations on the COBRA [10, 12, 9, 11, 13] and MAGPIE [32, 35] pulsed power generators have provided a wealth of compelling results. Newer configurations involve launching the hydrodynamic jet into an ambient medium [33] or modifying the magnetic field of the experiment with a solenoid in series with the load [34]. Imposing the magnetic field using an independent power supply allows for the study of dynamics in an (initially) uniform background field.

Coupling a slow-rise-time pulsed magnetic field to a fast-rise-time pulsed-power driver is also a topic of great importance and relevance to ongoing magnetized liner inertial fusion (MagLIF) [31] experiments. In this area, issues of interest include the synchronized triggering of multiple pulsed-power devices and the maintenance of magnetic insulation near the load.

1.3 Radial Foils

A short and simplified description of the early-time dynamics of an exploding radial foil is helpful to provide a background for the rest of this dissertation. (See Figure 1.1)

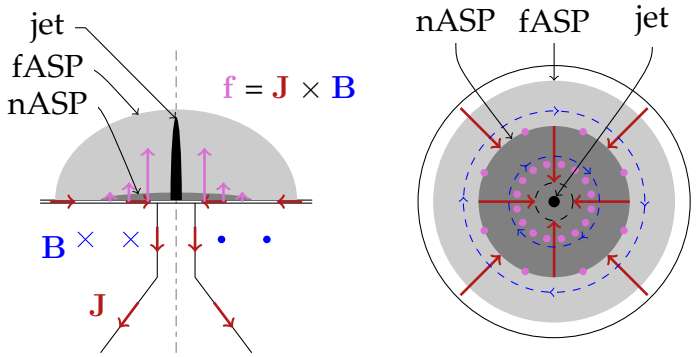

Figure 1.1: A cartoon diagram of a radial foil in the ablation regime. The electric current density (indicated in red) due to the COBRA driver flows radially inward through the foil and then downward when it reaches the central cathode pin. This creates an azimuthal magnetic field (pictured in blue) which is concentrated in the region below the foil. The combined effect of this current and field is an upward $\mathbf{J} \times \mathbf{B}$ force density which falls off as $(\text{distance from the axis})^{-2}$. The nASP, fASP, and jet, as described in Section 1.3, are labelled.

It begins with a room-temperature ($300\,\text{K}$) foil surrounded by high vacuum with particle density $\sim 10^{18}\,\text{m}^{-3}$. The radially inward and axially downward current distribution sets up an azimuthal B_θ which exerts an upward force on radial currents and an inward force on axial currents. As the COBRA current pulse ramps up to $1\,\text{MA}$ over $100\,\text{ns}$, the foil warms up due to Joule heating. The skin depth of the COBRA pulse in aluminum is about $40\,\mu\text{m}$, which is larger than the foil thickness ($20\,\mu\text{m}$). As the metal foil heats up, cooler regions are less resistive [5] and therefore draw more current. This leads to a relatively uniform heating of the foil. Once the full thickness of the foil has melted, significant ablation into the region above the foil is visible via XUV emission imaging. There is likely also ablated plasma on the underside of the foil, but it cannot be directly observed in this experimental configuration. Because of the upward $\mathbf{J} \times \mathbf{B}$ force density experienced by all of the current-carrying material in or adjacent to the foil, the plasma on the underside of the foil is pushed back towards the foil,

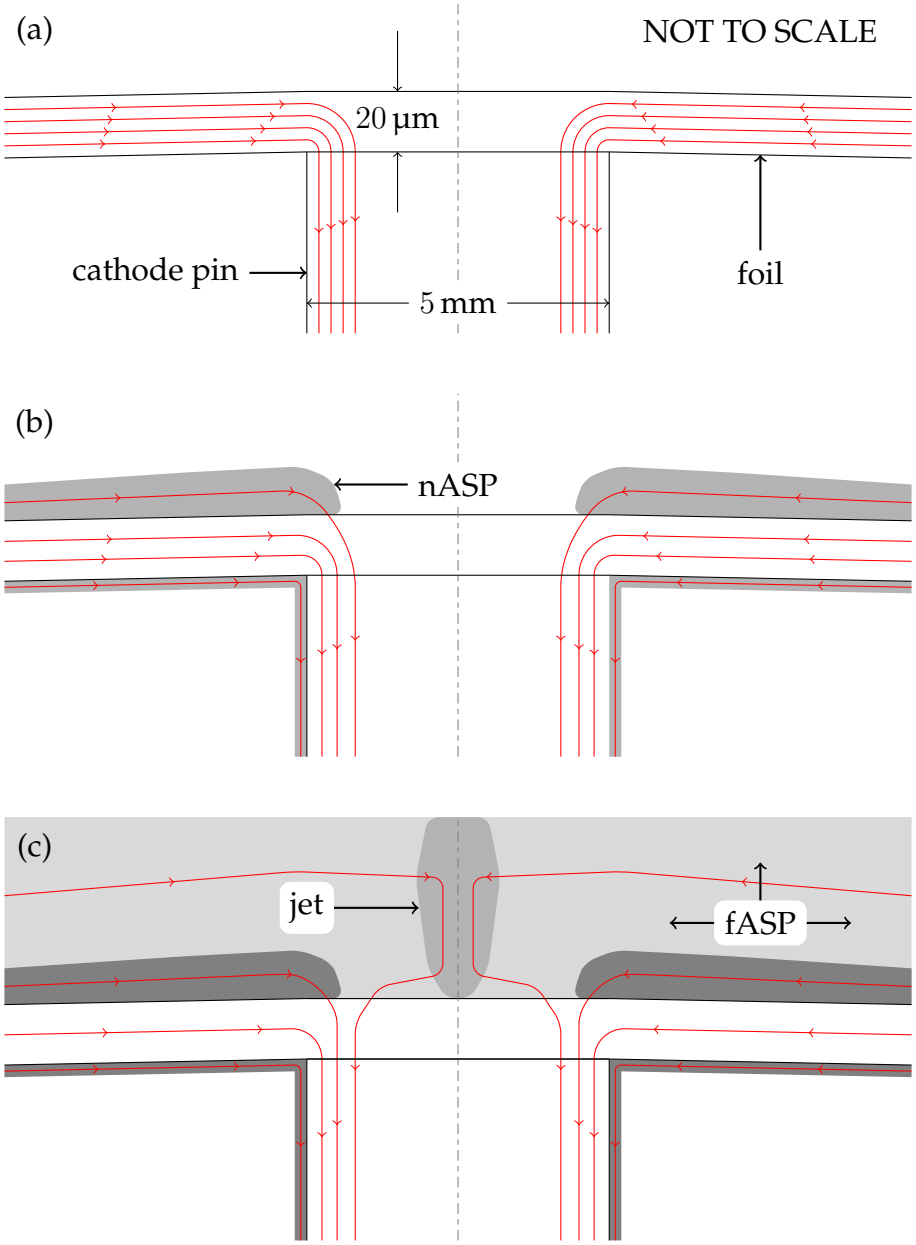

Figure 1.2: Time-lapse cartoon of the ablation of a radial foil. (a) initially electric current flows through the foil itself and an annular cross-section of the cathode pin. (b) Joule heating leads to the ablation of material which becomes a conductive plasma. Magnetic forces ($\mathbf{J} \times \mathbf{B}$) on this nASP push it upwards and inwards towards the axis. (c) The continued ablation of material from the foil leads to higher densities of plasma close to the foil and the (loose) distinction between the nASP and fASP regions. Radially inward magnetic forces on the ASP produce the axial jet. This diagram does not indicate the magnitude of the flow of electric current in each region.

preventing a significant amount of plasma from filling the region below the foil. The *ablated surface plasma* (ASP) above the foil is accelerated upward by this $\mathbf{J}\times\mathbf{B}$ force density.

It is useful to distinguish between three regimes in the forthcoming discussions. We define the nASP or *near* ASP as the relatively high density region extending up to $\sim$1 mm from the surface of the foil. There is a much lower density cloud of plasma surrounding this which we call the fASP or *far* ASP. The third region, the axial *jet* is formed by the motion of these ASPs. Due to the lack of current flow in the foil directly above the cathode pin, owing to the skin effect flow of current in the outer region ($\sim$40 µm to 100 µm) of the cathode, there is little ASP above the center of the cathode. At a slightly larger radius, where the current density in the foil is maximal, there is significant ablation and a build-up of ASP. This differential sets up a considerable pressure gradient, which gives the fluid near the cathode a radially-inward momentum component. The stagnation of intersecting momentum flows from the cathode circumference inward leads to the formation of the hydrodynamic jet on axis. The jet carries some current downward, antiparallel to the direction of fluid momentum. XMHD simulations, using the code PERSEUS described later in Chapter 6, show that a diffuse radially inward and axially upward current flows through the ASP into the jet, where the current builds up and flows downward into the central cathode. This collection of current on-axis leads to a pinching force which enhances the density gradient between the jet and the surrounding region. Later in time, beyond the scope of this investigation, the foil around the central pin is pushed upwards (forming the magnetic bubble) and a z-pinch forms along the axis above the cathode pin.

1.4 Goals

The initial and primary interest of this work was to study the effect of a relatively strong magnetic field (of order one tesla) on the development of the hydrodynamic plasma jet which forms on the axis of an exploding radial foil. This magnitude of field was chosen because it is similar to the maximum expected field due to electric currents in the jet as measured in previous experiments with small B-dot probes. Our goals were dynamic, and adapted based on new information learned from the experiment and computer simulations. The development of these experimental goals is more closely explored in Section 5.1.2.

1.5 Organization

The rest of this dissertation is organized as follows: Chapter 2 gives an overview of the design and construction of coils built to provide a strong and slow magnetic field for the experiment. Chapter 3 covers interferometric methods used as a quantitative diagnostic of our plasmas. The experiment is described in chapter 4 with enough detail that it could be reproduced by the interested reader. Chapter 5 provides an outline of all the data collected, and details a few particularly interesting results. Comparable results from computer simulations are presented in Chapter 6. Chapter 7 gives analytical methods and the result of their application to our experimental and simulated results. These results and analysis chapters focus on four issues:

1. Current-carrying tendrils which are formed by the nASP
2. The central hydrodynamic jet and its dynamics
3. Observed rotation in the fASP around the jet

4. Magnetic field compression on the axis of a magnetized jet

Finally, a summary of the work and ideas for future experiments come in Chapter 8.

CHAPTER 2

MAGNETIC COIL DESIGN

The proper and efficient design of low impedance ($\sim 1\,\Omega$) high current ($\sim 10\,$kA) non-destructively pulsed coils is a complicated subject. This chapter covers some of the largest factors that play into the design process, outlines the choices made for this experiment, and discusses their implementation.

2.1 Design Considerations

2.1.1 Basics

The magnetic field due to a current in a conductor is given by the Biot-Savart law [17], the fundamental equation of magnetostatics, which can be written as an integral over all space as:

$$\mathbf{B}(\mathbf{r}) = \frac{\mu_0}{4\pi} \int \mathrm{d}^3\mathbf{r}' \frac{\mathbf{J}(\mathbf{r}') \times (\mathbf{r} - \mathbf{r}')}{|\mathbf{r} - \mathbf{r}'|^3} \tag{2.1}$$

The field this creates around a long (ideally infinite), thin wire is in concentric circles, oriented according to the right hand rule[1], and dropping off in strength with distance from the wire as r^{-1}. All other magnetic field configurations can be made by manipulating this configuration and making appropriate superpositions. The most basic change is adding a second wire, at which point the relative orientations of the currents become important. With parallel (and equal) currents, the magnetic fields between the wire have opposite polarity and cancel to form a null at the midpoint. The reduced field between the wires leads to decreased magnetic pressure there and an attractive force between the wires.

[1] in a 'thumbs-up' salute, for current coming out of the thumb, magnetic field lines come out of the fingers

With antiparallel currents, the magnetic fields between them add, which leads to increased magnetic pressure and a repulsive force.

Taking one current-carrying wire and curving it around itself into a circular loop creates one of the most commonly encountered magnetic field configurations[2]. If we try to take our concentric circles (field lines) from the straight wire and put them on this loop, they will deform– bunching up in the middle where space is finite and expanding to fill the space outside the loop. Another way to picture it is (see figure 2.1) as the field of two wires with antiparallel currents rotated about the midpoint (the new axis of symmetry). This concentration of the field inside the loop leads to a radially outward force along the conductor. Additional loops with parallel currents will be pinched together while the radial force (sometimes called a hoop force) tries to blow each loop apart. These basic forces are an important consideration in solenoid design.

Because of the radially outward stress on magnetic coils, the best shapes for them involve few if any sharp turns or angles. However, one or two may be unavoidable at the feeds for external connection to a power supply. This experimental work is concerned with applying a magnetic field with a high degree of spatial uniformity. The best uniformity can be achieved with a tightly-wound helical wire configuration known as an air-core solenoid. Ignoring the effects of fringing fields at the boundaries, a large volume of practically constant field can be produced with this method. But a solenoid cannot be coupled with this COBRA experiment to produce the desired physical extent of field while maintaining good diagnostic access to the plasma. Instead we decided to use a pair of loops in what is known as a Helmholtz coil configuration.

[2]In the farfield it's equivalent to a dipole field

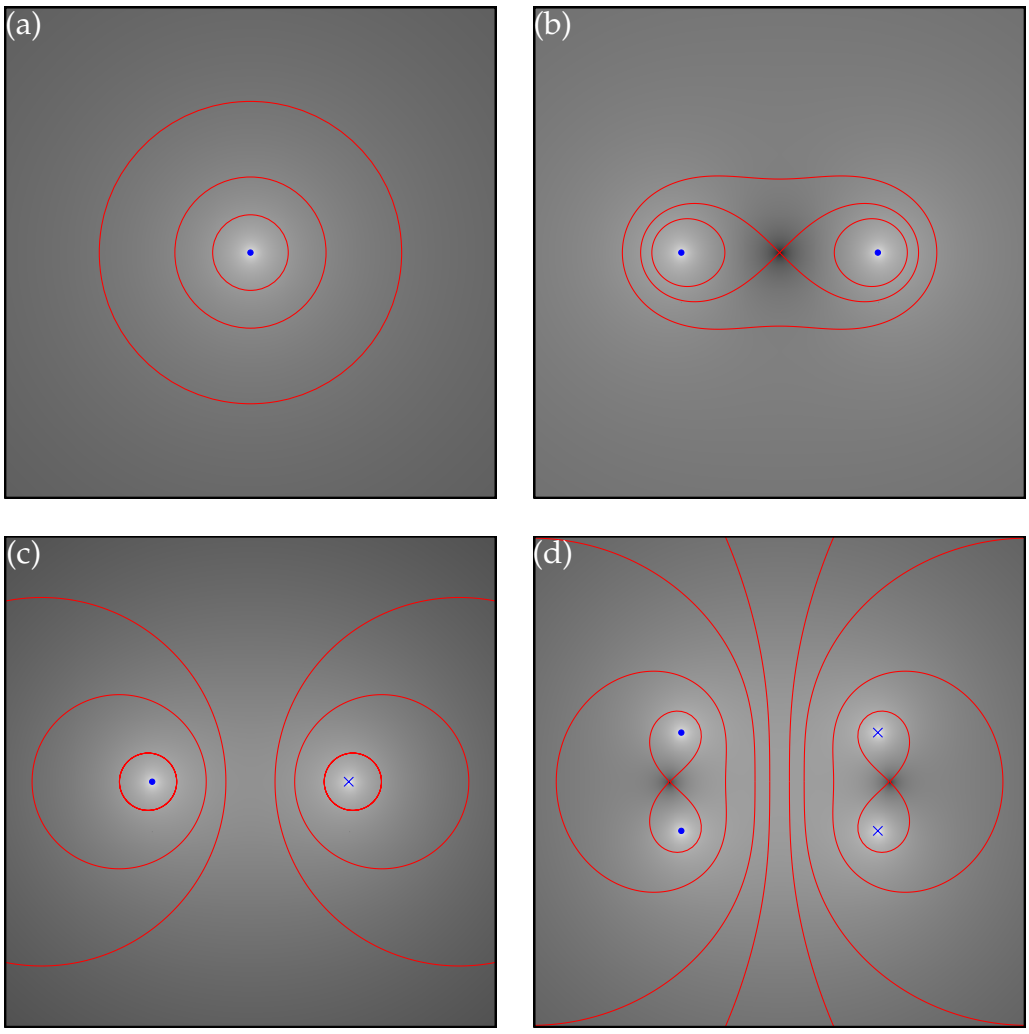

Figure 2.1: Assortment of magnetic field configurations. (a) The field around a single current-carrying wire just forms concentric circles. (b) The field of two parallel current-carrying wires has a zero between the wires. (c) The field of two antiparallel current-carrying wires appears the same as the cross-section of the field from a single current-carrying loop. (d) Two sets of antiparallel wires, or two loops in the Helmholtz coil configuration, can give a remarkably uniform magnetic field in the central region.

2.1.2 Helmholtz Coil

A *Helmholtz coil* has a pair of parallel circular loops of wire, sized such that the radius of the loops is equal to the distance between the loops. If current flows in the same direction in each of the loops, the magnetic field adds in the central region. This leads to a rather large volume of nearly constant field intensity without being fully surrounded like in a long cylindrical solenoid. The magnetic flux density (B field strength) at the center of the Helmholtz coil of radius a with N turns carrying current I is given by:

$$\mathbf{B} = \left(\frac{4}{5}\right)^{\frac{3}{2}} \frac{\mu_0 N I}{a} \tag{2.2}$$

2.1.3 Design Web

The design of a magnetic coil system is a balancing act between several factors, some more flexible than others. There are three main variables that characterize a field: the physical extent or volume ($\sim a^3$) it fills, its strength (magnetic flux density B,) and the timescale τ over which it is pulsed. This section gives an overview of the complicated relationships involved in coil design, following one method of approaching the problem. Figure 2.2 gives a visual representation of the design interdependencies. In practice, the design process is often an iterative one, with subsequent designs tweaked to properly balance all of the issues in play.

Once the style of coil (e.g. Helmholtz coil) has been chosen, the first variable to consider is the radius a of the coils. This is limited by the other experimental hardware the coil is intended to be coupled with. A larger coil can provide greater experimental flexibility at the expense of less magnetic field B or with the requirement of a larger power supply. The power supply is the next major

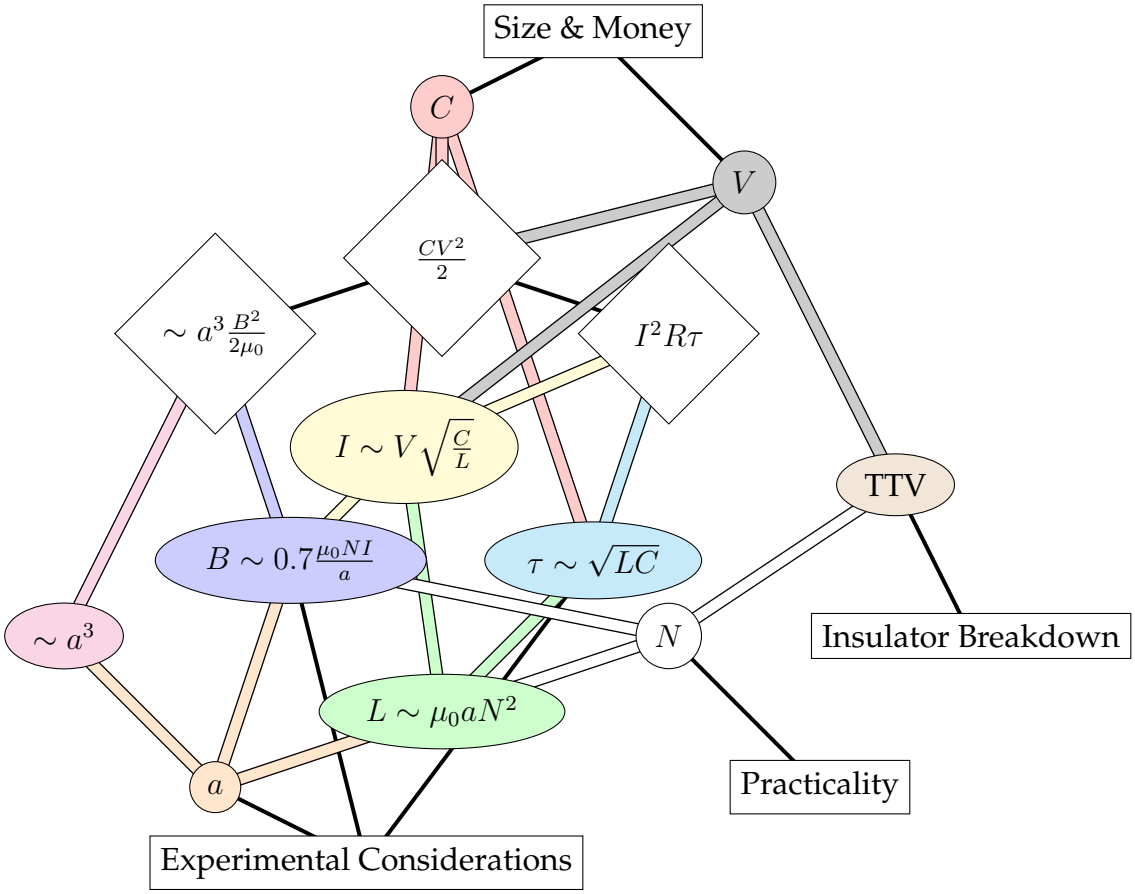

Figure 2.2: Illustration of the complicated relationships involved in coil design. Symbols are defined in the text. The four circles contain the controllable design variables. The ellipses have other dependent variables. The three diamonds represent important energy amounts: maximum energy in the magnetic field, stored energy in the power supply, and resistive losses. The rectangles contain limitations imposed by external factors. Direct dependencies are indicated by the colored bars between nodes.

consideration. It is characterized by a capacitance C and a maximum charging voltage V. It must also have some triggering mechanism to control timing of the pulsed field relative to the experiment. Practical concerns (laboratory space and financial cost) are the main limits to both C and V. Very large voltages require extreme care and possibly stronger insulation with transformer oil. Avoiding that expensive complication and sticking to reasonable ($<10\,\mathrm{kV}$) voltages leaves the relatively small energy density capacity of capacitors as a roadblock. Commerically available capacitors can store a peak energy density[3] of a few atmospheres ($\sim 1 \times 10^5\,\mathrm{J\,m^{-3}}$). According to General Atomics' website [2], they offer capacitors with a peak energy density of 20atm, but these generally offer relatively short lifespans (~ 100 charge/discharge cycles) and are limited to military applications. For us, this means that storing a few kilojoules of energy requires tens of liters of volume. Selecting a power supply sets a maximum stored energy $\frac{CV^2}{2}$ available for the magnetic field and resistive losses. The last major design choice to be made is the number of turns N in the coil. This determines the inductance L of the coil ($L \sim \mu_0 a N^2$) and the turn-to-turn voltage (TTV) in the coil, which must be limited to avoid insulation breakdown. The coil inductance is the last major puzzle piece. It allows us to set the timescale of the field ($\tau \sim \sqrt{LC}$) and the current pulsed in the line ($I = V\sqrt{\frac{C}{L}}$). The timescale of the field ought to be slow enough that it can be considered constant on the experimental timescales of interest and to sufficiently penetrate the experimental hardware (to avoid significant eddy currents producing an opposing field.) This allows us to take full advantage of the spatial uniformity of the field provided by a Helmholtz coil. The current I is limited by hardware (how much the pulser can deliver and how much the cable can carry), and the previously determined variables dictate the maximum magnetic field B given by equation

[3] Energy stored in the electric field $\frac{\epsilon_0 |\mathbf{E}|^2}{2}$

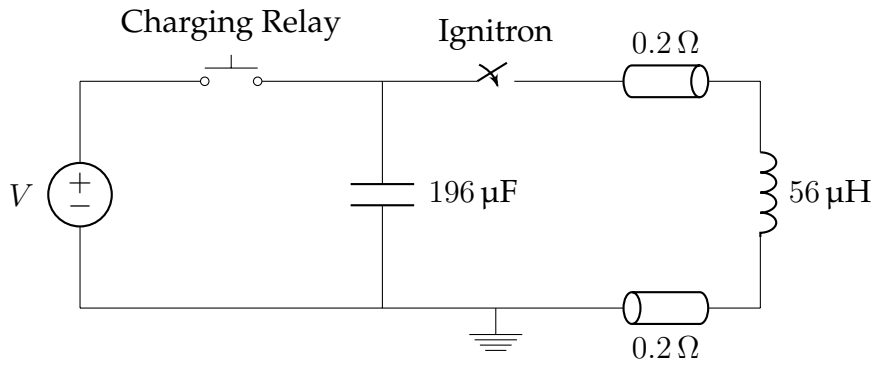

Figure 2.3: A simplified circuit diagram of our chosen bank and coil system.

2.2. This tells us the total peak energy in the magnet ($\sim a^3 \frac{B^2}{2\mu_0}$), and the amount we can expect to lose from resistance in the system ($I^2 R\tau$). The maximum magnetic field must be accounted for in designing the structure that holds the coil in place, as forces on the two loops will attempt to squeeze them together while exploding each loop radially outward. A strong fiberglass casing and an epoxy 'potting' of the coil can prevent this.

The network in Figure 2.2 shows interdependencies that might not be apparent when just looking at the formulas alone. For example, increasing the number of turns in the coil N appears to increase B, but making substitutions of I and L in the formula for B shows that it is independent of N. In fact, increasing N would likely decrease the maximum magnetic field because of the longer timescale and increased resistive losses. This is major issue for designing long-pulse magnetic field coils.

2.1.4 Circuit Modeling

These resistive losses can be more quantitatively dealt with by modeling the transmission cable, field coils, and storage bank as an RLC circuit. Figure 2.3

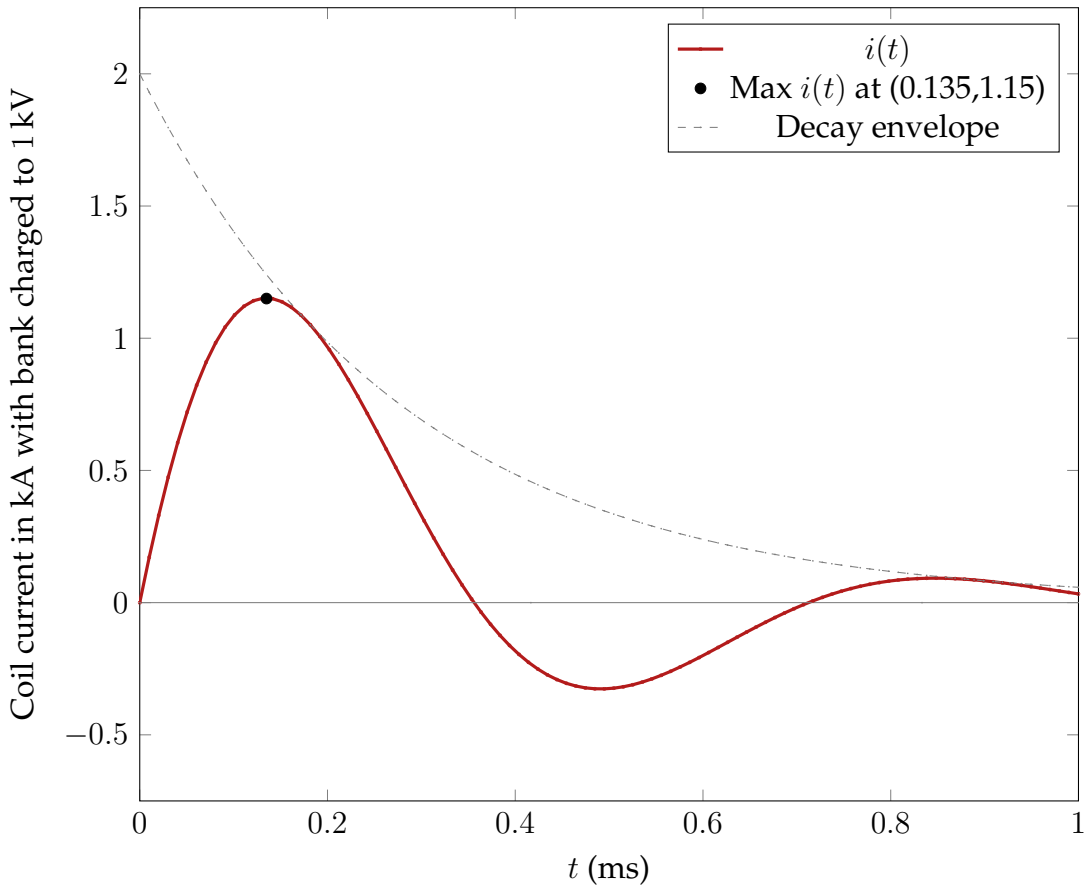

Figure 2.4: Plot of predicted current profile.

gives a simple circuit model that allows us to predict the coil response. Because our timescale is so long relative to the distances involved, we don't have to worry about a rigorous transmission line treatment of the signal. The long coaxial lines act as resistors which add a signficant amount of damping to the system.

We can model this with a second-order differential equation as follows:

$$\frac{\mathrm{d}^2 i(t)}{\mathrm{d}t^2} + 2\alpha \frac{\mathrm{d}i(t)}{\mathrm{d}t} + \omega_0^2 i(t) = 0 \tag{2.3}$$

With $\alpha = \frac{R}{2L}$, $\omega_0 = \frac{1}{\sqrt{LC}}$, $\zeta = \frac{\alpha}{\omega_0}$ and $\omega_d = \sqrt{1-\zeta^2}$. Equation 2.3 has the solution:

$$i(t) = \frac{V_c}{\omega_d L} \mathrm{e}^{-\alpha t} \sin(\omega_d t) \tag{2.4}$$

Figure 2.4 plots of $i(t)$ for our values, which give an "underdamped" waveform: C =196 µF, L =56 µH, and R =0.4 Ω. These values were measured directly and match up well to the design specifications (see Table 2.1).

2.2 SERPENTOR

2.2.1 Overview

After careful consideration of all the factors discussed in the previous section, a pair of coils was made with the design summarized in Table 2.1. From previous experiments and simulations, the expected azimuthal B_θ due to currents in the jet is no more than a few teslas, so applying a B_z of similar strength would be a significant perturbation and reasonably obtainable for the present investigation. The coils were coupled with a power supply in a system called SERPENTOR (Source of Electromagnetic Reactance for the Provision of ENergy to a TORoidal coil configuration).

2.2.2 Storage Bank

The power supply was repurposed from system used to power coils on the FIREX machine. This ensured it had all the necessary parts: high voltage supplies, capacitors, switching relays, and a triggering system. The bank stores energy in two 100 µF Maxwell capacitors in parallel, which are rated to 10 kV. A set of three high voltage power supplies can charge the capacitors to 6 kV (the maximum voltage used in these experiments) in about a minute, which is

Table 2.1: Chosen design parameters for the SERPENTOR system with Helmholz coil

Parameter	Symbol	Formula	Value
Coil Size	a		$0.1\,\mathrm{m}$
Capacitance	C		$200\,\mu\mathrm{F}$
Voltage	V		$6\,\mathrm{kV}$
Number of Turns	N		12
Inductance	L	$\mu_0 a N^2$	$50\,\mu\mathrm{H}$
Pulse Timescale	τ	$\sqrt{LC}$	$100\,\mu\mathrm{s}$
Current	I	$V\sqrt{\frac{C}{L}}$	$12\,\mathrm{kA}$
Field Strength	B	$\left(\frac{4}{5}\right)^{\frac{3}{2}} \frac{\mu_0 N I}{a}$	$1.5\,\mathrm{T}$
Stored Energy	$\mathcal{E}_\mathrm{C}$	$\frac{CV^2}{2}$	$3.6\,\mathrm{kJ}$
Field Energy	$\mathcal{E}_\mathrm{B}$	$a^3 \frac{B^2}{2\mu_0}$	$2.4\,\mathrm{kJ}$
Resistive Losses	$\mathcal{E}_\mathrm{R}$	$I^2 R \tau$	$1.2\,\mathrm{kJ}$

roughly the charging time for COBRA's main Marx generator. A set of relays control the charging, dumping, and firing preparation of the capacitors. The current is triggered and switched through an ignitron, in which a mercury bath is used as a conductor across a large gap. With the relays in the firing mode, the anode of the ignitron (central stalk at top) is at high voltage. A vacuum gap separates this from the mercury bath (cathode). When a trigger pulse into a pin 'ignites' the mercury bath, a mercury plasma fills the vacuum gap and the ignitron acts as a closed switch until the current drops below a threshold level. The power feed cable for the Helmholtz coil is attached to the ignitron cathode along the outer casing.

If the storage bank has difficulty holding a charge (unintended discharges at a few hundred volts), then there may be mercury droplets on the anode which

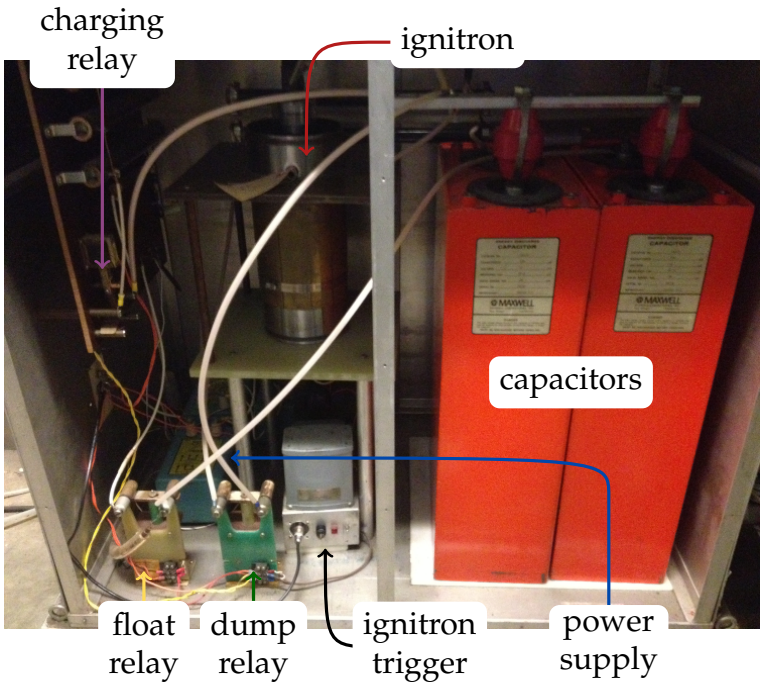

Figure 2.5: The SERPENTOR energy storage bank with major components labelled.

could cause it to short out. Slowly heating the anode with a lamp can boil off this mercury. Once the mercury has been given the chance to condense and return to the bath, the switch should be restored to normal operation.

Controls

The storage bank is linked to a control panel with a 6-pin cable that provides power (only the control panel itself has an electric utility connection) and controls the three relays. Two BNC cables give charging voltage and current readouts on the control panel.

The firing sequence of SERPENTOR is as follows:

0. Make sure current paths (i.e. power supply bank to coils) are complete and properly insulated.

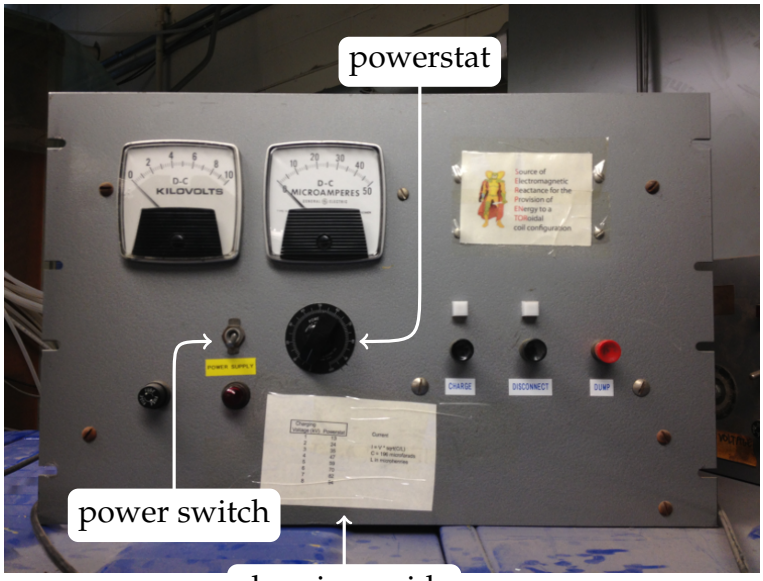

Figure 2.6: The SERPENTOR control panel.

1. Turn down powerstat.
2. Flip on toggle power switch (red light comes on).
3. Press 'charge' to activate charging relays.
4. Turn up powerstat to reach desired firing voltage, accounting for the drop in voltage when disconnecting. (There's a guide on the panel for this.)
5. Press 'disconnect' to isolate the capacitors and ignitron from the voltage supplies. (If firing during a COBRA shot, do this at the same time the COBRA operator presses 'disconnect' on COBRA .)
6. Press COBRA trigger.
7. Press 'dump' and flip off the toggle power switch after firing or if there is any irregularity (i.e. drop in voltage during charging) before examining the storage bank box.

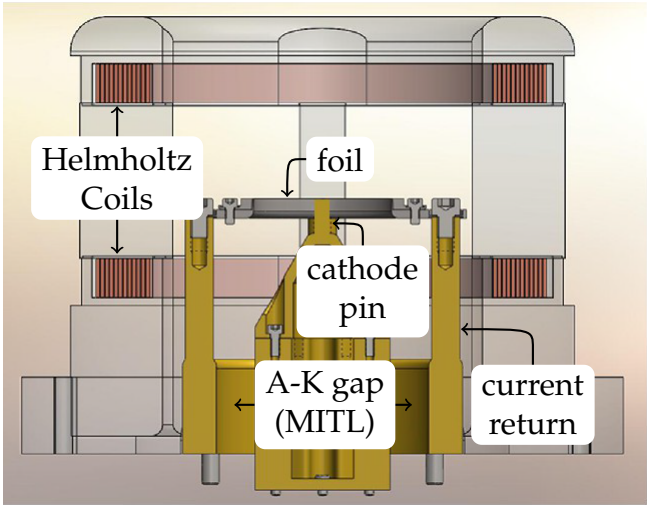

Figure 2.7: A cutaway diagram details the coils for providing an axial magnetic field and the hardware that connects the radial foil load to the COBRA A-K gap with important parts labelled.

2.2.3 Coils

The design of this experiment's coils has been discussed at length. This section will outline a few lingering design considerations and provide a gross description of the construction process.

The rise-time of the coils (100 µs) was set to be significantly slower than the rise-time of the COBRA pulse (100 ns) as well as sufficiently slow to penetrate the foil hardware (minimize azimuthal eddy currents.) But the field should not be able to penetrate the vacuum magnetically-insulated transmission line (MITL) gap and short out that insulation. This is a small concern for this particular set of coils because the radial fringing fields from the Helmholtz coils in the MITL gap are much smaller (by a factor ∼0.01) than the azimuthal MITL fields. The coil pulse is actually not slow enough to fully penetrate the foil hardware, so the field strengths quoted in this work (from B-dot measurements made ∼1 mm above the foil) are ∼66% of the 'vacuum' field which is measured in the absense

of the foil hardware. Despite this, the variation in $|B_z|$ in the region of interest above the foil is small (<10%).

Once all of the design parameters have been reiterated and finalized, construction can begin. In this case, a flat strip conductor of Cu-Be alloy was hand-wrapped into a spiral around a circular form. A double layer of kapton film was wrapped around the wire to provide insulation against the high voltages between turns. The coils were carefully twisted (with a torque along the spiral axis to minimize gaps between the turns) to full and uniform compression and placed in a shell made of G10 fiberglass. External feed cables were silver-soldered to the coils. This was then potted with STYCAST 1264 A/B epoxy which was deaired for several hours in a vacuum chamber before curing. The end result with the coils and how they fit around the foil hardware is depicted in Fig. 2.7.

The coils can be pulsed in opposite polarities easily by exchanging the feed cables. This allows for switching the orientation (upward or downward) of the applied B_z from one shot to another. The coils have been wound such that when the center conductor of the transmission line from the storage bank is connected to the lower coil input, the applied B_z has an upward orientation. There is a hard-wired connection between the bottom and top coils so each is always providing a field in the same direction as the other. Because of this, this set of coils cannot be operated in a 'cusp' configuration which would put a magnetic zero near the axis between the coils.

CHAPTER 3

INTERFEROMETRY

3.1 Motivation

Interferometry is a set of techniques that uses the superposition of waves to learn about the waves themselves. It allows for the study of physical phenomena that affect waves. Owing to their tiny mass, the electrons in a plasma react quickly to the local changes in electric field due to an electromagnetic (EM) wave passing through the plasma. The predictable effect this has on the passing EM wave can be used to infer plasma properties. Radio interferometry has been used since the 1940's for studying astronomical radio sources like the sun [21]. The invention of the cavity magnetron allowed the laboratory use of microwaves with this technique [25]. The development of the laser has opened up a new parameter space of plasma densities and enables simultaneous imaging. Laser-based optical interferometry remains an important and useful diagnostic tool for studying plasmas. This chapter explores a few methods of imaging interferometry, focussing on those relevant to the present investigation, and describes a general approach for the interpretation of data produced by imaging interferometry. This chapter draws on and greatly expands work from my undergraduate thesis [29].

3.2 Theory of Interferometry

Thanks to the work of Maxwell [20], Hughes, and Hertz, we can represent a monochromatic beam of light as an EM wave mathematically in terms of its electric field $\mathbf{E}$:

$$\mathbf{E}(\mathbf{r},t) = \mathbf{E_0}(\mathbf{r},t)\mathrm{e}^{\mathrm{i}(\mathbf{k}\cdot\mathbf{r}-\omega t+\phi)} \tag{3.1}$$

This is one generalized[1] solution to the wave equation formed by combining Faraday's law and the Maxwell-Ampere law. Here the added phase ϕ is a complicated object with a dependence on both the current position of the wave and its history. The goal of interferometry is generally to determine ϕ and some useful data that it represents. We will refer to the $\mathbf{k}\cdot\mathbf{r}$ term as the *carrier* phase and ϕ as the *object* phase.

We cannot directly measure ϕ, or even $\mathbf{E}$, for a given light wave. However, what we can perceive with our eyes or record with photographic film or a charge-coupled device (CCD) is a light wave's intensity I, which is proportional to $|\mathbf{E}|^2$. When just a single beam is present, the complex exponential in Equation 3.1 drops out of the formula for intensity, so the phase ϕ cannot be recovered. But if we have multiple *coherent* (like laser light of a given frequency and polarization) beams coincident on a single detector, an intensity pattern forms that can make it possible to deduce the form of ϕ. Take for instance the addition of two beams of the form of Equation 3.1.

$$\mathbf{E}_{\text{int}}(\mathbf{r},t) = \mathbf{E_1}(\mathbf{r},t)\mathrm{e}^{\mathrm{i}(\mathbf{k}_1\cdot\mathbf{r}-\omega_1 t+\phi_1)} + \mathbf{E_2}(\mathbf{r},t)\mathrm{e}^{\mathrm{i}(\mathbf{k}_2\cdot\mathbf{r}-\omega_2 t+\phi_2)} \tag{3.2}$$

This has complicated things greatly! Now there are two sets of phases to keep track of. An important simplification comes from taking the beams to be from the same monochromatic laser source and with the same polarization

[1]The variation of the amplitude function $\mathbf{E_0}(\mathbf{r},t)$ in space and time is assumed to be much slower than the variations associated with the wave itself. This means $\nabla^2 E_i << |\mathbf{k}|^2 E_i$ and $\mathbf{k}\cdot\nabla E_i << |\mathbf{k}|^2 E_i$ and $\frac{\partial E_i}{\partial t} << \omega E_i$ for each cartesian component i. This is a reasonable assumption for green laser light with λ=532 nm because the angular frequency ω ($3.5\times10^{15}\,\mathrm{s}^{-1}$) is much greater than the frequency of variation of a 120 ps pulse ($8.3\times10^{9}\,\mathrm{s}^{-1}$) and the wavenumber k ($1.2\times10^{7}\,\mathrm{m}^{-1}$) is much greater than the inverse of the scale length of spatial variations of interest ($10^{4}\,\mathrm{m}^{-1}$). Hiccups arise with sharper variations which leads to diffraction, discussed later.

($\omega_1 = \omega_2 = \omega$ and $\mathbf{E_1} \parallel \mathbf{E_2}$) with spatial and temporal uniformity (constant $E_1 = E_2 = E_0$). We place a detector at $z = 0$ on the x-y plane. Plugging these assumptions into Eq. 3.2 and finding the intensity gives:

$$I_{\text{int}}(x, y) \propto 2E_0^2 \left[1 + \cos\left(\mathbf{k}_1 \cdot \mathbf{r} - \mathbf{k}_2 \cdot \mathbf{r} + \phi_1(x, y) - \phi_2(x, y)\right)\right] \tag{3.3}$$

Now the intensity I_{int} is a pattern of sinusoidal fringes, the spacing between which is determined by the differences of the carrier and object phases of the two beams. If we consider perfectly collimated beams and take the first beam to be travelling along the z-axis ($\mathbf{k}_1 \parallel \hat{z}$) and the second beam to have a small component in the y direction, the intensity will take the form of Eq. 3.4.

$$I_{\text{int}}(x, y) \propto 2E_0^2 \left[1 + \cos\left(k_y y - \phi_1(x, y) + \phi_2(x, y)\right)\right] \tag{3.4}$$

If the beams are not collimated, the phase fronts will not be planar and the carrier phase term ($k_y y$) will have a much more complicated form. In many experiments, a lens is used to magnify and focus the image of the target onto a detector. For a given incoming beam, this lens will produce a focal point between the lens and the detector. If a second beam is not perfectly coincident with the first, it will produce a second distinct focal point. A focussed beam will expand with spherical fronts of constant phase between its focal point and the detector. The manner in which the two expanding beams overlap and interfere is responsible for a huge variety in carrier phase fringe patterns. Two important arrangements of final optics are shown in Figure 3.1. If we take d to be the distance between the focal points, R to be the distance from the focal points to the detector, and θ to be an angle describing the orientation of the detector, we can use Figure 3.2 to see how the different path lengths will affect interference patterns on the detector. Letting (x, y) be a point on the detector, we plot $I_{\text{int}}(x, y)$

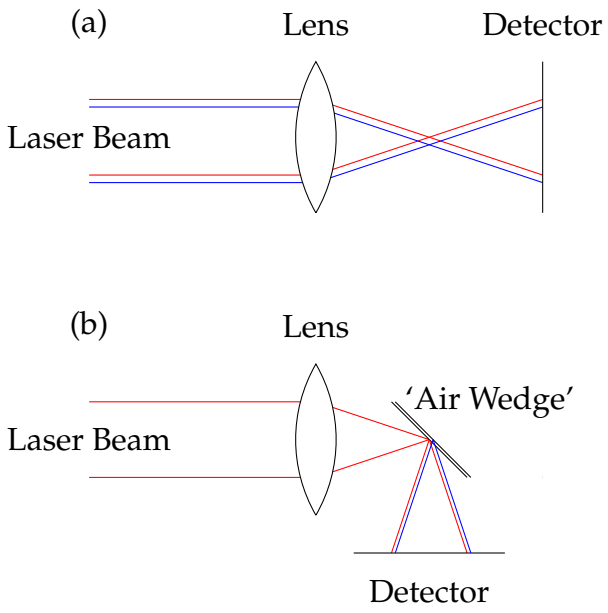

Figure 3.1: Depiction of how the focussing optics create distinct focal points in different interferometers. (a) For Michelson and Mach-Zender interferometers, the beam splitting occurs before the final optics and the focal points are generally beside one another relative to the detector. In these cases, $\theta \approx 0$, so the carrier fringe pattern consists of parallel lines. (b) In a shearing interferometer, the gap and angle of the air wedge can move the effective focal points to many positions relative to the detector, allowing for a wide range of θ.

for a variety of θ and d to show some possible fringe patterns in Figure 3.3. The relative orientation of the focal points and detector can be modified to adjust the angle of the fringes or to produce elliptical fringes instead of circular ones.

The sample fringe patterns illustrate that for a pair of focal points in a hypothetical phase-detecting sphere, fringes on the surface of the sphere would appear like lines of latitude on a globe. The line connecting the two focal points extends to the poles of that globe, producing the concentric circles in Fig. 3.3 when $\theta = 90°$. When we look in the direction $\theta = 0$, we are looking towards the equator of the globe, so lines of latitude are parallel lines. With λ being the wavelength of the laser light, the minimum fringe spacing f_{min} (at the 'equator')

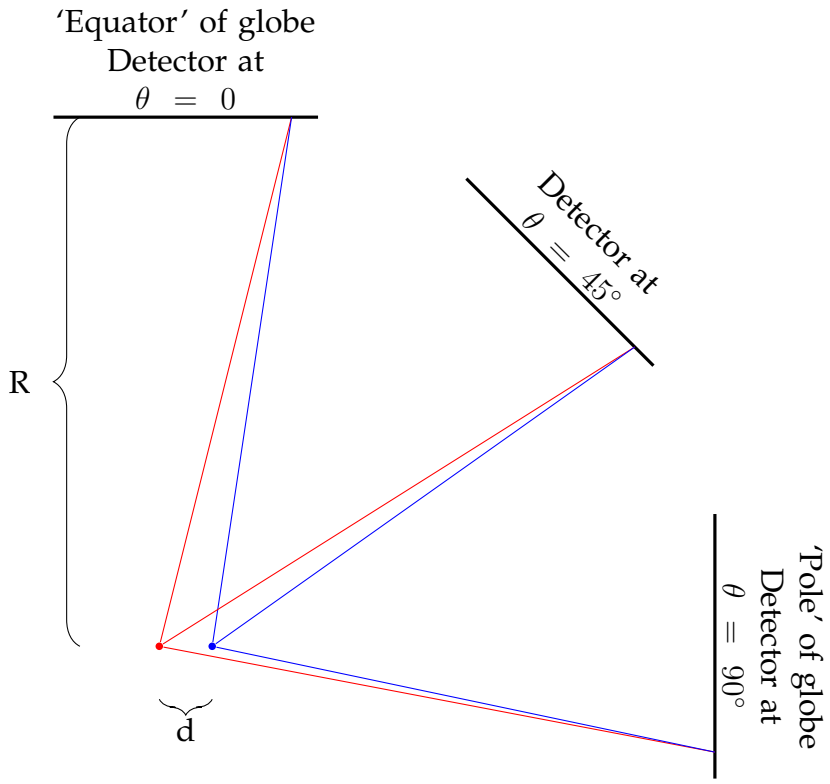

Figure 3.2: Schematic of focal points showing how spherical phase fronts emanating from two focal points can lead to a variety of interference patterns depending on detector position. The path length to a point (x,y) on the detector from the blue (+) or red (-) focal point is given by: $\sqrt{\left(R\sin\theta - x\cos\theta \pm \frac{d}{2}\right)^2 + \left(R\cos\theta + x\sin\theta\right)^2 + y^2}$. Carrier interference results from the difference between these path lengths. The fringe patterns can be compared to lines of latitude on an imaginary globe.

can be determined to be the following:

$$f_{\text{min}} = \frac{R\lambda}{d} \tag{3.5}$$

In the case of light travelling through a plasma, ϕ contains information about the electron density of the plasma. This relationship is due to the EM wave's interaction with free electrons in the plasma. EM waves in a plasma follow the

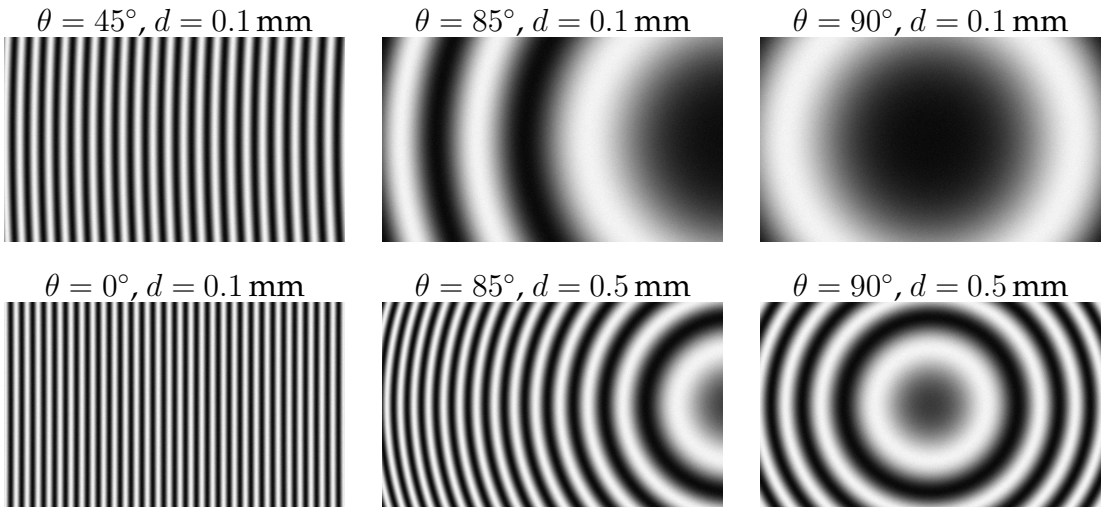

Figure 3.3: A selection of computer-generated fringe patterns showing the concentric circles near the 'pole,' and the parallel fringe pattern that arises when the detector moves relative to the focal points. These examples used $R = 150\,\text{mm}$ and are representative of carrier fringe patterns formed in the absence of any perturbative plasma.

dispersion relation $\omega^2 = \omega_p^2 + k^2c^2$ [4] or in terms of wavenumber, $k = \frac{\omega}{c}\sqrt{1 - \frac{\omega_p^2}{\omega^2}}$. Here ω_p^2 is the squared plasma frequency, proportional to the electron number density n_e. The change in k modifies the *effective path length* experienced by a particular ray relative to its neighbors that travel through plasma of a different density. We have retained all of this information in the object phase ϕ in equation 3.1.

Bellan [3] gives a clear and concise derivation of how this ϕ relates to the line-integrated electron density along the path that the light ray took through the plasma. Note that this is valid for the case $\omega_p^2 << \omega^2$, so the electron density is well below cutoff.

$$\phi = -\frac{e^2}{2\omega c m_e \epsilon_0}\int_0^L n\mathrm{d}x = -\frac{\mu_0 e^2 \lambda}{4\pi m_e}\int_0^L n\mathrm{d}x \tag{3.6}$$

Thus, with our green laser (λ =532 nm) and for a single fringe shift ($\phi = 2\pi$), we have a line-integrated areal density of $\int_0^L n\mathrm{d}x$ =4.2×10^{21} m^{-2}. This means that, depending on the assumed length (from a few centimeters to fractions of a millimeter), one fringe shift represents electron volume densities in the range 10^{23} m^{-3} to 10^{25} m^{-3}

3.3 Experimental Implementations

There are several ways to set up a situation where coherent beams interfere with one another. Figure 3.4 shows three varieties of laser-based interferometers, each of which is described in the following sections. For this discussion, we will call the beam that does not go through the plasma the *reference* beam and the one that does the *sampling* beam.

3.3.1 Michelson

A basic and easily constructed interferometer is the Michelson interferometer, famous for its use in the Michelson-Morley experiment of 1887. With this design, light is split into two perpendicular beams by a 50-50 beam splitter. These beams are reflected back through the beam splitter by mirrors. Interference patterns can be observed in the recombined beams. To observe the influence of a perturbing medium on the interference pattern, it can simply be put in the path of one of the beams. See Figure 3.4(a). This simplicity of operation is an advantage of the Michelson design. The main drawback to this method is that the perturbed beam travels twice through the perturbing medium, so analysis of the results can be more involved. Another issue with using a Michelson interferometer is that on the second pass, the laser pulse will experience a different

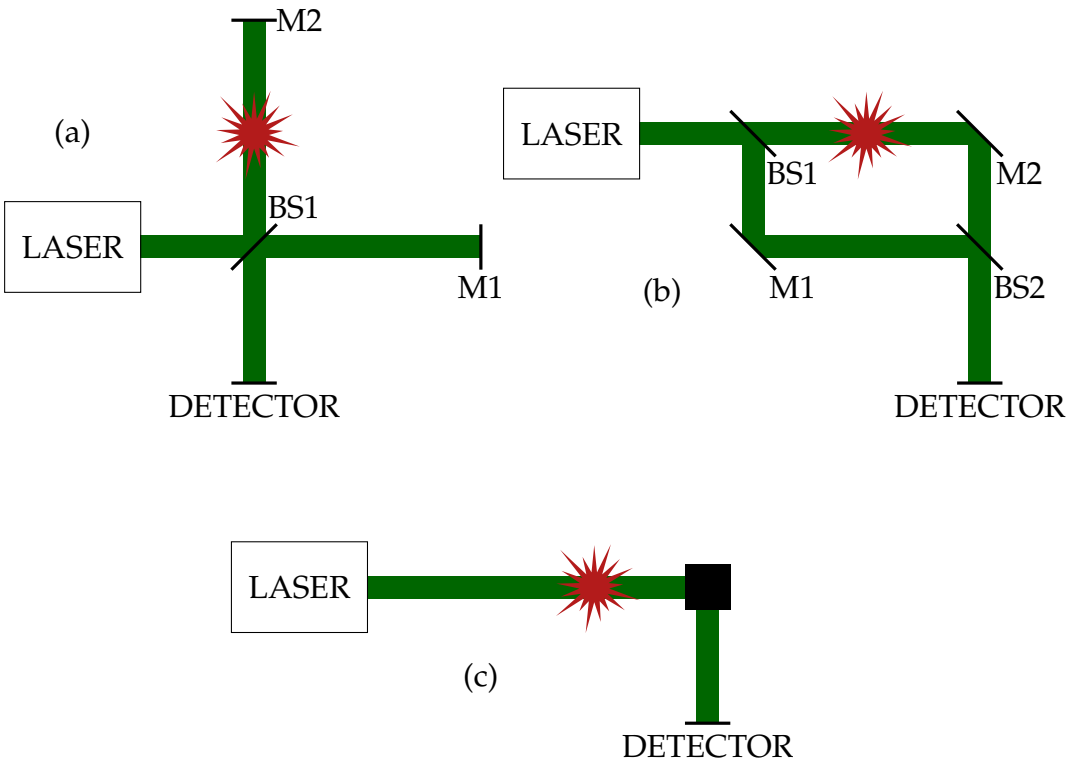

Figure 3.4: Schematics of three important types of interferometers: (a) Michelson (b) Mach-Zender (c) shearing

plasma. This may be negligible if the plasma dynamics are 'slow' compared to the time between passes and if the spatial varation in the plasma is small on the length scale of the lateral shift between the first and second pass. The two optical paths must also be of same length for good interference. This is easier to achieve with the Michelson design because it has fewer optical components than the Mach-Zender design.

3.3.2 Mach-Zender

A Mach-Zender interferometer operates similarly to a Michelson interferometer but uses two separate 50-50 beam splitters: one for splitting and one for recombination. The two separated beams can be manipulated independently,

making this a highly versatile configuration. Figure 3.4(b) illustrates a Mach-Zender interferometer. The main drawback of this design is its requirement for another optical path around the experiment for the reference beam. Each optical component increases the danger of unintentional misalignment. The second distinct path creates another difficulty when using short pulsed lasers, as much care must be taken to ensure that both legs of the interferometer have the same optical path length to within a small fraction of the beam length to produce well-contrasted interference. To look at numbers relevant to this research, the 120 ps diagnostic laser used on COBRA has a beam length of 3.6 cm. Implementing such a short-pulsed Mach-Zender interferometer requires very accurate distance measurements and may also need calibration with fast photodiodes.

3.3.3 Shearing

Shearing interferometry involves taking the beam *after* it has gone through some perturbing medium and then splitting and recombining it to produce interference. This splitting can be accomplished with an air-wedge formed by a gap between adjustable glass prisms [23]. An advantage of this method is its compactness and robustness. A significant drawback that comes along is a more difficult and finicky set-up.

Large Shear

When a portion of the beam has not been significantly affected by plasma, that part of the beam can be used as a the reference beam. This arrangment can ideally provide the ease of interpretation of a Mach-Zender interferometer with the simplicity of operation of a shearing interferometer. Adusting the air-wedge changes the position of the beam focal points (changing the fringe pattern) as

well as modifying the linear displacement of the two beam images. These factors must be carefully balanced, which complicates tuning the interferometer.

Small Shear

When there is not enough 'free' or unperturbed area on the beam to provide interference as described above, the shearing wedges can still be used. But in this case, the observed phase involves the difference of the object phase of the beam and a linearly shifted version of itself. If the shift is confined to one dimension, the phase takes the form $k_y y + \phi(x, y) - \phi(x + \delta, y)$. For a very small δ, it may be possible to consider this term like a numerical derivative of the phase. This could be advantageous in applying the data to an Abel-inversion technique that requires differentiation (covered in Section 3.4.5) For arbitrary δ, it is quite complicated to fully unwrap a small shear fringe pattern into $\phi(x, y)$.

'Torquing'

A novel interferogram design used for axially probing wire array z-pinches was developed at Cornell [24]. This involved splitting and then rotating a circular beam profile onto itself using dove prisms. It was intended for use similar to a 'large shear' linear shearing interferometer. This means that it could only reasonably probe the early-time dynamics of a low-wire-number array, as this ensured there would be some unperturbed beam area to act as a reference.

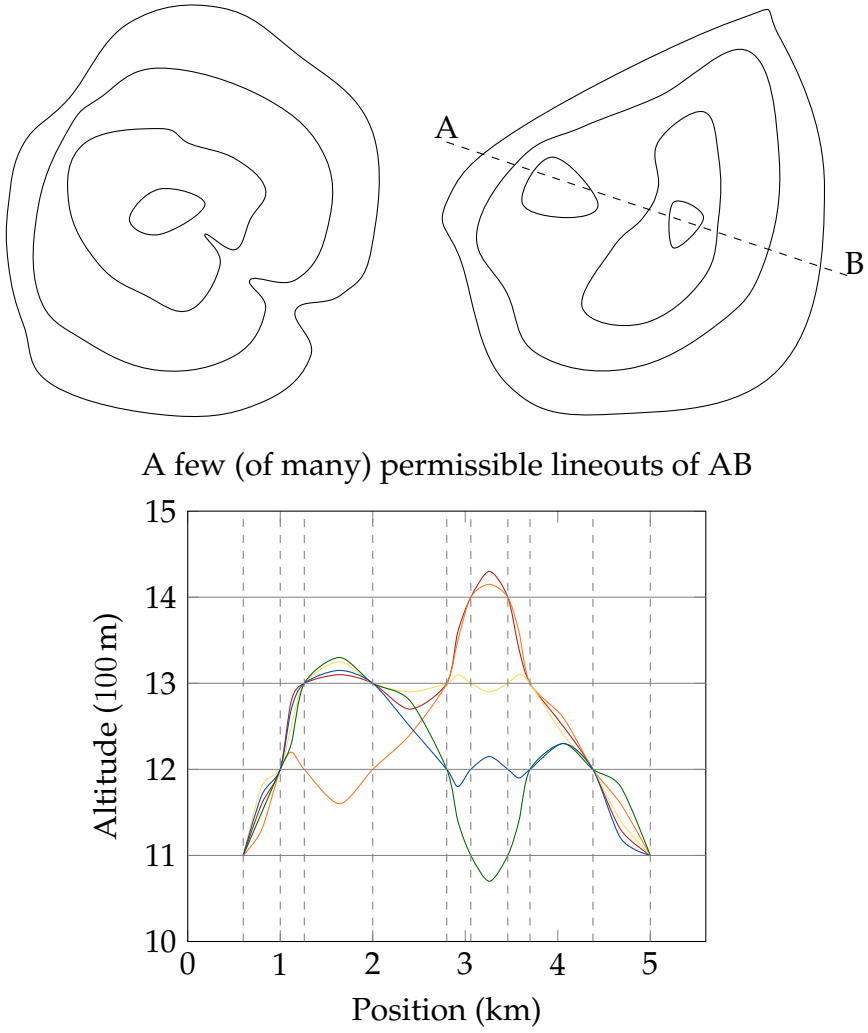

Figure 3.5: Two different topographic maps of varying difficulty to fill-in. The left example, if assumed to be monotonically rising to a central peak, can be trivially completed. The right example has no such trivial solution. A range of possible interpretations of this map is given in the graph. For a given map with f unmarked closed loops, the number of interpretations of that map may be as large as 2^f. Some interpretations are more likely than others, but significant ambiguity remains.

3.4 Interferogram Analysis

3.4.1 Mountain Climbing

A short story may be an instructive introduction to methods of interferogram analysis. Imagine we have a mountain climber who wishes to document every nook and cranny of a new conquest. Over the course of several runs up and down the face, he sets his altimeter to beep whenever his altitude ends in 00 (in meters.) At every beep, he plants a flag to mark that spot. After our climber has placed many flags, an aerial observer would start to notice a developing pattern: the flags are grouped in lines of constant altitude. Our climber is building a physical topographical map, but in his haste and excitement he has neglected to record altitude data for the flags! To salvage the project, he hires a pilot to go up so he can take a picture of the flag-studded mountain from above. Back at base camp, he analyzes the photo using what information he has. He knows there are $100\,\mathrm{m}$ between each level of flags and that the base camp is at $1000\,\mathrm{m}$ elevation. Using this data and his knowledge of the mountain's overall shape (it has a single central peak,) he can quite easily fill in all the elevation lines on his topographic map. But if he were try the same process on a more complicated mountain with several ridges or valleys, he could not unambiguously decide how to label the elevation. Figure 3.5 shows the difference between an 'easy' mountain and a 'difficult' mountain in this sense.

An unlabeled topographical map[2] is a great analogy for an interferogram. Instead of lines of constant altitude, we now have lines of constant phase. Phase is arbitrary to an addend of the form $2\pi n$ for any integer n. This is a double-edged sword, as it means we don't have to worry about determining absolute phase,

[2]For a relatively smooth area, without any vertical cliff faces or overhangs

but we need more data to get meaningful relative phase. In imaging experiments, this extra data is usually in the form of a *preshot* or *unperturbed* image. Here the phase is simply the carrier phase ($\mathbf{k}_1 \cdot \mathbf{r} - \mathbf{k}_2 \cdot \mathbf{r}$). The simplest preshot images for analysis appear as parallel lines (with carrier phase of the form $k_y y$), with at least one fringe line in a region of low expected electron density. In an ideal scenario, this line remains static in the *shot* or *perturbed* image and provides a straightforward way to correlate our fringe count between the two. It allows us to assume that phase in the shot image is of the form $k_y y - \phi(x, y)$ for a known $k_y y$ and that $\phi(x, y) = 0$ along at least one fringe. Even in this ideal situation, the $2\pi n$ ambiguity may crop up if $\phi(x, y)$ varies in a certain way. This issue will be tackled in the next section.

3.4.2 Synthetic Interferograms

This section will explore a variety of computer-generated fringe patterns produced by various carrier and object phase distributions. They will be used to explore issues relevant to interferogram interpretation.

Escaping Ambiguity

To avoid the situation described in Figure 3.5, we will need to determine what limitations are necessary to produce easily interpretable fringe patterns. If we consider a linear carrier phase, $k_y y$, then our unperturbed interferogram will have parallel fringes. Adding an object phase will cause these fringes to shift, bunching together on one side (the 'downhill' side) of the object and spreading apart on the 'uphill' side. At some magnitude of object phase, this bunching and spreading leads to the creation of closed fringes around one side of the object. These kinds of fringe patterns are ambiguous because we can create an

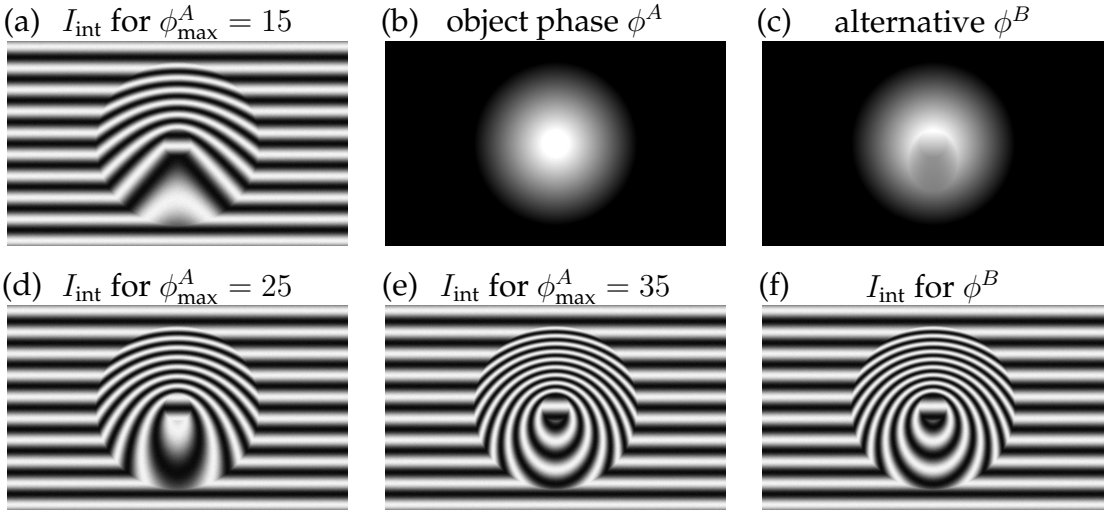

Figure 3.6: Computer-generated fringe patterns showing possible ambiguity. (b) object phase ϕ^A is a flat-topped cone used with various amplitudes to produce (a), (d) and (e). The object phase given in (c) is a variation of ϕ^A with a more complicated shape which can produce (f), an interference pattern identical to (e).

alternative object phase which will produce an identical interference pattern. This issue is illustrated in Figure 3.6.

The ambiguity begins when the object phase build-up on one side of the object exceeds the carrier phase across the whole object. This means that the number of carrier fringes that pass through the region containing the object is not sufficient to capture the object phase at every point in the object. Considering Figure 3.7, we say that an ambiguous fringe pattern occurs when the total phase (carrier plus object) along a lineout is not monotonic.[3] This requirement can be written in terms of the carrier phase wavenumber and object phase derivative as:

[3]for convenience's sake we count fringes upwards, although the result is the same either way.

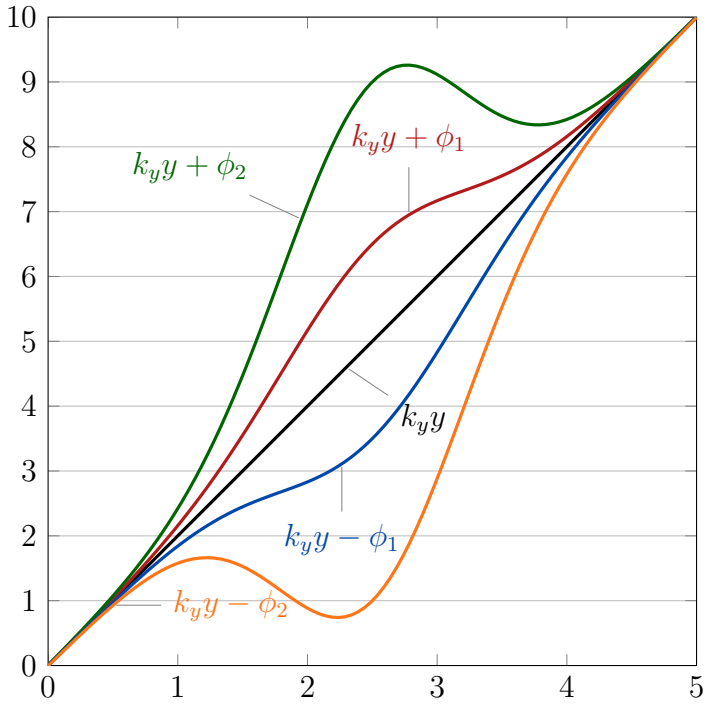

Figure 3.7: Graph showing a lineout of phase along an interferogram with carrier phase $k_y y$ and two possible object phases ϕ_1 and ϕ_2. ϕ_2 could not be unambiguously unwrapped from an interferogram because the combined phase $k_y y \pm \phi_2$ is not monotonically increasing.

$$k_y > \left| \frac{\mathrm{d}\phi}{\mathrm{d}y} \right| \tag{3.7}$$

This gives us a hint of a few ways to avoid ambiguity in interference patterns. We can increase k_y or find a way to reduce $\left| \frac{\mathrm{d}\phi}{\mathrm{d}y} \right|$. A few methods of this are discussed below and illustrated in figure 3.8.

Effect of Fringe Spacing

A tighter fringe spacing increases k_y, and by extension the $\frac{\mathrm{d}\phi}{\mathrm{d}y}$ that can be unambiguously probed. This can be achieved by manipulating optics to adjust the relative position of the focal points and detector as described in Figure 3.2. In gen-

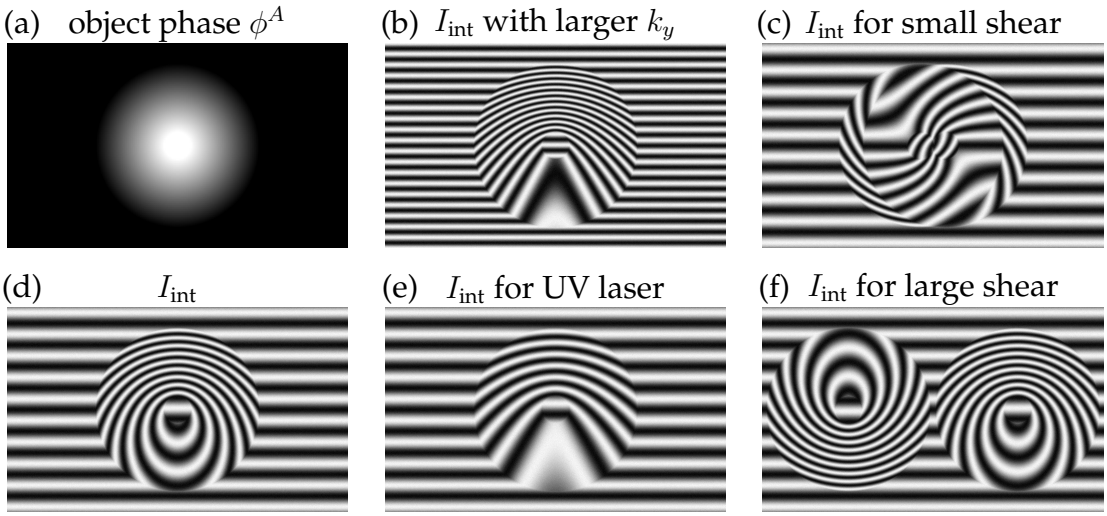

Figure 3.8: (a) The object phase ϕ^A is a flat-topped cone. (d) The interferogram formed with ϕ^A is ambiguous because $\left|\frac{\mathrm{d}\phi}{\mathrm{d}y}\right| > k_y$. (b) By increasing k_y, we can form an unambiguous fringe pattern with tighter fringe spacing. (e) Alternatively, switching to a shorter-wavelength laser effectively reduces ϕ for the same plasma density n_e. (c) A sufficiently small shear can reduce ambiguity by reducing the effective object phase in the interference pattern, but a more complicated analysis is required to pull out ϕ^A. (f) A large shear just gives two copies of the original pattern, but with opposite phase.

eral, a higher fringe density (smaller fringe spacing) leads to better (higher resolution and contrast) interferograms. This correspondence runs into two main problems. Eventually the detector cannot resolve smaller and smaller fringes, so the carrier phase pattern ought to be adjusted such that fringes formed by the total phase are not so tightly packed as to be indistinguishable. Secondly, imaging effects such as diffraction can lead to competing fringe-like patterns overlayed on an interferogram that are not directly related to the desired object phase ϕ and ought to be ignored in interferometric analysis. These limitations are considered further in Section 3.4.4.

Effect of Laser Wavelength

A shorter wavelength laser (e.g. ultraviolet instead of green) would reduce the object phase shift for a given density, allowing for the probing of higher densities. This happens because of the relationship of λ and ϕ in Equation 3.6 and can be intuitively thought of as the higher energy photons being less perturbed by the bulk electron plasma density.

Effect of Shearing

Shearing produces two copies of the object phase ϕ which then interfere with one another. In the small-shear case, the effective phase of the interferogram involves the difference of the sheared object phases ($\phi(x, y) - \phi(x + \delta, y)$). Because of this, a small shear can be useful for avoiding ambiguous fringe patterns. However it will take more effort to decipher the true object phase. A large shear involves little overlap between the segments of beam with significant object phase, giving two distinct copies of ϕ.

3.4.3 Implementation

Interferograms captured in this dataset had a high fringe density of $4\,\mathrm{cm}^{-1}$ in the unperturbed case. Raw images from the experiment were digitally expanded (magnified) and the fringes were manually traced onto a binary (black and white) layer. This eliminated the possibility for any ambiguity or error introduced by FFT-related interferogram smoothing and denoising algorithms. A simple counting script was run on the binary fringe layer to number each fringe. Cells between fringes were then linearly interpolated along lines running perpendicular to the unperturbed fringe orientation. This was used as an input to a variation-minimizing Gauss-Seidel relaxation routine, which smoothed the

dataset but kept the fringe-count value on each fringe constant. The implementation of these analysis methods is discussed further in Appendix B.

3.4.4 Limitations

Diffraction Effects

As mentioned earlier in this chapter, diffraction effects become important when the scale-length of spatial variations in the plasma is comparable to the laser light's wavelength ($0.5\,\mu$m). This produces artifacts which typically appear as narrow fringes perpendicular to large gradients[4] in plasma density. These fringes, if they are a similar size to interferometric fringes, could cause issues with analysis and lead to incorrect interpretation of the fringe pattern. For this reason, it is can be advantageous to set up an interference pattern such that the fringes run parallel to the direction of the strongest expected gradients. As an example, in most shots with the collimated radial foil jet (with strong horizontal gradients due to the jet edge and weak vertical gradients), we set up the fringe pattern such that unperturbed fringes were horizontal. This gives us the ability to count fringe lines down along the weak vertical gradients, which allows for connectivity of the pattern in the event that diffraction effects near strong gradients make the fringe pattern ambiguous in those regions.

Detector Resolution

The finite resolution of the detector puts a limit on the density of fringes that can be resolved. The tightest reasonably distinguishable spacing for well-contrasted fringes is about 5 pixels (px). Less spacing than this could result in difficult-to-

[4] the diffraction fringes run parallel to sharp edges, which are perpendicular to strong gradients

interpret interferograms. Assuming our detector image sensor has the dimensions[5] ($22.3\,\text{mm}\times14.9\,\text{mm}$) and ($5184\text{px}\times3456\text{px}$), which gives us a linear pixel density of $4.3\,\mu\text{m}\,\text{px}^{-1}$, we want to the keep the fringe wavelength at least $20\,\mu\text{m}$. Referring back to the discussion in Section 3.2 and Figure 3.2, this gives us the requirement (when using a green laser) that $\frac{R}{d} > 40$. This is why the interfering beams' focal points must be so close together.

3.4.5 Abel Inversion

In order to take the line-integrated areal electron number density and get the more useful volumetric density n_e, some assumptions need to be made about the distribution of the plasma. In the simplest case and as a zeroth-order approximation, n_e can be assumed to be constant throughout the extent of the plasma L. This is a reasonable assumption in a few geometries, such as looking along the axis of a wire array z-pinch. For situations with cylindrical symmetry, such as the hydrodynamic jets formed by exploding radial foils, methods using the inverse Abel transform can very accurately unwrap a radial distribution $n_e(r)$ of density.

Definition

The Abel transform, named for Niels Henrik Abel, expresses the relationship between the radial dependence of a function $f(r)$, and the projection of the integral of that function along an axis $F(y)$. The forward transform (integrating radial data) can be written as:

$$F(y) = 2\int_y^\infty \frac{f(r)r\mathrm{d}r}{\sqrt{r^2-y^2}} \tag{3.8}$$

[5] like an APS-C sensor found in our consumer DSLRs

The reverse transform is:

$$f(r) = -\frac{1}{\pi}\int_r^\infty \frac{\mathrm{d}F}{\mathrm{d}y}\frac{\mathrm{d}y}{\sqrt{y^2 - r^2}} \tag{3.9}$$

A derivation of these is given in Appendix A.

Numerical Implementation

A simple and direct method for numerical Abel inversion breaks the integral into a sum of integrals over unit-length domains. For each of these integrals, the term $\frac{\mathrm{d}F}{\mathrm{d}y}$ is assumed constant, and the integration is explicitly carried out. This gives an inversion of the form:

$$f_i = -\frac{1}{\pi}\sum_{n=0}^{N-1-i} F'_{i+n} \ln\left(\frac{\sqrt{n^2 + 2in + 3n + 2i + 2} + (i + n + 1.5)}{\sqrt{n^2 + 2in + n} + (i + n + 0.5)}\right) \tag{3.10}$$

Similarly, the forward Abel transform can be written discretely as:

$$F_i = \frac{2R}{N}\sum_{n=0}^{N-1-i} f_{i+n}\left[\sqrt{n^2 + 2n + 2i + 2in + 1} - \sqrt{n^2 + 2in}\right] \tag{3.11}$$

A derivation for these is also given in Appendix A.

CHAPTER 4

EXPERIMENTAL DESIGN

This chapter describes the experimental apparatus used in these investigations. This includes the *driver* (source of energy), *load* (target of energy), and several diagnostics used for collecting data from the experiment.

4.1 COBRA

4.1.1 Overview

The pulsed-power driver COBRA [14] (COrnell Beam Research Accelerator) nominally provides a current pulse peaking at $1\,\mathrm{MA}$ to an inductive load ($\sim 10\,\mathrm{nH}$) with a rise time of $100\,\mathrm{ns}$. COBRA has been used for the study of wire array z-pinches and x-pinches, gas puff z-pinches, and several configurations of foil and liner research. It is a bipartite machine mirrored about its saggital plane. Each half of COBRA is driven by a Marx generator of sixteen $1.35\,\mu\mathrm{F}$ capacitors which store a total of $106\,\mathrm{kJ}$ when charged to the standard operating voltage of $70\,\mathrm{kV}$. Manipulation of the gasses in the self-breaking output switches of COBRA can allow for operation in *long-pulse mode*, which is characterized by a rise-time of $150\,\mathrm{ns}$ to $250\,\mathrm{ns}$ and a peak current below $1\,\mathrm{MA}$. Long-pulse operation can also result unintentionally from electronic jitter in Marx triggering, firing, or switch operation. Due to all these factors and their inherent unpredicatibility, there can be significant variation in the pulse shape and magnitude. It is important to control for this in analyzing results, as different COBRA pulses provide different environments for the development of the plasma. Most of the work discussed in this dissertation involves short pulses on COBRA (rise times of $90\,\mathrm{ns}$ to $110\,\mathrm{ns}$ reaching peak currents of $0.9\,\mathrm{MA}$ to $1.1\,\mathrm{MA}$). Exceptions are

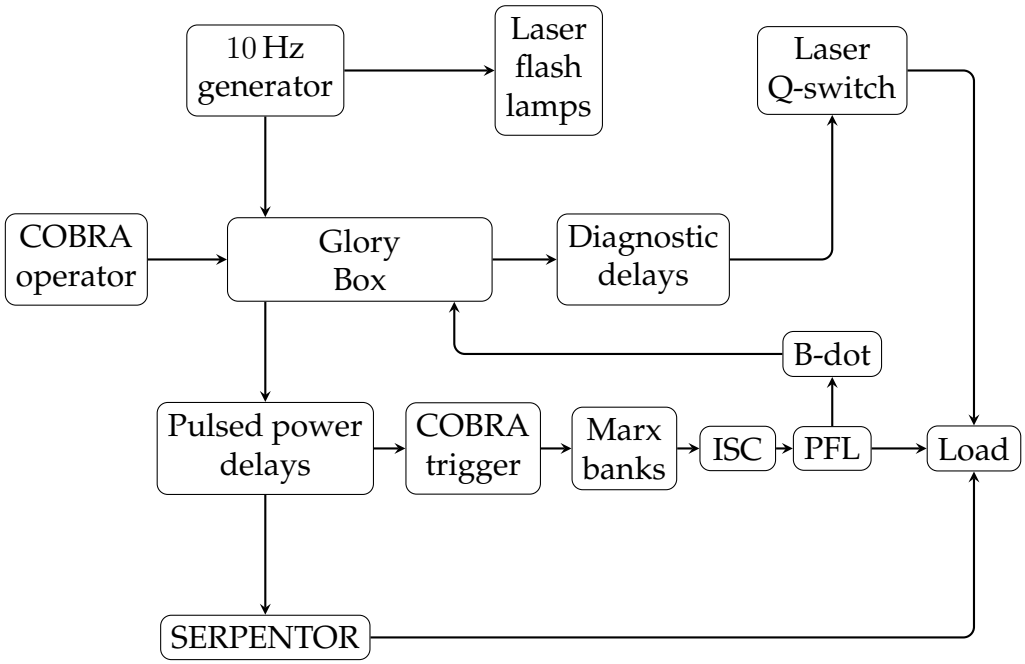

Figure 4.1: Simplified flowchart of COBRA diagnosic coupling. 'Laser' refers to the 120 ps diagnostic laser. Modifications are necessary when operating the gas-puff or the new high energy laser (not used with these radial foil loads).

indicated by quoting a time as t_{LP}, which means we are not dealing with a comparable short rise-time current pulse.

4.1.2 Diagnostic Coupling

Because of the sensitivity of lasers to timing, COBRA's triggering is slaved to the diagnostic (short-pulse, 532 nm) laser. This is accomplished by a seemingly convoluted arrangement of delays and circuit logic controlled by the so-called 'glory box.' The following is a short overview of how this works and how diagnostics can be coupled into our system. Follow along in Figure 4.1.

A 10 Hz signal generator is the metronome that synchronizes everything around COBRA . It is constantly running and provides a signal to the diag-

nostic laser to run its flashlamps. This signal is teed off to also go to the glory box. When the COBRA operator presses the 'fire' button, a $22\,\mathrm{V}$ signal goes to the glory box. It waits for a set number of $10\,\mathrm{Hz}$ pulses, in order to get the timing right for proper Q-switching of the laser, then it sends out a signal that goes to a delay generator which fires the PT-55 in COBRA's trigger sequence. This is also the point where the SERPENTOR trigger is inserted in parallel with COBRA's. SERPENTOR has a relatively slow rise-time, so the high jitter of the experiment relative to this point is not an issue. A set of B-dot probes on the pulse forming lines (PFL) send signals to the glory box when the COBRA current pulse reaches that point. These lead to the triggering of a diagnostic delay box, which allows for low jitter triggering of the diagnostic laser Q-switch and XUV pinhole cameras. Recent developments in gas-puff experiments, such as requiring that pre-ionizer has broken down the gas before delivering current to the load, have changed some of the particulars of the early triggering process since my work was carried out. The acquisition of the new $10\,\mathrm{J}$ laser intended for use in optical Thomson scattering experiments will require its integration into this trigger sequence, perhaps as a slave off the diagnostic laser.

4.2 Load Hardware

The current pulses from COBRA's four output switches are combined in the aptly named *adder* which sits under the load region. A magnetically-insulated transmission line (MITL) brings current up the cathode stalk to the A-K gap at the load. This 'magnetic insulation' is due to the very high currents in the line and necessary because of the high voltage of the transmission line's midplane. The voltage is high enough ($\sim 1\,\mathrm{MV}$) and the gap small enough, that

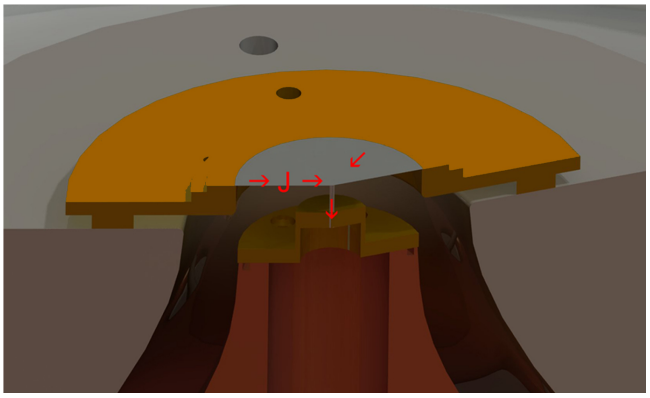

Figure 4.2: A cutaway CAD view of the 'Type A' hardware used for firing radial foil loads.

field emission of electrons[1] from the midplane would cause conduction across the gap which would short circuit the load. This is prevented by the magnetic field produced by current running through the transmission line. With a large enough current, the field-emitted electrons launched into the vacuum gap are deflected back towards the center conductor. This magnetic insulation effect is an important consideration for hardware design.

A radial foil load is characterized primarily by the thickness of the foil and the radius of the cathode pin which provides electrical contact to the driver. A thicker foil tends to slow down the dynamics, as there is more material to melt and ablate. A larger cathode pin also slows things down, as it reduces the maximal current density on the foil. This leads to smaller maximal magnetic fields, and in turn smaller forces pushing ASP and foil material upwards. Two main configurations of load hardware have been used in these experiments. The first (type A, pictured in Figure 4.2) is quite similar to that used in previous work with radial foils on COBRA [10, 12, 9, 11, 13]. It keeps the foil relatively low and close to the anode plane to minimize the load inductance. It is compatible with

[1]COBRA is designed such that high voltages are negative with respect to ground

several variations of magnet holders for permanent magnet experiments. The second (type B) has an extension of the cathode stalk to put the foil near the center of the Helmholtz coil (described in Chapter 2).

4.3 Applying a magnetic field

4.3.1 Permanent magnets

Neodymium Iron Boron (NIB) magnets are a kind of very strong, readily available, permanent magnet. We purchased many, in a variety of shapes and sizes, from K&J Magnetics. Depending on their aspect ratio, NIB magnets have a remanence (magnetic field strength) of about one tesla. The field around a permanent magnet can be approximated by calculating the field due to imaginary surface currents perpendicular to its magnetization. The magnitude of these currents is set to give the proper remanence value inside the magnet.

I explored using several different configurations of NIB magnets to impose magnetic fields on the exploding foil. I was initially interested in applying a transverse field to the jet because the strongest, most uniform fields could be made this way. But to keep field uniformity and strength up, the spacing between the magnets must be smaller than the magnets themselves. Figure 4.3 shows a piece of hardware developed to achieve this. Having the magnets too close to the jet could perturb it in unintended ways. The square hole was designed to account for this by putting the cathode pin at the center of a symmetric conductor.

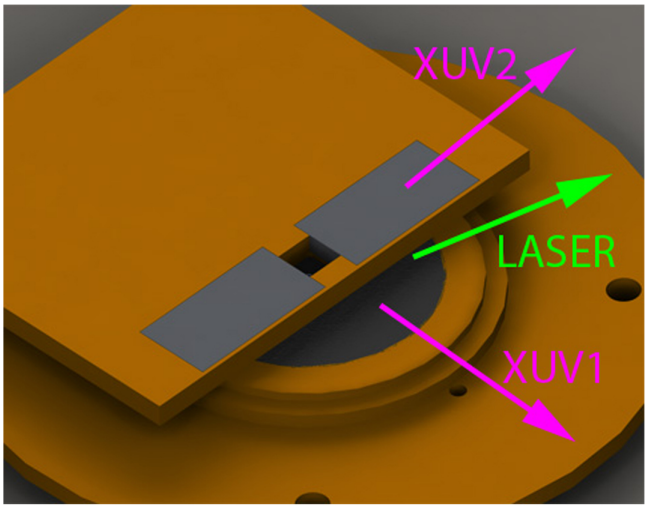

Figure 4.3: A CAD view of the brass magnet holder used in many of the experiments with NIB magnets. The central cathode pin is vertically aligned with the square hole between the magnets by sight.

4.3.2 Helmholtz coils

The design of the Helmholtz coils used for this experiment is described in depth in Chapter 2.

4.4 Diagnostics

The COBRA vacuum chamber with lines-of-sight of interest is diagrammed in Figure 4.4. The main diagnostics of interest for this work are XUV emission pinhole cameras, green-laser-backlit shadowgraphy and interferometry, and spatially-resolved, time-gated optical spectroscopy. Each of these is described in the following sections. Recent changes (Spring 2014) to the COBRA experiment include a new vacuum chamber with much larger windows for getting a full view of gas-puff experiments. This has changed the appearance of some of these diagnostics, but their implentation is roughly the same.

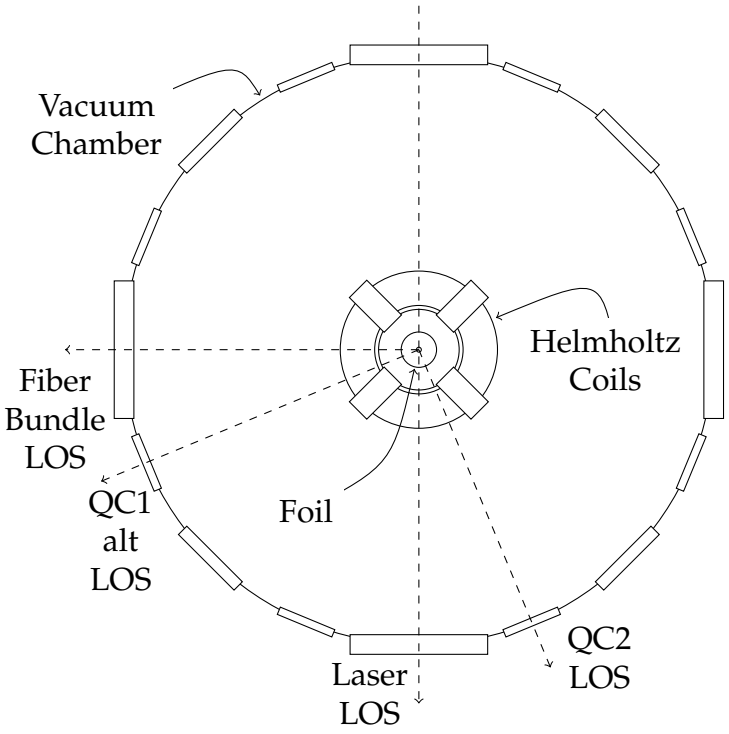

Figure 4.4: An axial view of the COBRA load and diagnostics shows lines-of-sight for the main diagnostics. QC1's standard viewpoint is the same as the figure perspective, magnified to just see the full extent of the foil. An alternate viewpoint, used in early experiments, provides a view perpendicular to QC2's.

4.4.1 Laser Shadowgraphy & Interferometry

A $120\,\text{ps}$, $532\,\text{nm}$ (frequency-doubled ND-YAG) EKSPLA laser provides coherent light for spatially and temporally resolved backlighting and interferometry. Before entering the experimental chamber it is split into three separate paths of distinct lengths allowing us to probe the experiment at three times separated by $\sim 10\,\text{ns}$. These three beams enter the COBRA chamber at a very small ($< 5^\circ$) angle with respect to one another and intersect at the load. They are collected by separate sets of focussing optics, including a compound lens, and recorded with off-the-shelf consumer DSLR CCD cameras (Canon Rebel 3XTi). Beam splitting and recombination for interferometry is accomplished between the focussing

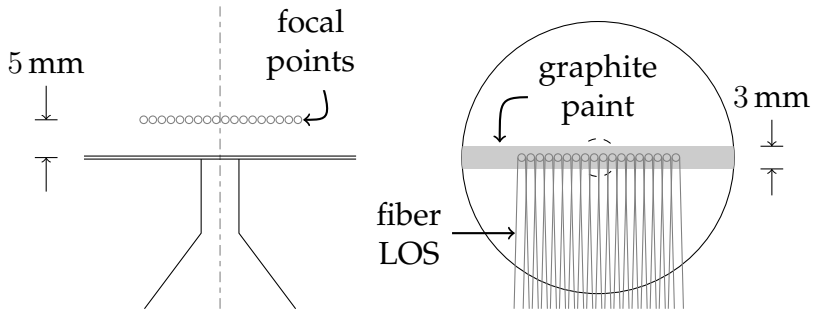

Figure 4.5: This cartoon explains the carbon seeding for the spectroscopic diagnostic, showing the location of the graphite paint and the positions of the fiber bundle focal points and lines-of-sight.

optics and camera with an air-wedge shearing interferometer [23]. Chapter 3 addresses the theory and practical analysis of interferometry relevant to these experiments.

4.4.2 XUV imaging

Two sets of 4-frame pinhole quadrant cameras (*QUAD-cams*) give spatially and temporally resolved images of the plasma where it is warm and dense enough to emit light collected through $200\,\mu$m pinholes and detected by the multi-channel plate (MCP) intensified CCD cameras. The MCPs are triggered to provide four $\sim$3 ns-long exposures separated by $10\,$ns. In these experiments there is one set of QUAD-cams (QC1) positioned along the axis looking at emission from hot plasma above the foil. This captures striking images of the thermally-unstable ASP. Another set of QUAD-cams (QC2) sees the plasma development side-on and clearly shows the profile and development of the axial jet.

4.4.3 Spectroscopy

After an early experiment showed evidence of an azimuthal velocity induced by the applied B_z, it was decided to implement a spectroscopic diagnostic to look for a Doppler shift in emission lines in the ASP around the jet. This work uses an ultra-fast gated Gen 3 ICCD camera from Andor (model DH340T-18U-63) coupled with an Andor SR750 Czerny-Turner spectrometer that has a focal length of 750 mm, with a 2400 lines per mm grating blazed for 400 nm. With a custom lens for spectroscopic imaging, this setup allows for a spectral resolution better than 0.4 Å. An 18-fiber bundle collects light from focal points spread across the radius of the foil, 5 mm above the foil. To provide enough light for analysis, spectra are integrated over 40 ns near the peak of the current pulse. Although Al spectral lines were too weak to make conclusive measurements, a C-III doublet was visible which was further enhanced by seeding the foil with carbon. A 3 mm-wide stripe of graphite (Aerodag-G) was painted on the foil perpendicular to the line of sight of the light-collecting fiber bundle. This arrangement is diagrammed in Figure 4.5. The thin graphite stripe was used because having excess carbon (painting the whole foil) ablated into the fiber lines-of-sight made subtle Doppler shifts unobservable. Experiments verified that the carbon does not move far (along the line-of-sight direction) from its seeding position over the integration time. When this small quantity of graphite ablates, it significantly increases the population of C atoms in the plasma without having a noticable effect on the overall plasma dynamics as observed with the interferometry and XUV-emission diagnostics. The additional carbon gives a much stronger signal that can be analyzed to find the Doppler shift due to the rotation of the ASP. Because of the high collisionality of the ASP ($\nu_i > 10^9\,\mathrm{s}^{-1}$) relative to our timescale of interest, is it reasonable to say that the carbon tracer atoms move in the same

sense as the aluminum plasma. Their effect on the magnitude of that motion is not addressed in this work.

4.4.4 B-dot probes

The change in a magnetic field over time can be measured by monitoring the voltage induced in a conducting loop encircling some of the field lines thanks to Faraday's Law:

$$\nabla \times \mathbf{E} = -\frac{\partial \mathbf{B}}{\partial t} \tag{4.1}$$

Integrating this equation over the area of the loop, applying Stokes' theorem and the definition of voltage, and assuming that the field is well-behaved (mathematically), we can write the following:

$$V = A\frac{\partial B}{\partial t} \tag{4.2}$$

Here V is the voltage across the loop, A is the area of the loop, and B is the average value of magnetic field only counting flux that goes through the loop. This means that we can set up probes that look at specific components of $\mathbf{B}$ by proper construction and orientation of this loop. In COBRA experiments, significant magnetic fields can develop quite quickly. If the loop area is too large[2], these fast field changes will cause high voltages that can break down the probe insulation. John Greenly's B-dot probes account for this by having a very tiny area, a trait which makes their production and calibration a bit more technical than that for a simple $1\,\mathrm{cm}^2$ loop I used for measuring the SERPENTOR B-field.

[2] As an example, for a $1\,\mathrm{cm}^2$ loop with $1\,\mathrm{T}$ in $10\,\mathrm{ns}$ field change, there will be $10\,\mathrm{kV}$ across the probe.

CHAPTER 5

EXPERIMENTAL RESULTS

This chapter explores all of the major experimental results relevant to the present investigation of magnetized hydrodynamic plasma jets on COBRA. Here we simply present the data with sufficient context for understanding its relevance. Discussion and analysis are in Chapter 7.

5.1 Campaign Overview

5.1.1 Timeline

Radial foil work has been a significant portion of COBRA's shot schedule since 2008. I became involved and began to run shots independently in September 2009. Figure 5.1 and Table 5.1 provide a timeline and outline of all my COBRA work since then.

5.1.2 Motivations

The first goal of this radial foil campaign was to learn about the formation and structure of the initial bright 'precursor' jet formed during a radial foil explosion by perturbing it with a strong magnetic field. My earliest experiments (COBRA shots 1604-1611) used coiled cathodes to produce a strong axial (or poloidal) field using the current drive of COBRA itself. These did not produce a noticable effect on the jet and were labor-intensive[1]. While the Helmholtz coil (described in Chapter 2) was being designed and produced, some COBRA shots (1789-1812) were run with radial foils and strong NIB magnets. These produced

[1]They required a cleaning of COBRA's adder rings after every shot due to excess debris from the coiled cathode.

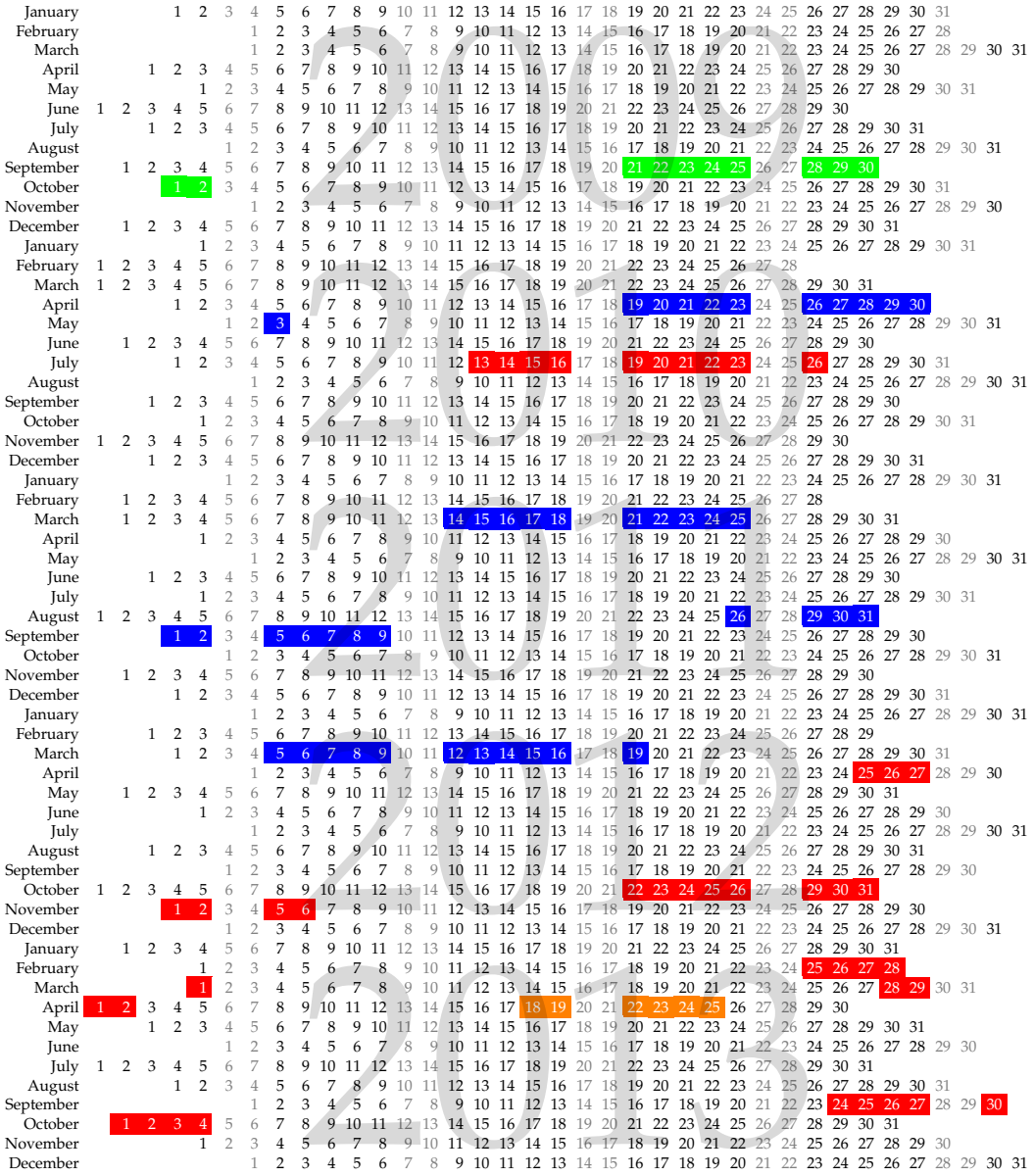

Figure 5.1: 5-year calendar overview of this experimental campaign. Colors indicate similar 'styles' of run, see Table 5.1 for details.

Table 5.1: Summary of my COBRA runs

Run	Dates	Shot #s	Notes
I	2009-09-21 to 2009-10-02	1604 -1611	Coiled Cathodes
II	2010-04-19 to 2010-05-03	1789 - 1812	NIB magnets
III	2010-07-13 to 2010-07-26	1876 - 1891	B_z coils
IV	2011-03-14 to 2011-03-25	2215 - 2138	NIB magnets
V	2011-08-26 to 2011-09-09	2280 - 2292	NIB magnets
VIA	2012-03-05 to 2012-03-19	2421 - 2441	NIB magnets
VIB	2012-04-25 to 2012-04-27	2484 - 2491	B_z coils
VII	2012-10-22 to 2012-11-06	2664 - 2687	B_z coils
VIII	2013-02-25 to 2013-03-01	2752 - 2763	B_z coils
IX	2013-03-28 to 2013-04-02	2793 - 2800	B_z coils
	2013-04-18 to 2013-04-25	2818 - 2833	KSB run with B_z coils for spectroscopic data
X	2013-09-24 to 2013-10-04	2972 - 2989	B_z coils to look for magnetic field compression

some interesting results, notably an apparent splitting of the jet as it crossed a transverse field. Closer investigation of this (COBRA shots 2280-2292) seemed to show the splitting was not reproducible and highly dependent on the alignment of the magnet hardware. Explorations with other configurations of NIB magnets (greater spacing and weaker fields during shots 2421-2441) led to the discovery of the current-carrying tendrils, which became a secondary focus of investigation. The most compelling and repeatable results with the jet have been achieved with the Helmholtz coil (COBRA shots 2484-2491 and 2664-2678). Efforts to learn about the possible rotation induced in the plasma by the ap-

plied B_z led to the development of the spectroscopic diagnostic. When simulations, which had shown strong agreement with the dynamics of the experiment, showed axial magnetic field compression, it became an experimental priority to demonstrate that.

5.1.3 Chapter Organization

Instead of following a linear timeline, the next sections of this chapter illustrate the patterns found in this work in a thematically-driven manner. We begin with results relevant to the formation of *tendrils* of current-carrying plasma along the upper surface of foil and their response to applied magnetic fields. Then we look at the axial *jet* itself, which has been the main focus of much of this work. The *rotation* of the ASP is explored at first grossly, then with a precise spectroscopic diagnostic. Finally we explore the possibility of B_z *compression* with small B-dot probes.

5.2 Tendrils

Narrow channels of high-intensity XUV emission have been observed via the axial pinhole camera diagnostic (QC1). Due to their appearance, we call these structures tendrils. The first experimental results involving them appears in Figure 5.2. These shots were at the beginning of an exploration to use larger cathode pins (up to $10\,\mathrm{mm}$) in an attempt to maximize the length and persistence of the initial hydrodynamic jet. Interest in the tendrils steadily grew.

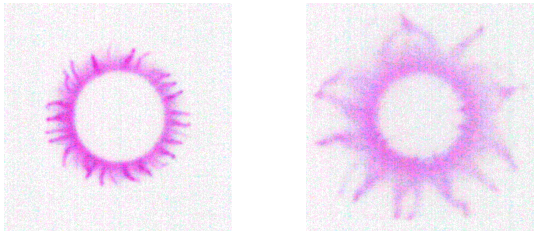

Figure 5.2: The first experimental evidence of the tendrils, from COBRA shots 2421 and 2422. These used a larger cathode pin (10 mm diameter), which is visible as the central gap in emission. This also helps to illustrate a general trend seen in this data. As the tendrils expand radially outward, they become larger and fewer in number.

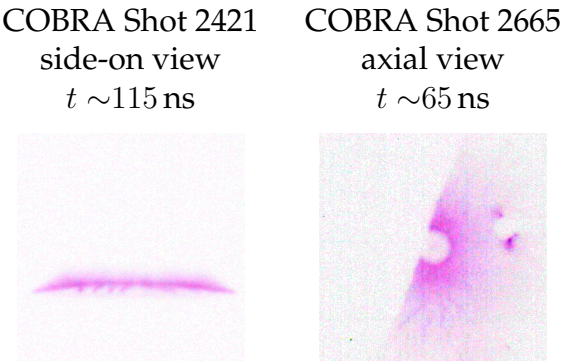

Figure 5.3: Evidence for the tendrils being on top of the foil, from COBRA shots 2421 and 2665. In the side-on view of shot 2421, structures resembling the tendrils can be distinguished on the top-side of the foil. For shot 2665, a sheet of 6 µm Al foil was placed ∼10 cm above the load foil (still far from the pinholes) as a filter to demonstrate its high attenuation of XUV emission. This is visible as a line cutting-off emission near the central cathode. A small hole torn in the foil to the right of the cathode shows enhanced emission near its edges (in two spots) and no emission from below the foil.

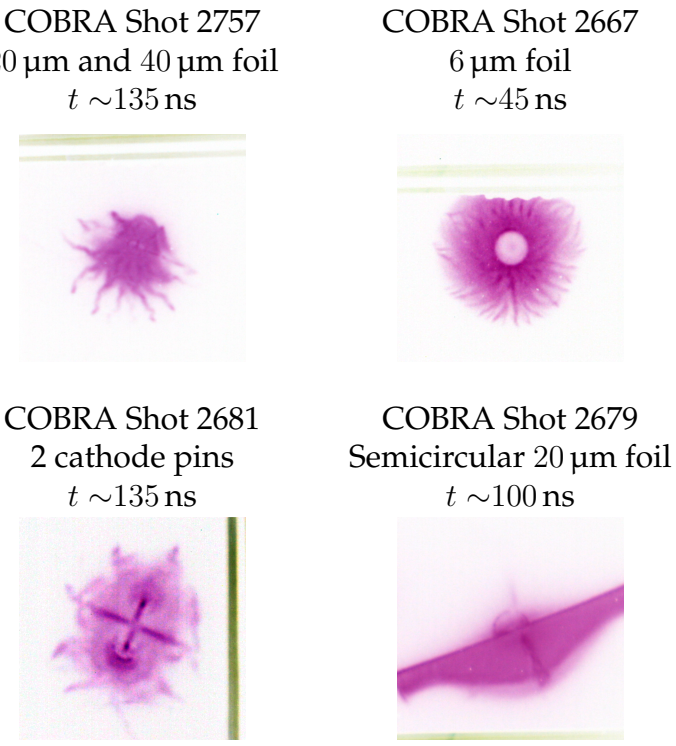

Figure 5.4: An illustration of the wide variety of situations where these tendrils appear. For shot 2757, we had a single layer of 20 µm Al foil across the whole circle and an additional layer across one half (upper right). All of these examples show some tendril structure, except for shot 2679, in which one half of the foil was removed prior to the shot. Because of the much higher current densities in this configuration, we are probably looking too late in time to see the tendrils.

5.2.1 Formation

A set of COBRA shots was performed to take a closer look at the nature of the tendrils. We established that they are on top of the foil, as shown in Figure 5.3. We also found that they appear in many different configurations. Figure 5.4 depicts this variety over a sample of exploratory shots.

During the current pulse of an exploding radial foil, the tendrils expand radially outward and eventually a brighter region of enhanced XUV emission develops around the cathode. There is a structure to this region that we will refer

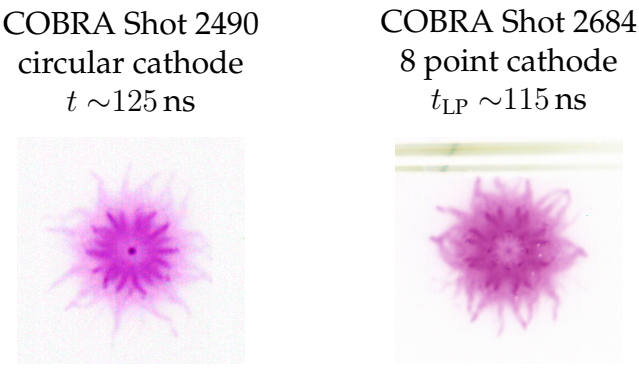

Figure 5.5: An attempt at seeding the tendril instability succeeded at providing some regularity to the inner spokes.

to as *spokes* in the coming discussion to contrast them with the tendrils.

Seeding

The pseudo-regular appearance of the tendrils made them a prime candidate for attempting to seed their structure. Figure 5.5 shows the results of an attempt at manipulating the tendrils by replacing the circular cathode pin with a segment of 8-point pinion gear stock.

5.2.2 Magnetic Field Interaction

NIB Magnets

Perturbing the tendrils with a small static magnetic field would allow us to see if they are current-carrying structures. Experiments were performed with a pair of 1 cubic inch (dangerous!)[2] NIB magnets mounted to either side of the radial foil load hardware. Depending on the relative orientation of these magnets, fields with lines parallel to or normal to the foil could be made. Figure 5.6 shows the effect of these weak fields on the tendrils.

[2]Owing to their strong attractive force which creates a pinching hazard.

COBRA Shot 2434
Transverse B_z
t_{LP} ∼165 ns, B ∼100 mT

COBRA Shot 2435
Downward B_z
t_{LP} ∼150 ns, B_z ∼50 mT

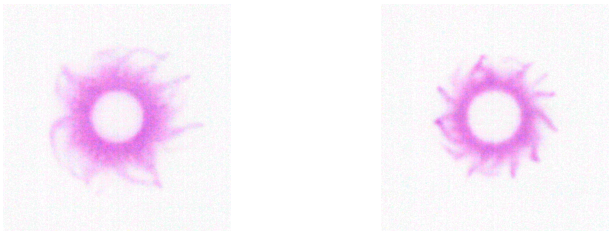

Figure 5.6: Weak field effect on tendrils (using far-spaced NIB magnets)

COBRA Shot 2675
Downward B_z
t ∼100 ns, B_z ∼130 mT

COBRA Shot 2676
Upward B_z
t ∼100 ns, B_z ∼130 mT

Figure 5.7: Reversing the direction of the applied B_z switches the sense of rotation of the tendrils.

B_z Coils

With the Helmholtz coils, we have the ability to vary the applied B_z over a large range (up to 1.5 T) by varying the charging voltage. Initial experiments looked at relatively small fields to try to reproduce the NIB results (See Figure 5.7). With these fields, the tendrils begin to run together. Stronger fields tend to reduce asymmetries up to a point, as summarized in Figure 5.8.

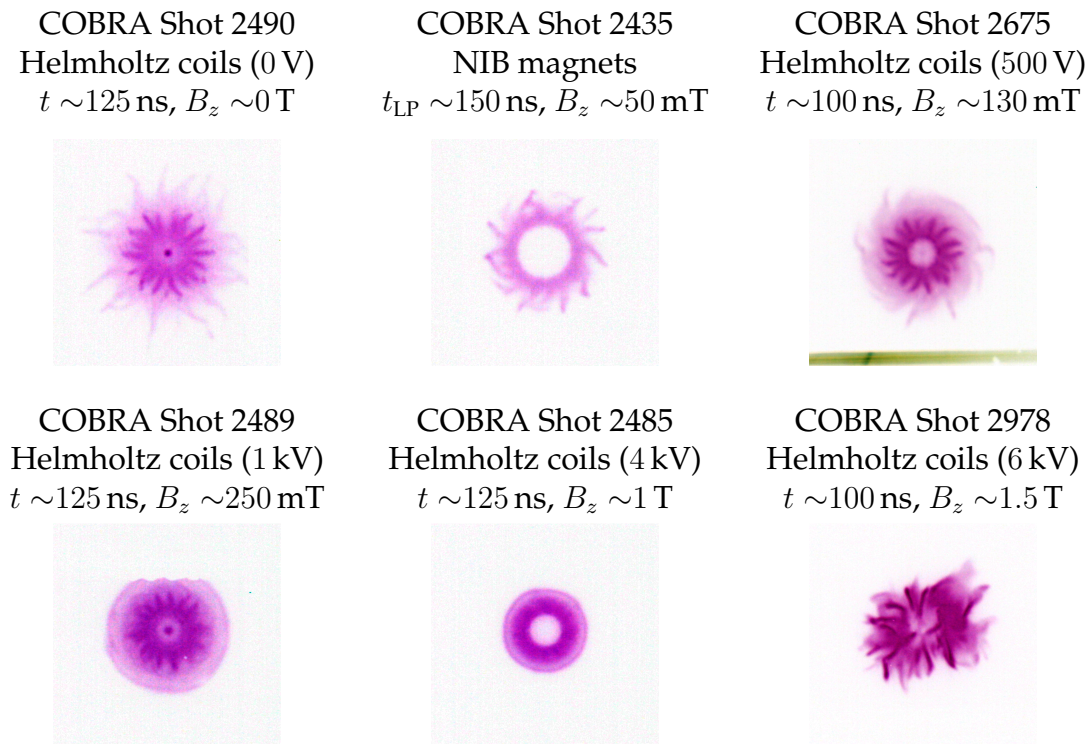

Figure 5.8: Summary of magnetic field effects on the tendrils. With increasing field strength, the outer tendrils wrap around until being eventually 'washed out.' The spokes still remain at ∼0.25 T, although with ∼1 T there is almost no azimuthal asymmetry. A strong instability appears somewhere between an applied field ∼1 T and ∼1.5 T

5.3 Jet

The jet has been the primary focus of this experimental investigation. This section covers results pertinent to the development of this hydrodynamic jet.

5.3.1 Previous Results

Radial foil experiments on COBRA and MAGPIE have produced an axial plasma jet. It has been referred to as the 'precursor' jet in work done at Imperial College. Its time of appearance varies depending on the machine current

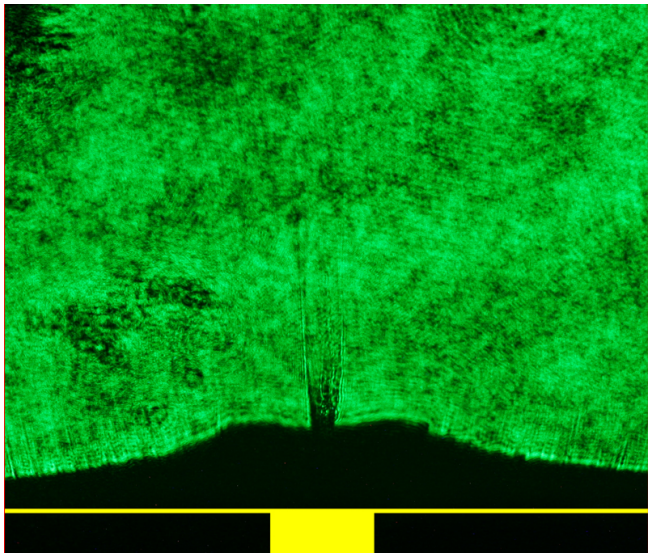

Figure 5.9: Laser-backlit shadowgraph of a radial foil jet from COBRA shot 1686 taken 90 ns after the onset of the current pulse. It shows the typical shadowgraph features of these jets. At the bottom in yellow we've added the initial position of the thin foil and the 2 mm cathode pin. Foil material is pushed up, which causes the curved shadow extending to the center. On axis, the jet has densities which approach an effective cut-off closer to the foil. Higher above, it is accentuated by diffraction features at its edges.

and the rate of surface plasma ablation (a function of foil thickness and cathode diameter). In many of the early COBRA experiments with radial foils (6 µm foils with 1 mm diameter cathode) the jet can be seen about mid-way through the current-rise of a 100 ns COBRA pulse. Figure 5.9 shows a laser-backlit view of one of these jets.

5.3.2 NIB magnets

The NIB magnets provide a quick and cheap way to impose a strong magnetic field on the experiment. Using the brass magnet holder described in Section 4.3.1, we are able to perturb the jet near the foil surface with a transverse field

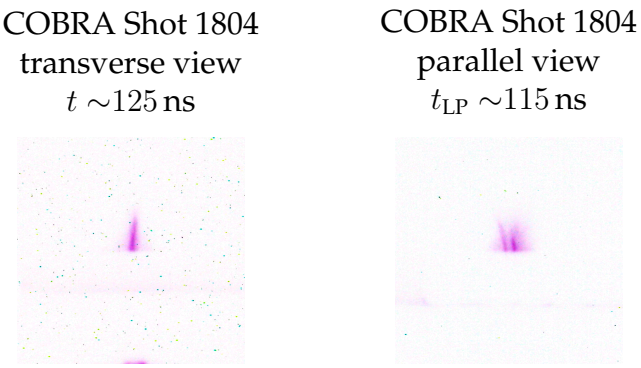

Figure 5.10: Apparent assymetric splitting of the jet due to a transverse field. Views are indicated relative to the applied magnetic field.

and then watch its propagation above the region of strong magnetic field.

Results

COBRA shot 1804 provided some of the most interesting results with NIB magnets. It showed an apparent assymetric splitting of the jet due to the transverse field. This is depicted in Figure 5.10. On this shot, QC1 was in its alternate position such that both QCs could give side-on images and be perpendicular to one another.

Issues

Subsequent attempts to reproduce the results from shot 1804 were unsuccessful. It is likely that the alignment of the 2 mm cathode pin and the 6.4 mm-wide square hole in the brass magnet holder had a stronger effect on the development of the jet than the transverse field. Figure 5.11 shows an axial QC1 view of this alignment sensitivity. A magnetic field effect cannot be ruled-out entirely, however. Figure 5.12 shows laser-backlighting images of these jets at late time. They show an effect, but not one as simple as was implied by shot 1804. I have

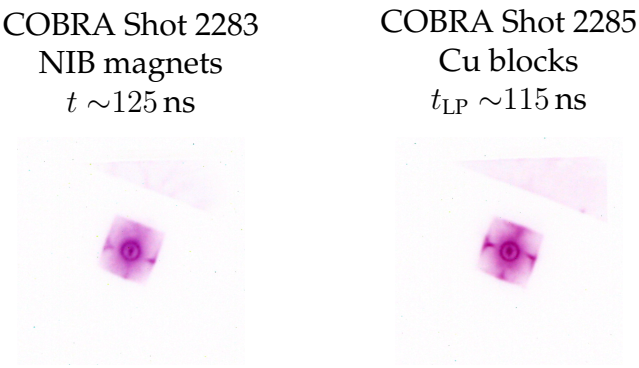

Figure 5.11: The jet visible on top of the brass magnet holder is very sensitive to the axial alignment of the magnet holder and the cathode pin. This figure shows the similar behavior of the jet when the magnets are replaced with copper blocks (the NIB magnets have a nickel-copper coating). The presence of the conducting surfaces so close to the jet is likely as significant to the jet development as the transverse magnetic field.

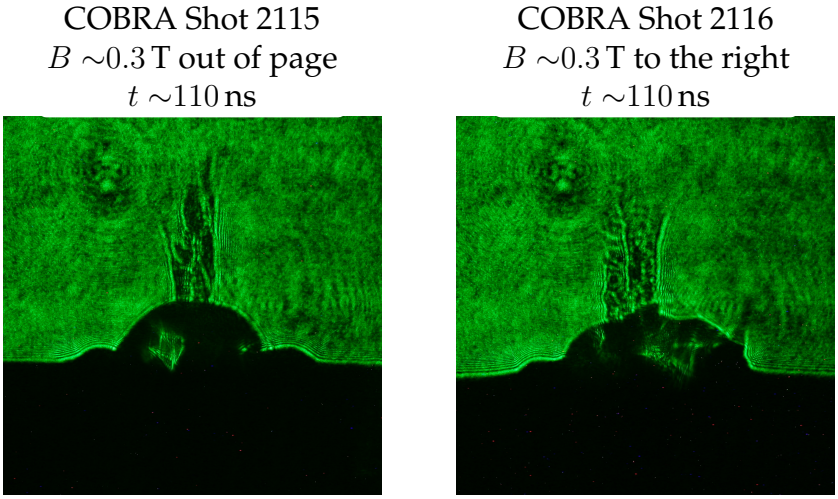

Figure 5.12: Experiments with NIB magnets that show a more complicated jet (with strong-gradients features along the center) than the standard radial foil jet. Applied fields quoted are in the region above the foil which is obscured by the magnet holder. The bottom of these images corresponds to the initial position of the foil. At this late time (for a thin foil), there is a significant amount of foil material erupting from the square hole in the magnet holder.

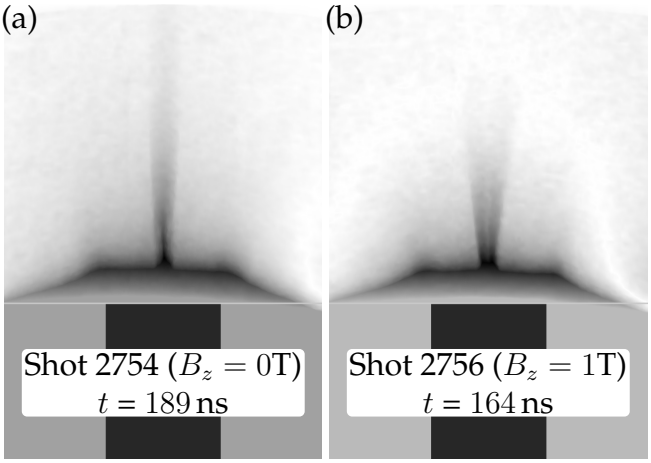

Figure 5.13: Side-on laser-backlit interferometry was processed to give this comparison of line-of-sight integrated phase shift ($\propto$ areal electron number density). Numerical Abel inversion gives volumetric densities approaching $10^{26}\,\mathrm{m}^{-3}$. (a) The no-field case shows the hydrodynamic jet familiar from previous radial foil work. (b) Adding B_z hollows the jet on axis and widens the angle of its divergence.

not seen similar images without the magnets. Because of these reproducibility issues, I decided to persue experiments with magnetic field coils that did not perturb the region of jet formation with conducting surfaces.

5.3.3 B_z Coils

Although I had at one point intended to build a pulsed solenoid that would provide a transverse magnetic field, results with the axial-field Helmholtz coil proved too interesting to discontinue. The results have shown a consistent and highly reproducible effect on the development of the jet. This is illustrated via laser interferometry in Figure 5.13 and side-on XUV emission imaging in Figure 5.14.

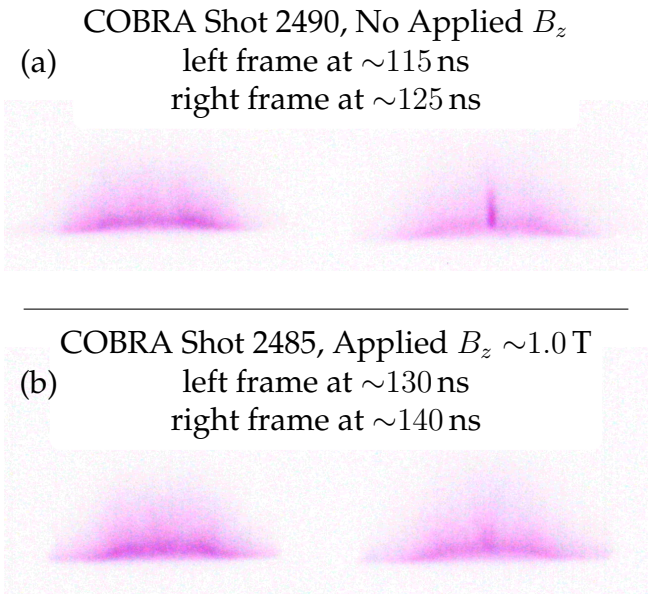

Figure 5.14: Side-on XUV emission imaging (QC2) shows the initial formation of the jet shortly after peak current on COBRA. (a) There is a distinct transition between these frames (spaced 10 ns apart) in which the jet becomes apparent. (b) In the case with the applied field, the formation of the jet is delayed by ∼15 ns.

5.4 Rotation

The behavior of the tendrils under the influence of applied magnetic fields made us suspect that the ASP underwent some azimuthal motion due to the fields. This section presents results supporting that idea.

5.4.1 Hints

To begin looking for this rotation, we inserted a thin rigid mylar 'flag,' which extended radially inward along the top of the foil. It extended vertically from about one millimeter above the foil to several centimeters above and radially from outside the foil edge to a few millimeters from the axis. Axial QC1 views of this flag during a shot with an applied axial magnetic field showed enhanced

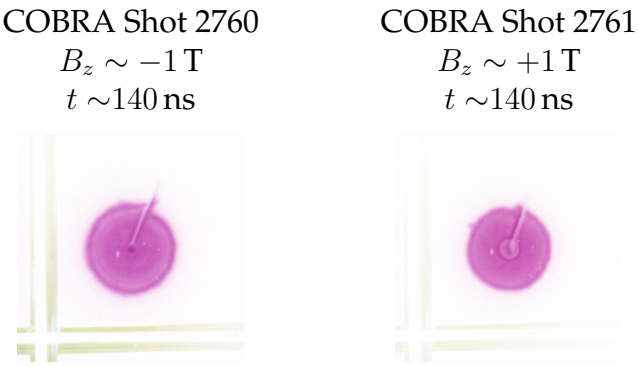

Figure 5.15: Changing the field direction switches the side that plasma builds up against the mylar flag. In these images, the white radial line corresponds to the thin strip of mylar. The dark region next to it is greater emission due to the ASP colliding with the mylar.

emission on one side of it. Switching the direction of the magnetic field changed the side of mylar with enhanced emission. This result is summarized in Figure 5.15.

5.4.2 Spectroscopic Results

The spectroscopic diagnostic described in Section 4.4.3 was implemented in order to make quantitative measurements of this ASP rotation. Figure 5.16 shows the major result. We found measurable Doppler shifts in the ASP that correspond to rotational velocities approaching $\sim 50\,\mathrm{km\,s^{-1}}$. The process used for analyzing this data can be found in Section 7.1.2

5.5 B_z Compression

Small B-dot Probes of the type described in Section 4.4.4 were used to look for expected B_z compression of the applied field on axis due to the ASP outflow.

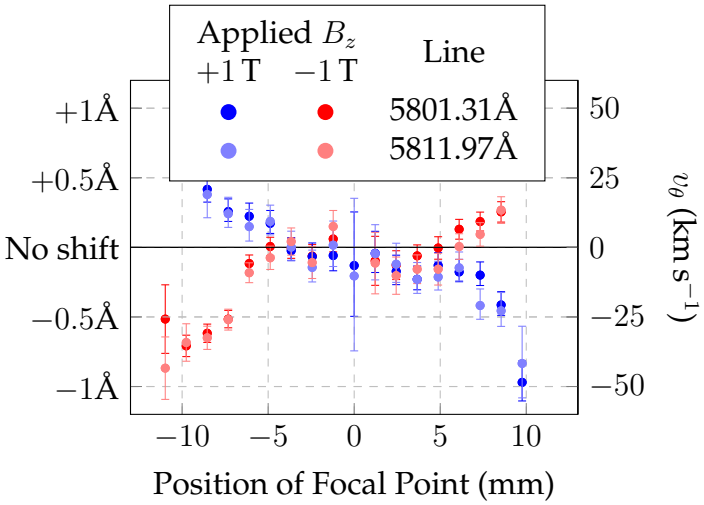

Figure 5.16: Processed spectra from two COBRA shots (2822 & 2823) with graphite painted on the foil to accentuate a C-IV doublet indicate a lineshift in the outer edges of the ASP for focal points >5 mm away from the axis. If this lineshift is interpreted as a Doppler shift, the outer ASP rotates at speeds $\sim 50\,\mathrm{km\,s^{-1}}$, as indicated on the right axis. The direction of the shift is consistent with the direction expected from $\mathbf{J} \times \mathbf{B}$ forces. The jet is nearly the same size as a focal point of a fiber and it emits relatively bright continuum radiation, so it cannot be effectively probed with this diagnostic.

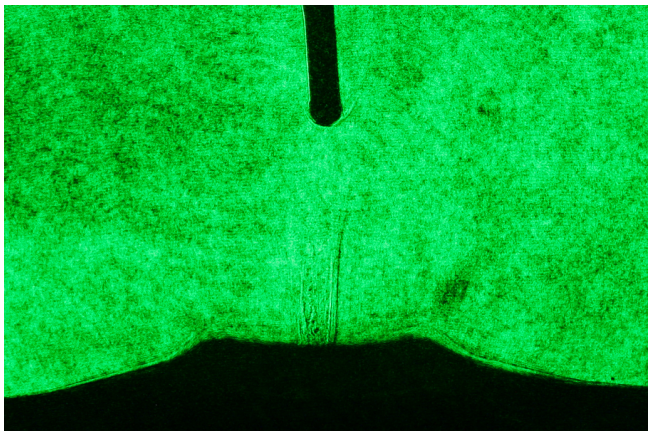

Figure 5.17: Laser shadowgraph showing the formation of a shock front against a B-dot probe placed along the jet axis.

Over several shots we recorded inconsistent and difficult-to-interpret B-dot measurements. On a later shot, laser backlighting demonstrated that relatively early-on, there is a noticable shock front forming around the edge of the probe. This is pictured in Figure 5.17. Thus the probe is likely a significant perturbation in this regime, and it's difficult to relate the probe reading to the actual change in field at that position without the probe.

CHAPTER 6

SIMULATION

This chapter discusses PERSEUS, a code developed at Cornell for the study of plasmas formed by exploding wires and foils. We explore its structure and strengths, and then apply it to study situations similar to the experiments described in Chapters 4 & 5. The simulation results shown in this chapter were provided by Professor Charles Seyler with my guidance on the experimental conditions.

6.1 PERSEUS

The initial goal of PERSEUS was the proper treatment of the plasma-vacuum interface using a generalized Ohm's law (GOL) which extends the standard MHD model. Its development was the core of Matt Martin's PhD work [19]. It has been used to study the relevance of Hall physics to new experimental work with radial foils [13].

We can develop the GOL used in PERSEUS beginning with the momentum equation ($\mathbf{F} = m\mathbf{a}$ analogue) for each species ($\alpha = e, i$ for electrons and ions, for simplicity we'll assume 1 ion species with charge Z and mass m_i)

$$\frac{\partial \rho_\alpha \mathbf{u}_\alpha}{\partial t} + \nabla \cdot (\rho_\alpha \mathbf{u}_\alpha \mathbf{u}_\alpha + P_\alpha \mathbf{I}) = \frac{q_\alpha \rho_\alpha}{m_\alpha} (\mathbf{E} + \mathbf{u}_\alpha \times \mathbf{B}) + \mathbf{R}_\alpha \tag{6.1}$$

We take $\frac{Ze}{m_i}$(Eq 6.1)$_i$ $-$ $\frac{e}{m_e}$(Eq 6.1)$_e$ to get the GOL:

$$\begin{aligned} \frac{\partial \mathbf{j}}{\partial t} + \nabla \cdot \left[\xi(\mathbf{uj} + \mathbf{ju} - \rho_c \mathbf{uu}) - \frac{1}{en_e}\mathbf{jj} - \frac{e}{m_e} P_e \mathbf{I} \right] = \\ \epsilon_0 \omega_{pe}^2 \left[\mathbf{E} + \left(\xi \mathbf{u} - \frac{1}{en_e}\mathbf{j} \right) \times \mathbf{B} \right] - \nu_{ei}(\mathbf{j} - \rho_c \mathbf{u}) \end{aligned} \tag{6.2}$$

By introducing nondimensionalized variables, e.g. $\mathbf{B} = B_0 \mathbf{B}$, we can nondimensionalize all the involved quantities against chosen scale parameters L_0, B_0.

Table 6.1: Values for Nondimensionalized GOL. ND-value refers to the unit value of a nondimensionalized variable. TE-range gives a typical experimental range of the variable in units of ND-value.

Symbol	ND-value	TE-range	Justification
L_0	$0.1\,\mathrm{mm}$		chosen
B_0	$1\,\mathrm{T}$		chosen
n_{e0}	$1.30 \times 10^{18}\,\mathrm{m}^{-3}$	1 to 10^8	Let $L_0\omega_{pe0} = \frac{B_0}{\sqrt{\mu_0\rho_0}}$
ω_{pe0}	$6.40 \times 10^{10}\,\mathrm{s}^{-1}$	1 to 10^4	Same as above
$v_0 = V_A$	$6.40 \times 10^{6}\,\mathrm{m\,s}^{-1}$	10^{-3} to 1	Same as above
ρ_0	$1.94 \times 10^{-8}\,\mathrm{kg\,m}^{-3}$	1 to 10^8	Same as above
j_0	$7.96 \times 10^{9}\,\mathrm{A\,m}^{-2}$	0.1 to 10^3	$j_0 = \frac{B_0}{\mu_0 L_0}$
E_0	$678\,\mathrm{V\,m}^{-1}$		$E_0 = v_A B_0$

Surprisingly, with just these two choices and several assumed relations between parameters, we can nondimensionalize every term. The most powerful relation is letting the Alfvén velocity be the scale velocity, or scale length times scale plasma frequency. In the equation $L_0\omega_{pe0} = \frac{B_0}{\sqrt{\mu_0\rho_0}}$, ω_{pe0} and ρ_0 are both functions of n_{e0}. Therefore, setting L_0 and B_0 sets n_{e0}, and the rest of the parameters follow. Table 6.1 gives the result of this nondimensionalization and shows the typical values for our experiments.

$$t = \frac{1}{\omega_{pe0}}t, \quad \mathbf{u} = L_0\omega_{pe0}\mathbf{u} = \frac{B_0}{\sqrt{\mu_0\rho_0}}\mathbf{u} = V_A\mathbf{u}, \quad \rho = \frac{B_0^2}{\mu_0 V_A^2}\rho,$$
$$\mathbf{j} = V_H e n_{e0}\mathbf{j} = \frac{B_0}{\mu_0 L_0}\mathbf{j}, \quad \rho_c = \frac{j_0}{u_0}\rho_c = \frac{V_H}{V_A}e n_{e0}\rho_c = \frac{B_0}{\mu_0 L_0 V_A}\rho_c,$$
$$V_H = \frac{B_0}{\mu_0 L_0 e n_{e0}}, \quad \mathbf{E} = V_A B_0 \mathbf{E}, \quad P = P_0 P$$

After substituting our new variables into Equation 6.2, a few lines of simplification gives us the nondimensionalized GOL:

$$\mathbf{E} + \mathbf{u} \times \mathbf{B} =$$
$$\frac{c^2}{V_A^2 n_e}\left(\frac{\partial \mathbf{j}}{\partial t} + \nabla \cdot \left[(\mathbf{uj} + \mathbf{ju}) - \frac{V_H}{V_A}\frac{\mathbf{jj}}{n_e} - \frac{B_0 e \beta_e}{m_e \omega_{pe0}} P_e \mathbf{I}\right] + \frac{\nu_{ei}}{\omega_{pe0}}\mathbf{j}\right) + \frac{V_H}{V_A}\frac{\mathbf{j} \times \mathbf{B}}{n_e} \tag{6.3}$$

We consider four different terms on the right hand side (bottom) of Equation 6.3 individually. They are:

1. Electron inertia
$$\frac{\lambda_e^2}{L_0^2 n_e}\left(\frac{\partial \mathbf{j}}{\partial t} + \nabla \cdot \left[(\mathbf{uj} + \mathbf{ju}) - \frac{\lambda_i}{L_0}\frac{\mathbf{jj}}{n_e}\right]\right)$$
2. Electron pressure
$$\frac{c^2}{V_A^2}\frac{B_0 e \beta_e}{m_e \omega_{pe0}}\frac{\nabla P_e}{n_e} = \frac{\lambda_i}{L_0}\beta_e \frac{\nabla P_e}{n_e}$$
3. Resistivity
$$\frac{c^2}{V_A^2 n_e}\frac{\nu_{ei}}{\omega_{pe0}}\mathbf{j} = \frac{\eta}{\mu_0 L_0 V_A}\frac{\mathbf{j}}{n_e} = \frac{1}{S}\frac{\mathbf{j}}{n_e}$$
4. Hall term
$$\frac{V_H}{V_A}\frac{\mathbf{j} \times \mathbf{B}}{n_e} = \frac{\lambda_i}{L_0}\frac{\mathbf{j} \times \mathbf{B}}{n_e}$$

By plugging in some typical parameters we can explore which of these terms is the most dominant for a given situation. Figure 6.1 helps to establish the importance of Hall physics in these experiments. One major benefit of PERSEUS is its ability to 'switch' on or off different terms so their effect and significance can be compared from one simulation run to the next.

6.2 Results

This section on simulation results is arranged in a manner intended to parallel the experimental results in Chapter 5. These two-dimensional XMHD simulations use cylindrical symmetry (r-z), which imposes azimuthal uniformity

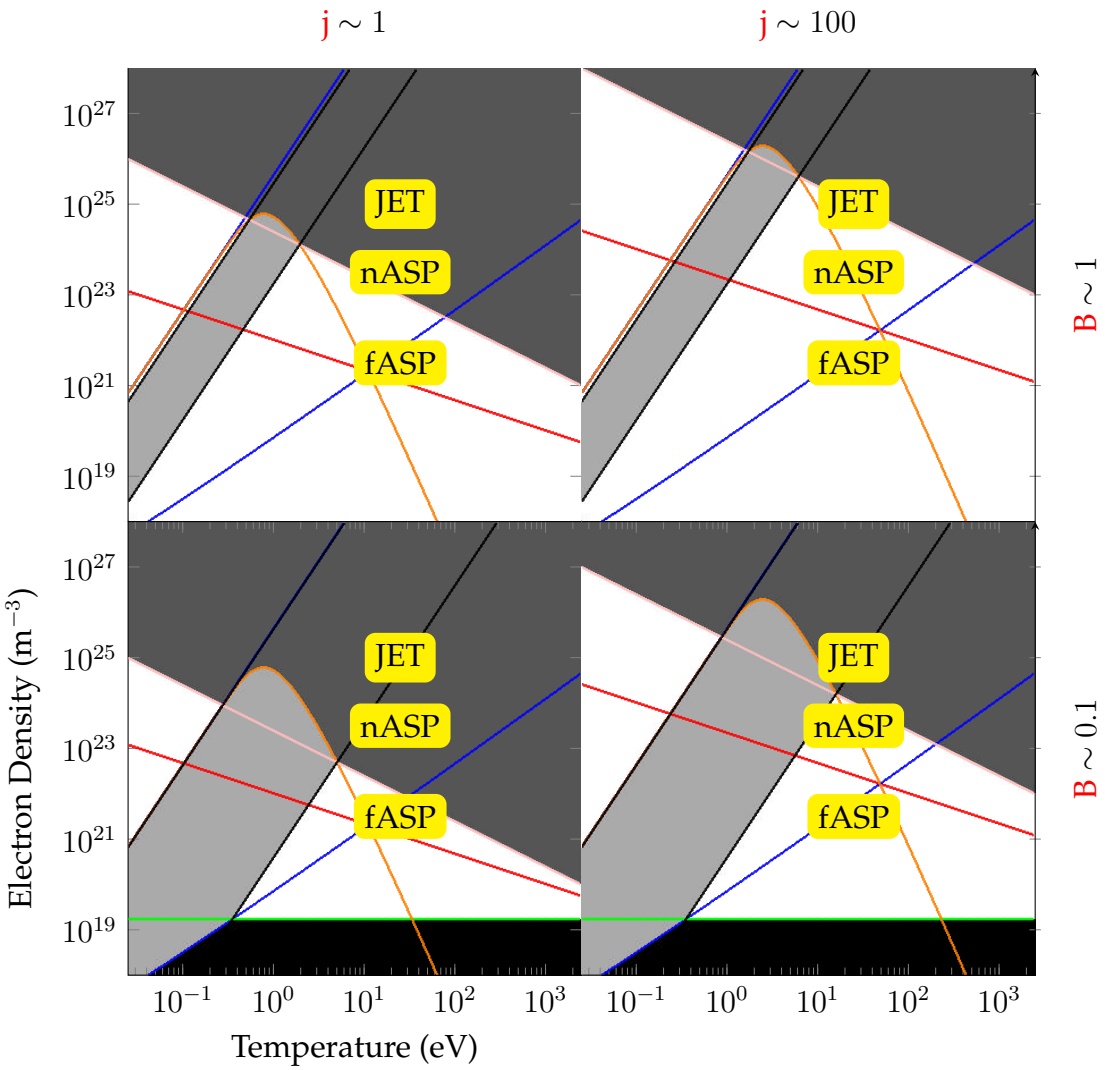

Figure 6.1: A plot showing the dominant term in our nondimensional GOL (Equation 6.3) over the given range of parameter space. The background colors indicate which term dominates with the following correspondence: black - electron inertia; dark grey - electron pressure; light grey - resistivity; white - Hall term. This figure demonstrates that although Hall physics may not dominate in the high density regions of the jet itself, it is very important for the lower density regions that merge to form the jet.

on the results. This is clearly nonphysical, considering the significant assymetries seen in the experiment. For the present investigation, the 2D simulations capture meaningful results that closely match the experiment. The work included in this dissertation had a (400×400) cell simulation grid running along ($0 < r <$18 mm,$-$4 mm$< z <$15 mm). The results have been mirrored along the axis to provide symmetrical images for comparison to the experiment.

6.2.1 Tendrils

A fair computational representation of the tendrils cannot be accomplished with a 2D (r-z) treatment. There are 3D versions of PERSEUS which could potentially simulate this behavior, but the high resolution necessary creates a large burden for processing and memory resources. 3D simulations have not yet been run to explore the formation of the tendrils, but it is likely that future simulation work will be able to shed light on the tendril/B-field interaction, especially with respect to the high-field instability.

6.2.2 Jet

The main goal of the simulation work is to make as direct comparisons to the experiment as possible. Interferometric measurements of electron density can be compared to simulation results of ion density (depicted in Fig. 6.2). The behavior of the simulation with the applied B_z qualitatively agrees with the experiment. To make direct numerical comparisons, an average ionization must be assumed. These simulations used $Z = 3$, which is reasonable because of the average expected temperatures in the region of interest (~ 50 eV).

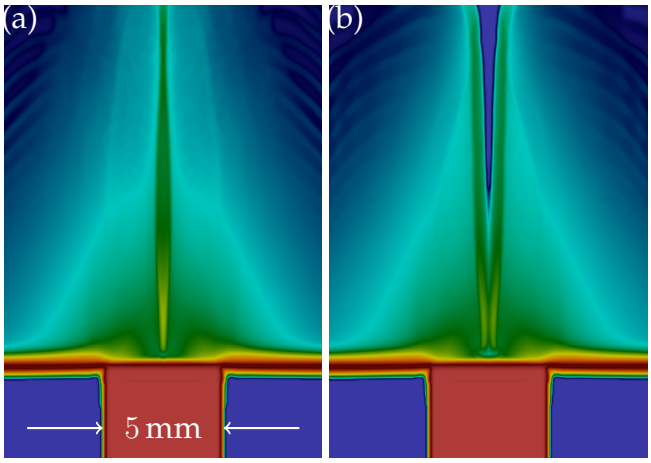

Figure 6.2: A PERSEUS simulation of an exploding radial foil is pictured as a log-plot of ion number density. (a) The no-field case shows a narrow jet with a small angular divergence. The jet's density does not significantly dip on axis. (b) With a $1\,\mathrm{T}$ B_z, the jet is wider, more divergent, and has a distinct axial hollowing.

6.2.3 Rotation

The Doppler shift indicated by the spectroscopic diagnostic provides experimental evidence of an azimuthal velocity in the fASP. Figure 6.3 shows v_θ in the simulation with B_z. Ignoring the jet itself, the general trend of increasing velocity far from the jet matches the experiment.

6.2.4 B_z Compression

A secondary goal of the simulation work is to search for physical explanations for dynamics using parameters not easily accessible in the experiment. It is difficult to do in-situ probing of magnetic fields without perturbing the plasma significantly. The simulation results show a compression of the applied magnetic field onto the axis (see Fig. 6.4) that is likely responsible for the modified behavior of the jet. The initial B_z is enhanced on axis by a factor ~ 4 in the

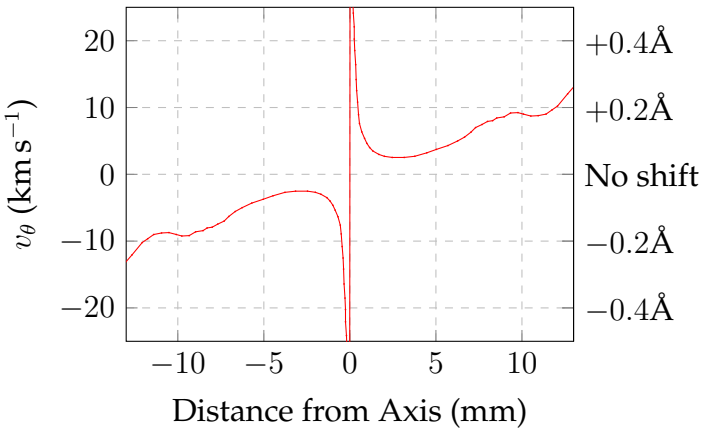

Figure 6.3: Because of the implicit azimuthal symmetry in the $r-z$ simulation, the azimuthal fluid velocity v_θ is everywhere zero in the absence of an applied B_z. With a 1 T B_z, a line-out of $v_\theta(r)$ for z =5 mm looks like this. It shows high speeds in the jet where present diagnostics cannot probe spectroscopically. The speeds in the ASP increase with radius, a behavior which agrees with the line-shifts seen in the experiment. Equivalent Doppler shifts are given on the right axis for comparison to the experiment.

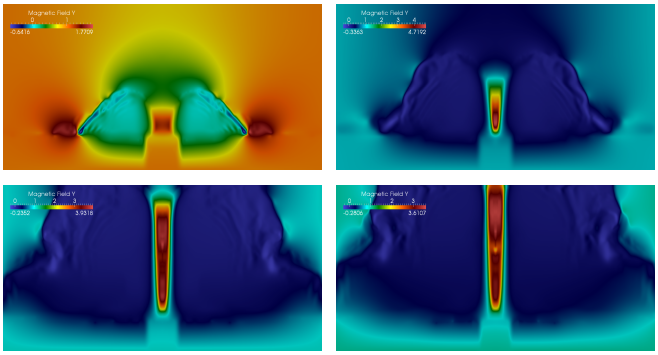

Figure 6.4: Four frames of B_z from a PERSEUS simulation with an initial imposed 1 T field show the strong compression of B_z into a funnel on axis. These images are ordered in time in a 'Z' shape, starting in the top left quadrant. The peak fields on axis approach 4 T

simulations.

CHAPTER 7

ANALYSIS

This chapter discusses some analytical methods, and digs into the physics behind the major experimental and simulation findings. Because this campaign has largely been based on experimental exploration (i.e. a random walk through parameter space), we only seek to posit plausible arguments that may explain our observations.

7.1 Methods

7.1.1 Interferometry

Inteferometric analysis methods are detailed in section 3.4.

7.1.2 Spectroscopy

Shortly before each COBRA shot, the alignment of the fiber bundle image was observed with a neon (Ne) lamp placed by the collection optics to ensure that spectra from different fibers did not overlap. These spectra were saved to provide a known-wavelength calibration for the different parts of the image on the ICCD. Then the shot data could be recorded. For analysis, the Ne lines were fitted to a Gaussian profile (due to the spectrometer) which gave spectral resolution for each fiber and each wavelength. This calibration was applied to the shot spectrum of each fiber individually. To find the line positions, Lorentzian profiles (the shape is dominated by Stark broadening) as well as a flat continuum background (reasonable because of the high resolution and small bandwidth) were fitted to these lines.

7.2 Results

We'll begin by looking at some general concepts and then use that as a launching point for seeking trends and meaning in the experimental results.

7.2.1 General Discussion

There are many variables and regimes to consider when studying plasmas. Often, by comparing parameters such as shielding length or collision frequency to scale lengths or times of interest, one can determine what physics is most responsible for the observed behavior. This section will review several plasma parameters in the context of our experiment. Much of this work will be of a graphical nature, to help elucidate the relationships between these variables. For reference, the following formulae can be found in the NRL formulary [16].

Length Scales

As a first example, let's consider the electron *Debye length* for a plasma in our experiment. We'll make a log-log plot with an x-axis of electron temperature from $0.025\,\text{eV}$ to $2.5 \times 10^3\,\text{eV}$, and a y-xais of electron number density from $10^{18}\,\text{m}^{-3}$ to $10^{28}\,\text{m}^{-3}$. The lower bounds of these ranges were chosen because they are room temperature and the high vacuum density of neutrals, respectively. The upper bounds exceed the values we expect to find in our regions of interest.

$$\lambda_D = \sqrt{\frac{\epsilon_0 k_B T_e}{q_e^2 n_e}} \approx 1.175\sqrt{\frac{\hat{T}}{\hat{n}}}\mu\text{m} \tag{7.1}$$

We've simplified Equation 7.1 by introducing nondimensional hat variables, which extend only through our parameter space of interest. (i.e. $\hat{T}$ goes from 1 to 10^5 and $\hat{n}$ goes from 1 to 10^{10}) Let's do the same for a few other variables and

plot them in Figure 7.1.

We've also included the electron mean free path, the distance we expect a thermal electron to travel before experiencing a collision event:

$$\lambda_{mfp} = \frac{v_{\text{The}}}{\nu_{ee}} = 49.22\frac{\hat{T}^2}{\hat{n}}\text{nm} \tag{7.2}$$

The electron inertial length:

$$\frac{c}{\omega_{pe}} = \frac{c}{e}\sqrt{\frac{m_e\epsilon_0}{n}} \approx 5.314\sqrt{\frac{1}{\hat{n}}}\text{mm} \tag{7.3}$$

and the cyclotron radius for a thermal electron in a $1\,$T magnetic field:

$$r_{Le} = \frac{m_e v_{\text{The}}}{eB} \approx 601.6\hat{T}\text{nm} \tag{7.4}$$

By using Figure 7.1, we can relatively quickly find orders of magnitude of these lengths for our jet ($n_e \sim 10^{25}\,\text{m}^{-3}$ and $T_e \sim 50\,\text{eV}$). They are: $\lambda_D \sim 10\,\text{nm}$, $\lambda_{mfp} \sim 30\,\text{nm}$, $\frac{c}{\omega_{pe}} \sim 1\,\mu\text{m}$, and $r_{Le} \sim 30\,\mu\text{m}$. This indicates that collisionality is very important in describing the jet.

Velocity Scales

We can do an analysis similar to the one on length scales on velocity scales. This produces a less complicated chart (see Figure 7.2) because the parameters of interest vary only on temperature or density. Electron thermal velocity and the sound speed both go up as $\sqrt{T}$, while the Alfven velocity falls as $\frac{1}{\sqrt{n}}$. This chart shows that our jets are supersonic (with Mach numbers $\sim 2-10$) and Alfven speeds are generally slow comparable to dynamics of interest.

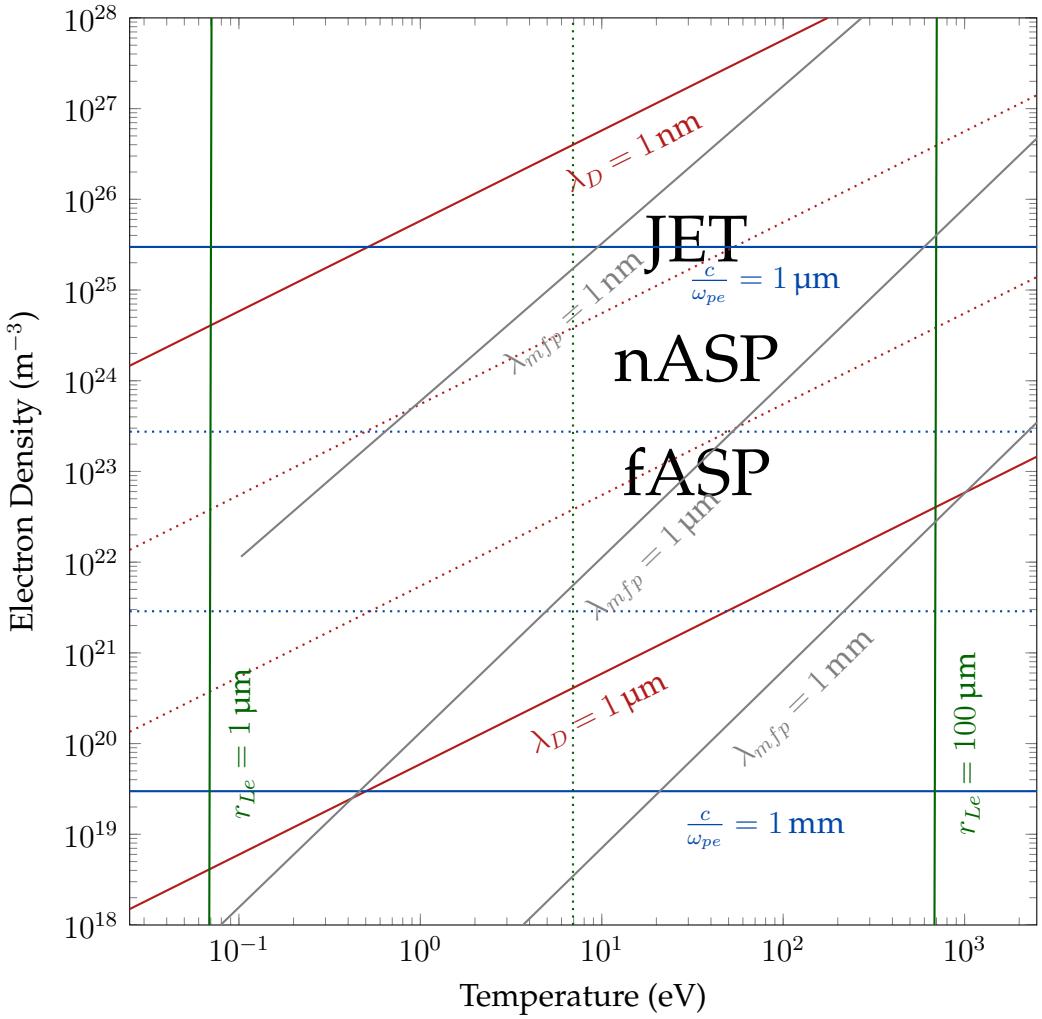

Figure 7.1: Several lengths of interest for our experiments. λ_D refers to the length scale of electron shielding of electric fields. λ_{mfp} is the electron mean-free-path, the expected distance a thermal electron will travel before a Coulomb scattering event. $\frac{c}{\omega_{pe}}$ is the electron inertial length. r_{Le} is the electron cyclotron radius for a thermal electron in a 1 T field. Increasing the field would move these lines to the right, as a stronger field leads to smaller cyclotron orbits.

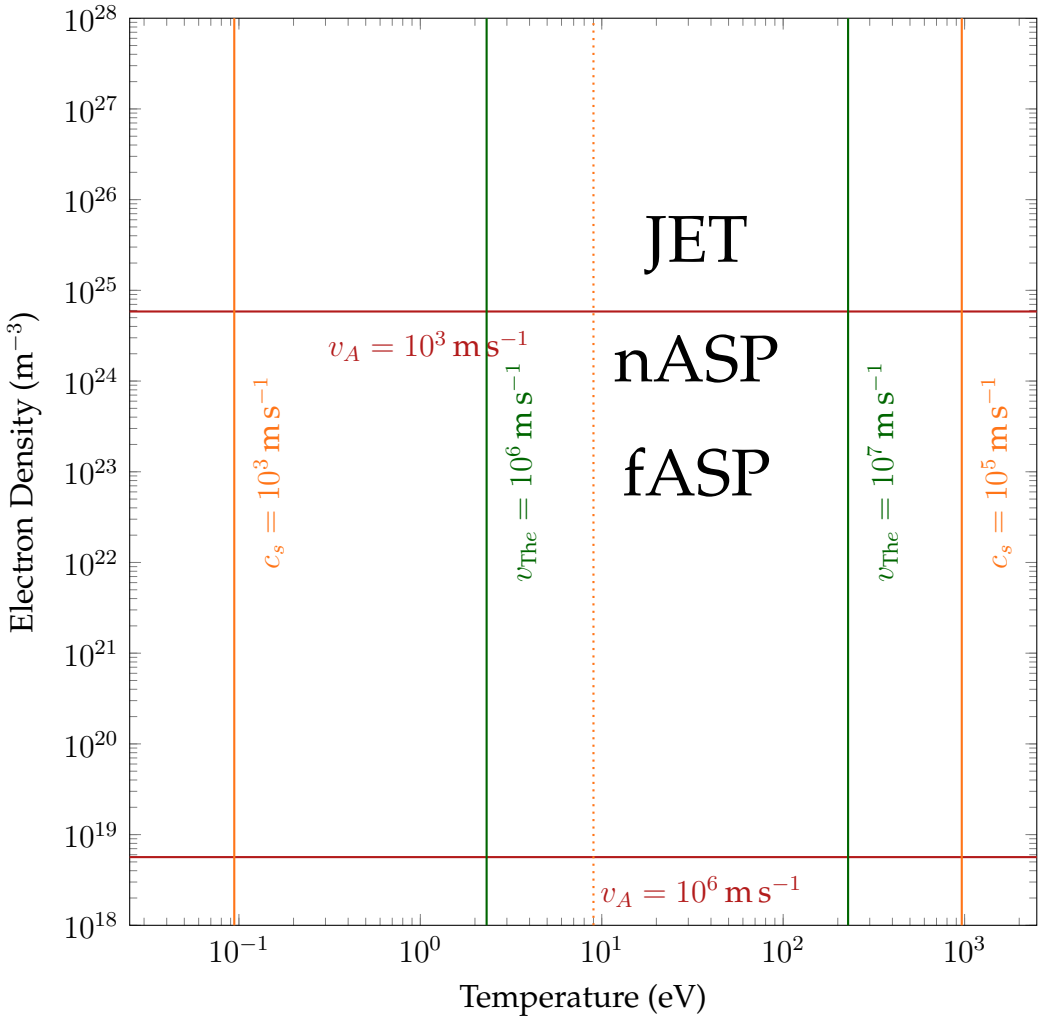

Figure 7.2: A set of velocity scales of interest plotted against temperature and electron density. We've included the electron thermal velocity v_{The}, the Alfven speed v_A for a 1 T B, and the ion-acoustic sound speed c_s. For reference, the upward expansion of the jet has been measured via laser shadowgraphy to be around $100\,\mathrm{km\,s^{-1}}$ to $300\,\mathrm{km\,s^{-1}}$. Increasing B would shift the lines for v_A upward because of the direct relationship between them.

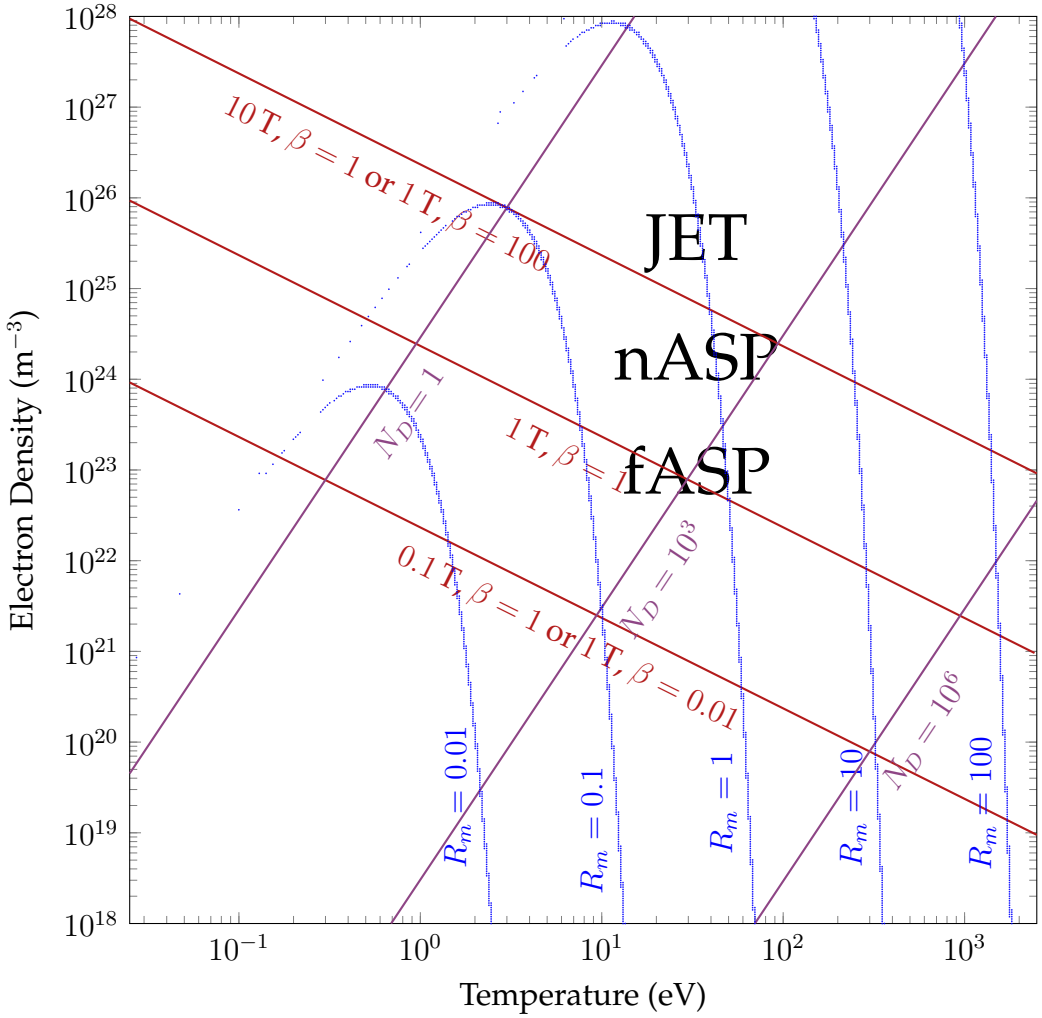

Figure 7.3: Several dimensionless numbers plotted over the log-log graph of T vs n. Plasma β, the parameter N_D and the magnetic Reynolds Number R_m are all included.

Important Dimensionless Numbers

A plasmas β is the ratio of kinetic pressure (nkT) to magnetic pressure ($\frac{B^2}{2\mu_0}$) and gives a measure of how important the magnetic field is to plasma dynamics. In low beta plasmas, magnetic forces dominate, whereas in high beta plasmas they may be negligible. Our experiment covers a wide range of plasma beta. Considering the magnetized jet, in the high density, warm jet itself, the beta is

likely quite high, while in the inner region with low density and a compressed B_z, the beta is low. Similarly we expect low beta in the low density fASP around the jet. $\beta = 1$ may correspond to the boundary of the jet.

The plasma parameter N_D, closely related to the Coulomb logarithm argument Λ, is a measure of the number of particles in a sphere with the radius λ_D. It corresponds to the coupling of the plasma over distance. Strongly coupled plasmas have few ($<< 1$) particles in a Debye sphere. Our experiment tends to stay in a weakly coupled regime ($N_D > 10^3$).

The magnetic Reynolds number ($\frac{VL\mu_0}{\eta}$) is a dimensionless parameter that expresses the ratio of magnetic advection (motion of flux with the plasma) to diffusion (having magnetic fields determined by boundary conditions as opposed to flow effects). The actual number is dependent on the selection of representative length and velocity scales. For these calculations, I've chosen $L = 1\,\mathrm{mm}$ and $U = 100\,\mathrm{km\,s^{-1}}$. R_m is related to the plasma resistivity, which depends on the collision frequency. I calculated this with the Coulomb-scattering formula given by Bellan, which includes the Coulomb logarithm. This explains the behavior of the curves of R_m in the strongly coupled regime (high density, low temperature) where that model of collisions is less applicable.

7.2.2 Tendrils

A discussion of the electrothermal instability and its relation to the present experiment continues from the introduction to radial foils found in Section 1.3. Some fraction of the machine current flows in the nASP, causing it to heat up further. At this point, the nASP follows a Spitzer-like resistivity curve ($\rho \propto T^{-3/2}$) and futher increases in temperature from this Joule heating lead to reduced resistivity and additional current draw in a positive feedback loop. The nASP

current appears to flow in one of several (∼20) discrete current paths (*tendrils*) which are created through this process of an overheating-filamentation instabilty. These tendrils expand radially and persist for long timescales (∼100 ns.) They appear to interact, with several close pairs merging over time. This supports the idea that the tendrils are channels of conductive plasma which carry some of the current that was originally in the foil. The progression of images in Figure 5.8 demonstrates that an externally imposed magnetic field deflects the tendrils in a manner consistent with the expected $\mathbf{J} \times \mathbf{B}$ force density. Because of the current carried by the tendrils, it is likely that a pinching force plays a role in their development and persistance, but their initial seeding comes from the overheating-filamentation instability.

Based on the behavior of the tendrils in the presence of the applied magnetic field, we can get an idea of the ratio of electric current density to mass density $\frac{\mathbf{J}}{\rho}$. Looking closer, we can put a range on current densities in the tendrils. In a simple model of a tube of current-carrying plasma in an external magnetic field, $\frac{\mathbf{J}}{\rho} = \frac{2x}{B\tau^2}$, where x is the distance of deflection of the tube and τ is the timescale of the motion. Looking to Figure 5.8, we'll consider the case where the outer tendrils have been wrapped around completely, so $x \sim 5$ mm and $\tau \sim 20$ ns for $B = 250$ mT. This gives $\frac{\mathbf{J}}{\rho} \sim 10^{14}$ m A kg^{-1}. We will take $\rho = m_i n_i = m_i n_e / Z$. For $n_e = 10^{24}$ m^{-3}, $m_i = 27 m_p$ for Al ions, and $Z = 3$, we calculate $J \sim 10^{12}$ A m^{-2}. This high current density is likely carried in a thin (of order 10 µm $\sim \frac{c}{\omega_{pe}}$) layer of the nASP. Coupling this dimension with the ∼1 mm width of the unperturbed tendrils gives a total current in each tendril of ∼10 kA.

Near the cathode there is a region of enhanced XUV emission, where it looks like spokes. The outer edge of this region closely corresponds to a 'boil-circle,' the region within which, according to a simple one-dimensional Ohmic heating

model, sufficient energy has been deposited into the current-carrying metal to vaporize its entire thickness. The discrete jump in emission could be related to a phase change in the foil underneath the emitting plasma. At the outer radii, where not all of the foil material has vaporized, the warm plasma loses energy due to collisions with the liquid core of the foil. Inside the 'boil-circle,' the fully-vaporized and partially-ionized foil remnant is not as strong an energy sink, and the plasma there gets warmer and emits more XUV.

7.2.3 Jet

The axial hydrodynamic ('precursor') jet has been the focus of this work. As explained in Section 1.3, the jet is formed by the inward radial force of pressure (density) gradients near the edge of the cathode. By prefilling this region with a strong B_z, we slow down the development of the jet. Some of the radially inward momentum is converted to azimuthal motion, and it is likely that currents develop as the inward plasma flow forms the conical hollow jet. Abel inverted line-outs of electron density for several heights above the foil are given in Figures 7.4 and 7.5. These show cross-sections of the unmagnetized and magnetized jets, respectively. The jet that forms in the presence of the applied $B_z \sim 1$ T is significantly hollowed on-axis. There is a drop in electron density near $r = 0$ along the axial extent of the jet. Along with this hollowing, the jet takes on an angular 'V' or conical shape as opposed to the more straight-edged cylinder it forms as in the absence of an applied B_z. This hollowing and cone-shape is intimately related to the compression of axial B_z the jet performs, addressed in Section 7.2.5.

Figure 7.6 shows the outstanding qualitative agreement between the experimental and simulation results. Caution needs to be taken with direct quantita-

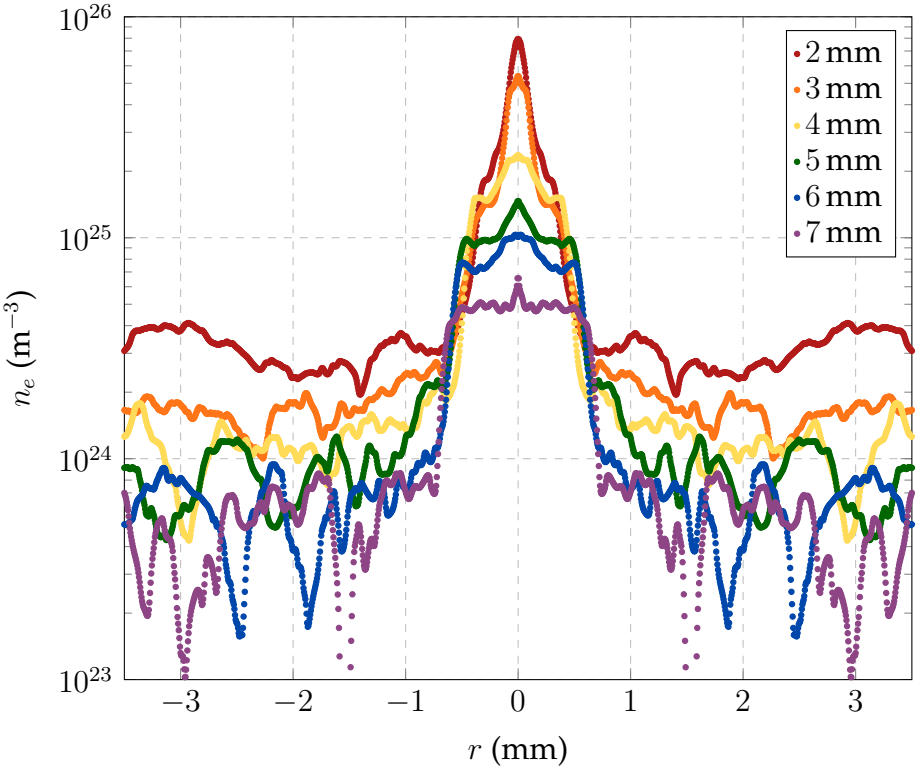

Figure 7.4: Abel-inverted (and mirrored) experimental data (showing volumetric electron density) for an exploding radial foil with no applied magnetic field. We can clearly see the edge of the jet (at about r =0.5 mm). The legend indicates the height of the line-out above the initial foil position. Absolute error analysis is difficult to accurately accomplish with Abel-inverted data because of the numerical differentiation and integration involved. Small amounts of noise tend to be exaggerated when differentiating, but the sum of many of these works to reduce this affect. Testing with synthetic data indicates the Abel-inverted data should be accurate to within 20% near the peak and within an order of magnitude at the edges. These interferograms were hand-traced, so I can confidently say the phase data (and areal electron density) are accurate to within 0.5 fringes (2.1×10^{22} m^{-2}). Because of the small effect of the sheared image (2nd 'negative' copy of jet to the lower right in the raw data), this is a lower bound of the phase data.

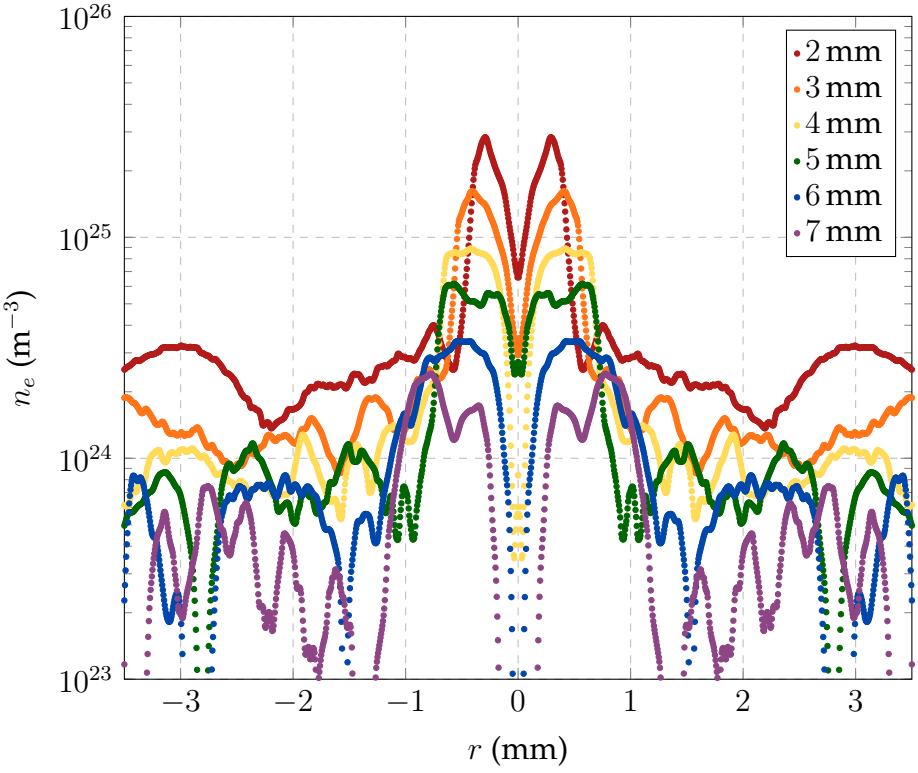

Figure 7.5: Similar to Figure 7.4, but with a 1 T applied B_z. Now there is a distinctly hollow segment on axis, and the jet has a larger radius with height above the foil.

tive comparisons, because the given simulation frame is at 120 ns after current rise versus 189 ns and 164 ns for the experimental data (refer to Fig. 5.13). In all cases, the line-out is taken 5 mm above the initial foil position.

7.2.4 Rotation

The rotation of the fASP around the jet is intuitively appreciable as a magnetic field affect similar to the washing-out of the current-carrying tendrils. It supports the notion from the simulations that there is a diffuse current density throughout the fASP bringing current into the central jet.

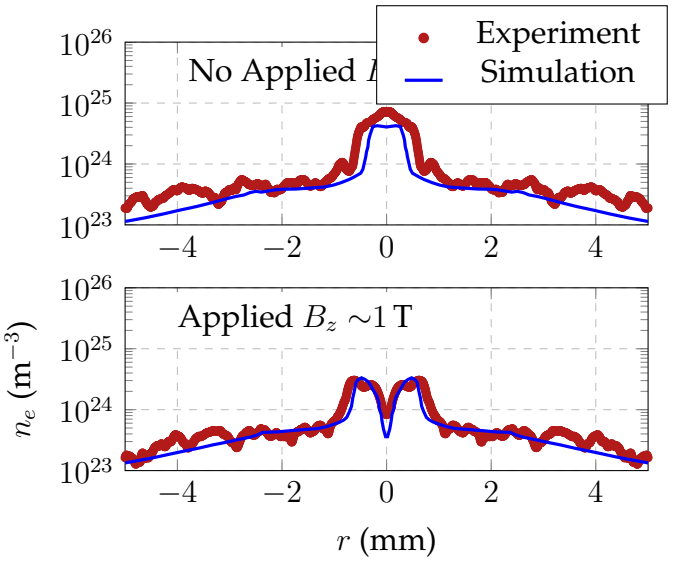

Figure 7.6: Figure showing comparison of density from experiment and simulation. $3n_i = n_e$ (blue line) from the PERSEUS simulation is plotted on top of n_e (red dots) Abel inverted from interferograms.

7.2.5 B_z Compression

Although we have not yet been able to experimentally confirm the compression of B_z, it is consistent with the rest of our results. The flow of ASP off the boiling foil advects magnetic field with it, and this field collects on the axis. This idea of flux compression can explain the conical shape of the jet, because the higher densities of ASP closer to the foil can converge to a smaller radius before the magnetic pressure dominates. B_z compression on the order of 4 times the initial field is compatible with the thought that all of the original compressed B_z flux is from the cylinder above the cathode pin ($r = 2.5$ mm) coming into the jet inner radius (~ 0.5 mm). This could be tested in simulations by looking at max B_z as a function of cathode radius.

CHAPTER 8

CONCLUSIONS

8.1 Summary of Findings

This work has explored the early ablation regime of an exploding radial foil under the influence of imposed magnetic fields. It shows that the addition of a $1\,\mathrm{T}$ field reduces assymetries due to an electrothermal filamentation instability in the current-carrying ablated plasma. The field also affects the central plasma jet, which becomes wider, more divergent, and hollowed on-axis with the applied field. A doppler shift seen with optical spectroscopy confirms the hypothesis of significant fluid rotation in the plasma surrounding the jet. These results are summarized in Fig. 8.1. XMHD computational simulations provide results in striking agreement with the experiment with regards to jet dynamics and the plasma rotation. Simulations demonstrate that a probable cause for the hollowing of the jet is a compression of the applied B_z onto the axis due to the inward flow of the ablated plasma.

Magnetic field compression is compatible with the observations of the changes in jet dynamics. The magnetized jet is hollow because the magnetic

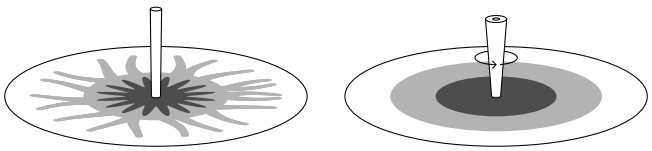

Figure 8.1: Cartoon of the jet formed by an exploding radial foil illustrating the major findings of this investigation. The jet becomes a hollow cone as it compresses the applied B_z on axis, azimuthal assymetries in the nASP become indistinct due to the azimuthal motion of current-carrying plasma. The fASP (not pictured) also takes on the same sense of rotation as the jet.

pressure of the compressed B_z excludes the ASP from the axis. The jet is conical because the higher densities closer to the foil lead to higher kinetic pressure, allowing more compression of the B_z. As this density falls off with distance from the foil, the edge of the jet moves out radially. The jet develops later in time with the applied B_z because the azimuthal velocity increases the effective distance that plasma must travel to converge on axis.

8.2 Future Work

Because this has been a largely exploratory campaign, there are many interesting directions that future work could be taken. With regards to the tendrils and the instability that appears with $B_z \sim 1.5\,\mathrm{T}$, it would be enlightening to try to create computer simulations of this behavior. XMHD simulations of the jet run in opposite polarity (COBRA current pulse radially outward instead of inward at the foil) predict a significantly wider angle of divergence, so further experiments should try to look for this. Finding this experimentally would be a strong endorsement of the necessity of Hall physics in these plasma simulations, because MHD simulations do not show the same polarity effect. Future experimental capabilities should allow for a closer study of the physics in the jet. One prime candidate is rotation, which could be measured with optical Thomson scattering. It would also be quite nice to develop a non-perturbative experimental method for determining axial B_z compression. More experimental and simulation work could look at the relationship between cathode radius (points of maximum ablation) and magnitude of B_z compression.

APPENDIX A

ABEL INVERSION METHODS

A.1 Derivation

The Abel transform/inversion pair gives a relationship between a radial function $f(r)$ and its integral along one cartesian axis $F(y)$. It is useful when dealing with physical systems with cylindrical symmetry. We usually record some data that integrates across a chord through the target. By assuming an azimuthally symmetric profile, we can recover the radial function with an Abel inversion.

A.1.1 Forward Transform

The forward Abel transform takes a function of radius, and integrates it along a straight line perpendicular to our 'detector plane.' For convenience we will take the detector plane to be parallel to the y-axis and assume our function $f(r) \to 0$ sufficiently fast for its integral to converge.

$$\int_{-\infty}^{\infty} \mathrm{d}x f(r) = 2\int_{0}^{\infty} \mathrm{d}x f(r) = 2\int_{y}^{\infty} \frac{f(r) r \mathrm{d}r}{\sqrt{r^2 - y^2}} = F(y) \tag{A.1}$$

To solve this, we took advantage of symmetry and doubled the integral over one half the integration range. Then we did a transform of variables from $x \to r$. They are related by $x^2 + y^2 = r^2$, so $\mathrm{d}x = \frac{r\mathrm{d}r}{\sqrt{r^2-y^2}}$. When $x = 0$, $r = y$ and when $x \to \mathrm{inf}$, $r \to \mathrm{inf}$.

A.1.2 Inversion

The process of inverting Equation A.1, that is to get $f(r)$ in terms of $F(y)$, is not straightforward, but it ends up working. I'll try to explain it with as much

motivation as possible.

We being by taking a derivative of $F(y)$ with respect to y. However this will lead to infinite terms if we aren't careful. So first we integrate by parts:

$$F(y) = 2\int_y^\infty \frac{f(r)r\mathrm{d}r}{\sqrt{r^2-y^2}} = 2\, f(r)\sqrt{r^2-y^2}\Big|_{r\to y}^{r\to\infty} - 2\int_y^\infty \frac{\mathrm{d}f}{\mathrm{d}r}\sqrt{r^2-y^2}\mathrm{d}r \quad \text{(A.2)}$$

The first term in the RHS drops out because we assumed $f(\infty) \to 0$ fast enough. Now we can safely differentiate with respect to y.

$$-\frac{\mathrm{d}}{\mathrm{d}y}\int_y^\infty \frac{\mathrm{d}f}{\mathrm{d}r}\sqrt{r^2-y^2}\mathrm{d}r = \frac{\mathrm{d}f}{\mathrm{d}r}\sqrt{r^2-y^2}\Big|_{r\to y} - \int_y^\infty \frac{\mathrm{d}f}{\mathrm{d}r}\frac{\partial}{\partial y}\sqrt{r^2-y^2}\mathrm{d}r \quad \text{(A.3)}$$

Again the first term of the RHS $\to 0$.

$$\frac{\mathrm{d}F}{\mathrm{d}y} = 2\int_y^\infty \frac{\mathrm{d}f}{\mathrm{d}r}\frac{y\mathrm{d}r}{\sqrt{r^2-y^2}} \quad \text{(A.4)}$$

Now comes a trick to eliminate the radical from the f integral. We start by multiplying everything by $\frac{1}{\sqrt{y^2-s^2}}$ and then apply the integral operator $\int_s^\infty \mathrm{d}y$. We bring the new integral ($\mathrm{d}y$) inside the other one ($\mathrm{d}r$) and play with bounds a bit (using Fubini's theorem). This process is illustrated in Figure A.1.

Let's define $\hat{f}$ as the result of these processes.

$$\hat{f}(s) = 2\int_s^\infty \mathrm{d}y\frac{\mathrm{d}F}{\mathrm{d}y}\frac{1}{\sqrt{y^2-s^2}} = 2\int_s^\infty \mathrm{d}y\int_y^\infty \mathrm{d}r\frac{\mathrm{d}f}{\mathrm{d}r}\frac{y}{\sqrt{r^2-y^2}\sqrt{y^2-s^2}} \quad \text{(A.5)}$$

Now we switch the order of integration:

$$\hat{f}(s) = \int_s^\infty \mathrm{d}r\frac{\mathrm{d}f}{\mathrm{d}r}\int_s^r \mathrm{d}y\frac{y}{\sqrt{r^2-y^2}\sqrt{y^2-s^2}} \quad \text{(A.6)}$$

By making the substitution $u^2 = \frac{y^2-s^2}{r^2-s^2}$, so when $y = s$, $u = 0$ and when $y = r$, $u = 1$, we can write the inner integral as the much simpler:

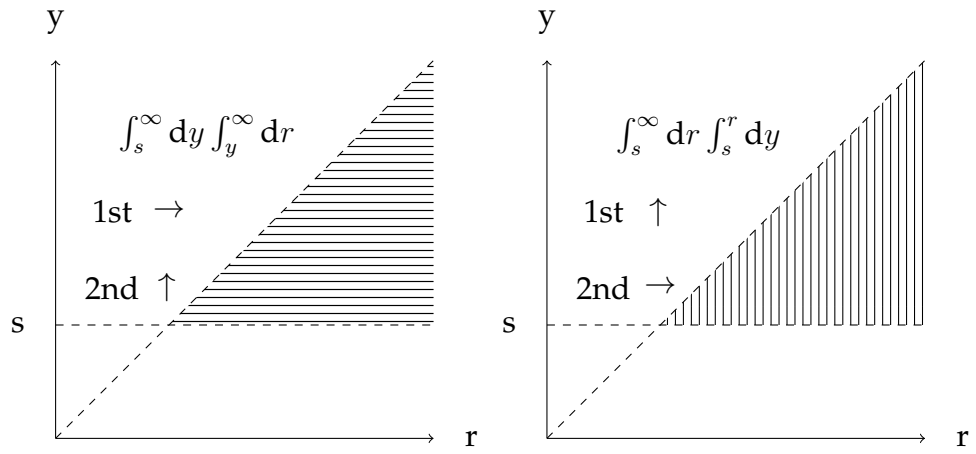

Figure A.1: Bringing one integral inside the other.

$$\int_s^r \mathrm{d}y \frac{y}{\sqrt{r^2-y^2}\sqrt{y^2-s^2}} = \int_0^1 \frac{\mathrm{d}u}{\sqrt{1-u^2}} = \frac{\pi}{2} \tag{A.7}$$

The fundamental theorem of calculus takes us the rest of the way there:

$$\hat{f}(s) = \pi \int_s^\infty \mathrm{d}r \frac{\mathrm{d}f}{\mathrm{d}r} = \pi \left(f(\infty) - f(s)\right) = -\pi f(s) \tag{A.8}$$

So our definition of $\hat{f}(s)$ was not too far off the mark! Making a small adjustment gives us:

$$f(r) = -\frac{1}{\pi} \int_r^\infty \frac{\mathrm{d}F}{\mathrm{d}y} \frac{\mathrm{d}y}{\sqrt{y^2-r^2}} \tag{A.9}$$

A.2 Numerical Implementation

We'll begin with our inverse transform integral and try to make it compatible with a discrete data set. In our discretization, we'll assume N data points, and signal which is zero for all points with a greater index.

$F(y) = 0, y > R, r_i = \frac{R}{2N}(2i+1)$

$$f(r_i) = -\frac{1}{\pi}\int_{r_i}^{R}\frac{\mathrm{d}F}{\mathrm{d}y}\frac{\mathrm{d}y}{\sqrt{y^2-r_i^2}} \tag{A.10}$$

Taking the discretized equation, we break it into a sum of integrals over each record point, as pictured in Figure A.2.

$$f_i = -\frac{1}{\pi}\sum_{n=0}^{N-1-i}\int_{\frac{R}{2N}(2i+2n+1)}^{\frac{R}{2N}(2i+2n+3)}\frac{\mathrm{d}F}{\mathrm{d}y}\frac{\mathrm{d}y}{\sqrt{y^2-\left[\frac{R}{2N}(2i+1)\right]^2}} \tag{A.11}$$

$$f_i = -\frac{1}{\pi}\sum_{n=0}^{N-1-i}F'_{i+n}\ln\left(\frac{\sqrt{\left[\frac{R}{2N}(2i+2n+3)\right]^2-\left[\frac{R}{2N}(2i+1)\right]^2}+\frac{R}{2N}(2i+2n+3)}{\sqrt{\left[\frac{R}{2N}(2i+2n+1)\right]^2-\left[\frac{R}{2N}(2i+1)\right]^2}+\frac{R}{2N}(2i+2n+1)}\right) \tag{A.12}$$

$$f_i = -\frac{1}{\pi}\sum_{n=0}^{N-1-i}F'_{i+n}\ln\left(\frac{\sqrt{(2i+2n+3)^2-(2i+1)^2}+(2i+2n+3)}{\sqrt{(2i+2n+1)^2-(2i+1)^2}+(2i+2n+1)}\right) \tag{A.13}$$

$$f_i = -\frac{1}{\pi}\sum_{n=0}^{N-1-i}F'_{i+n}\ln\left(\frac{\sqrt{n^2+2in+3n+2i+2}+(i+n+1.5)}{\sqrt{n^2+2in+n}+(i+n+0.5)}\right) \tag{A.14}$$

$$f_i = -\frac{N}{\pi L}\sum_{n=0}^{N-1-i}(F_{i+1}-F_i)\ln\left(\frac{\sqrt{n^2+2in+3n+2i+2}+(i+n+1.5)}{\sqrt{n^2+2in+n}+(i+n+0.5)}\right) \tag{A.15}$$

$$F(y) = 2\int_y^\infty\frac{f(r)r\mathrm{d}r}{\sqrt{r^2-y^2}} \tag{A.16}$$

$f(r) = 0, r > R, y_i = \frac{R}{N}i$

$$F(y_i) = 2\int_{y_i}^{R}\frac{f(r)r\mathrm{d}r}{\sqrt{r^2-\left(\frac{R}{N}i\right)^2}} \tag{A.17}$$

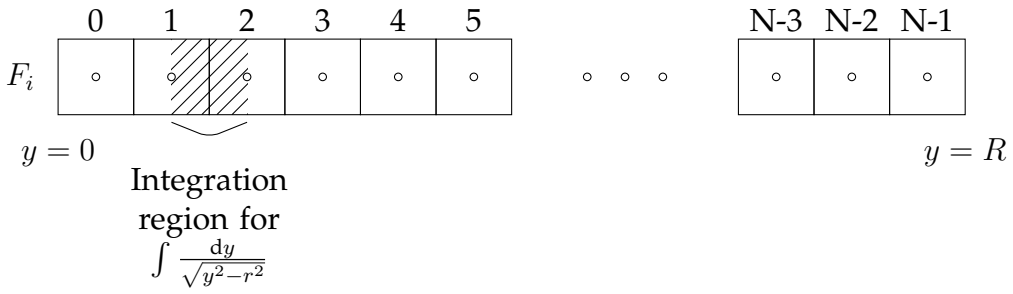

Figure A.2: Schematic for discrete Abel inversion integral

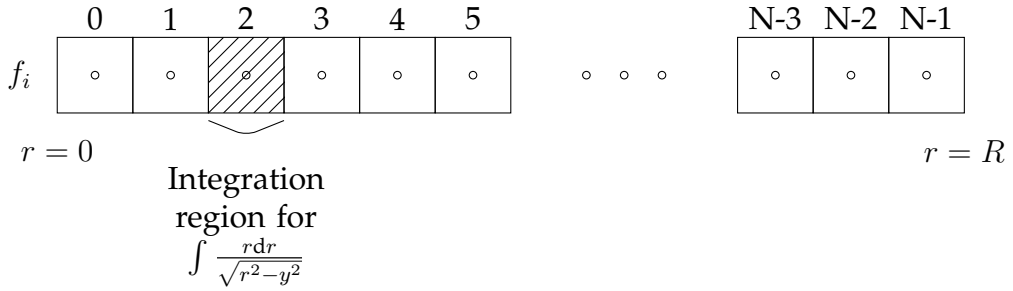

Figure A.3: Schematic for discrete forward Abel transform

$$F_i = 2 \sum_{n=0}^{N-1-i} f_{i+n} \int_{\frac{R}{N}(i+n)}^{\frac{R}{N}(i+n+1)} \frac{r\mathrm{d}r}{\sqrt{r^2 - \left(\frac{R}{N} i\right)^2}} \tag{A.18}$$

$$F_i = 2 \sum_{n=0}^{N-1-i} f_{i+n} \left[\sqrt{\left(\frac{R}{N}\right)^2 (i+n+1)^2 - \left(\frac{R}{N}\right)^2 i^2} - \sqrt{\left(\frac{R}{N}\right)^2 (i+n)^2 - \left(\frac{R}{N}\right)^2 i^2} \right] \tag{A.19}$$

$$F_i = \frac{2R}{N} \sum_{n=0}^{N-1-i} f_{i+n} \left[\sqrt{n^2 + 2n + 2i + 2in + 1} - \sqrt{n^2 + 2in} \right] \tag{A.20}$$

A.3 Python Example Inverse Abel Transform

```
from pylab import *
import numpy as np
import matplotlib.cm as cm
import matplotlib.mlab as mlab
```

```
import matplotlib.pyplot as plt
import matplotlib.image as mpimg
import sys

import random

import scipy.misc as sm

def abelInv2(Y,L):

   maxH = len(Y)
   Yprime = np.zeros(maxH)

   drI = (maxH+0.0)/L


   #calculate function derivative
   for i in xrange(0,maxH-1):
       sm1 = i-1
       sm2 = i-2
       sm3 = i-3
       sm4 = i-4
       sp1 = i+1
       sp2 = i+2
       sp3 = i+3
       sp4 = i+4

       if sm1<0:
           sm1 = np.abs(sm1)
       if sm2<0:
           sm2 = np.abs(sm2)
       if sm3<0:
           sm3 = np.abs(sm3)
       if sm4<0:
           sm4 = np.abs(sm4)

       ym1 = Y[sm1]
       ym2 = Y[sm2]
       ym3 = Y[sm3]
       ym4 = Y[sm4]

       if sp1 > maxH-2:
           yp1 = 0
       else:
           yp1= Y[sp1]

       if sp2 > maxH-2:
           yp2 = 0
       else:
           yp2= Y[sp2]

       if sp3 > maxH-2:
```

```
            yp3 = 0
        else:
            yp3= Y[sp3]

        if sp4 > maxH-2:
            yp4 = 0
        else:
            yp4= Y[sp4]

        #Yprime[i] = drI*(Y[i+1]-Y[i])
        #Yprimeb[i] = drI*((ym2-yp2)/12.0-2.0*(ym1-yp1)/3.0)
        Yprime[i] = drI*((ym4-yp4)/280.0-4.0*(ym3-yp3)/105.0#
+(ym2-yp2)/5.0-4.0*(ym1-yp1)/5.0)


    #numerical Abel inversion
    Yinv = np.zeros(maxH)
    for i in xrange(0,maxH-1):

        for n in xrange(0,maxH-i-1):

            yp = i+n+1.5
            ym = i+n+0.5
            r = i+0.5
            r1 = sqrt(yp*yp-r*r)+(yp)
            r2 = sqrt(ym*ym-r*r)+(ym)
            Yinv[i]+= Yprime[i+n]*np.log(r1/r2)

    Yinv *= -1/np.pi

    return Yinv
```

APPENDIX B

INTERFEROMETRIC ANALYSIS IMPLEMENTATION

This appendix is intended as a resource for methods of interferogram analysis. This especially covers images made with the methods described in Chapter 3, but it is generally applicable to any well-defined fringe pattern.

A scholarly literature search reveals many articles about techniques for interferogram analysis. Shortly after I began my graduate work I was introduced to the IDEA code, which includes fast Fourier transform (FFT) algorithms for image denoising and phase unwrapping. It's a useful tool, but a rather temperamental program[1] that requires significant human intervention in choosing and masking the FFT in order to process an interferogram from our experiment. After seeing some inconsistency in output data, I became wary of its results and began to seek a better method for analysis.

'Better' is a funny word in scientific analysis. My main goal was to produce a method more accurate, with good repeatability, and less reliant on difficult judgement calls by a human actor. Others may prefer something cheaper or faster that's just 'close enough.' The flowchart in Figure B.1 gives a picture of the steps required to produce quantitative data (spatially resolved electron density) from a set of interferograms on this COBRA experiment.

B.1 Work to Develop Fringe Identification

I've spent a significant amount of time thinking about the full automation of interferogram analysis (raw data to phase map) and the issues that arise. The development of such an automated technique, if generally applicable to a wide array of data and demonstrably accurate, would be a considerable achievement.

[1] look at it the wrong way and it crashes

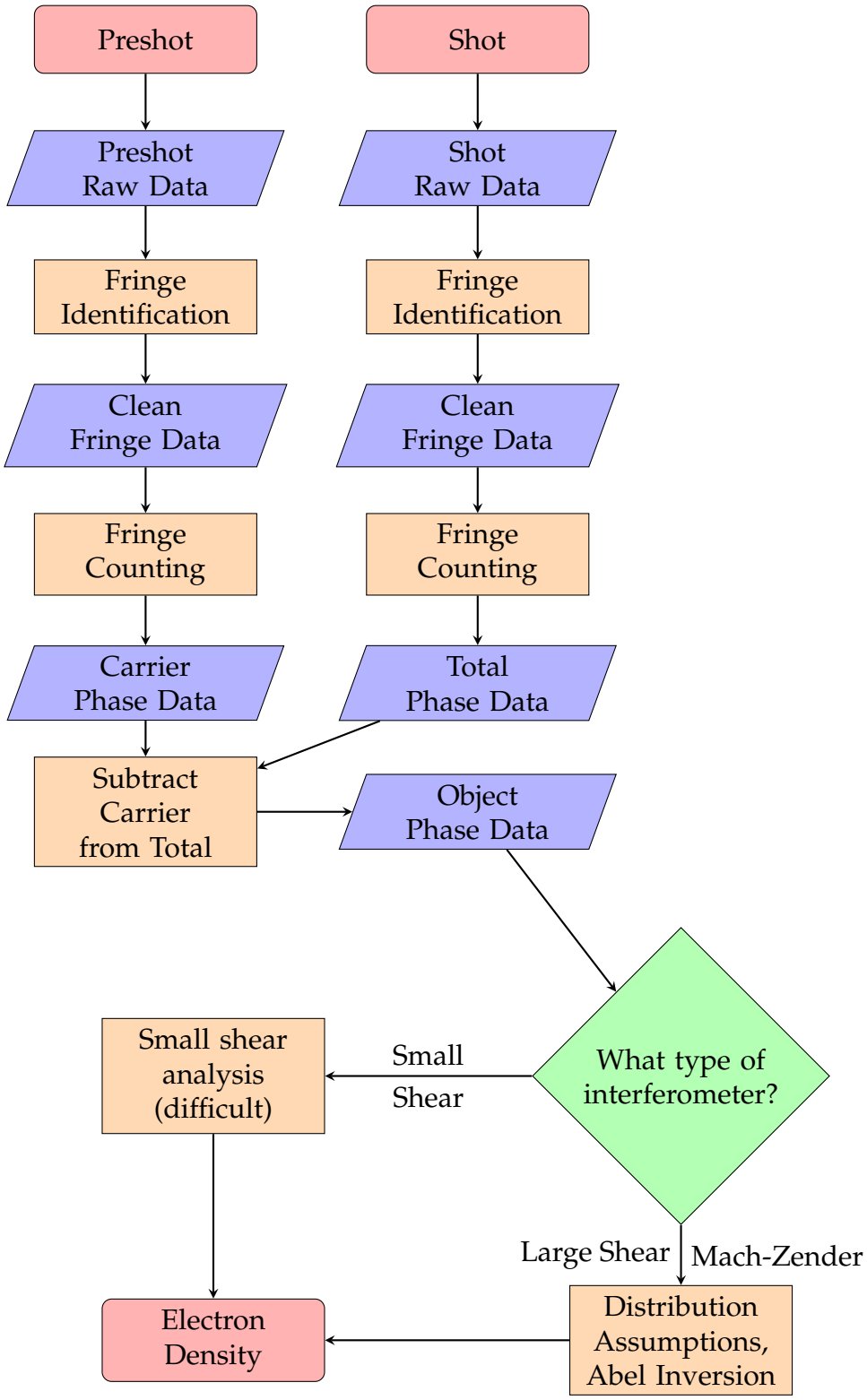

Figure B.1: Flowchart for interferogram analysis

This section explores my thoughts on the topic.

The biggest obstacle for a computerized algorithm for interferogram processing is handling noise. This comes in many varieties: the nonuniform laser beam profile which is exacerbated by dust on optical components, diffraction patterns due to sharp edges or gradients in the beam path, and extra light from self-emission of the plasma being probed. In general, these sources of noise affect the intensity profile of the recorded image in an unpredictable manner. High frequency filtering (low-pass) may allow us to attenuate or eliminate altogether th effects of dust or unwanted diffraction, but it could also modify the interference pattern we wish to recover. Similarly, low frequency filtering (high-pass) can balance out larger scale variations in intensity due to beam nonuniformity and plasma self-emission. For these reasons, interferograms processed with FFT algorithms are usually band-pass filtered over a relatively narrow band. The selection of this band, when done by a human, requires a certain amount of judgement and/or trial and error.

B.2 With a Given Frige Pattern

Probably the safest and most straight-forward (if labor-intensive) ways to identify fringes and produce a clean interference pattern is to do it by hand. This section will assume we have a 'clean' fringe pattern, i.e. a 2D array the size of our input image, with a '1' value at every point at the peak of a fringe and a '0' value everywhere else. I produced images like this by manually tracing a transparent layer over an image of the raw data in Photoshop. An advantage of this method is its resilience to the issues caused by fringe discontinuities or diffraction patterns at strong plasma gradients, IF we have chosen the carrier phase pattern appropriately.

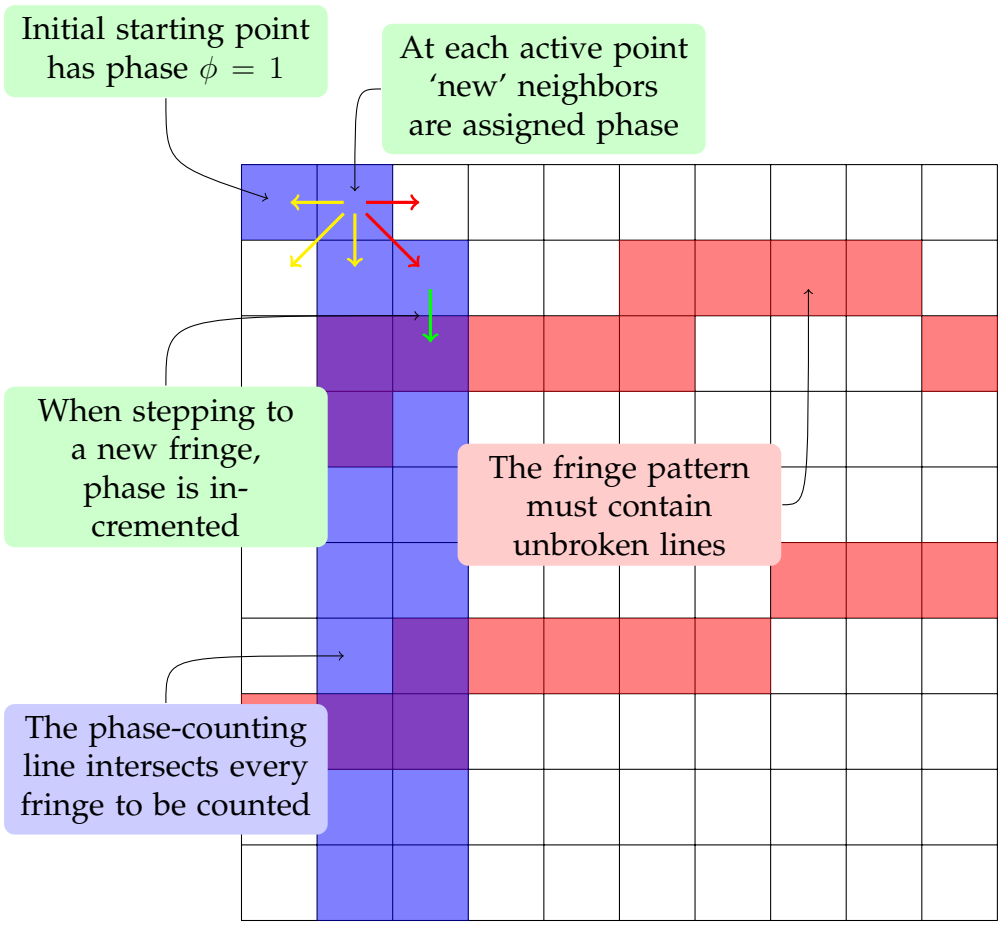

Figure B.2: Schematic of how my fringe-counting algorithm worked.

I implemented a simple fringe-counting algorithm in Python which only requires the 'clean' fringe pattern described above, and a 'counting line,' along which it will increment phase. Figure B.2 gives a pictoral description of the algorithm. Once all the fringes had been counted, I had another script to linearly interpolate phase between them. Then I smoothed this data by repeatedly averaging each point with its neighbors, except for edges and points on fringe peaks. This type of relaxation algorithm is useful and accurate when the fringe spacing is relatively tight. It reduces variations that may lead to extra noise in the numerical Abel inversion.

B.3 Python Example Fringe-Counting Algorithm

```
from pylab import *
import numpy as np
import matplotlib.cm as cm
import matplotlib.mlab as mlab
import matplotlib.pyplot as plt
import matplotlib.image as mpimg
import sys
import time

maxD = 2000

start = time.time()

FpImg=mpimg.imread('2754preshotFRINGE.png')
#FpImg=mpimg.imread('2754shotFRINGE.png')
#LiImg=mpimg.imread('line_2756.png')

print('Image loaded at', time.time()-start)

maxJ = FpImg.shape[0]
maxI = FpImg.shape[1]
print(maxJ , maxI)

#array initialization
Cr = np.zeros((maxJ,maxI),dtype=np.int)  # check this spot array
Li = np.zeros((maxJ,maxI),dtype=np.int)  # input for phase counting line
Fp = np.zeros((maxJ,maxI),dtype=np.int)  # input for fringe pattern
#Ls = np.zeros((maxD,maxD),dtype=np.int)  # setting line for phase counting
Ps = np.zeros((maxJ,maxI))  # phase setting for full image



for i in xrange(0,maxI):
   for j in xrange(0,maxJ):
       if FpImg[j,i][0]==0:
           Fp[j,i]=1
       #if LiImg[j,i][0]==0:
       #    Li[j,i]=1

Li[:,0]=1

print("Phase array initialized at ", time.time()-start)
Ch=[0,0]
Ps[0,0]=1

while len(Ch)>0:

   Ch2=[]
```

```
while len(Ch)>0:


    j = Ch.pop()
    i = Ch.pop()


    if i>0:

        ## left
        ig = i-1
        jg = j
        if (Ps[jg,ig]==0):
            if Li[jg,ig]==1:
                ## we are looking at new place on the phase line
                # we will want to check this later
                Ch2.append(ig)
                Ch2.append(jg)

                if Fp[jg,ig]==1:
                    if Fp[j,i]==0:
                        # going from no fringe to fringe- add phase!
                        Ps[jg,ig]=Ps[j,i]+1
                    else:
                        Ps[jg,ig]=Ps[j,i]
                else:
                    Ps[jg,ig]=Ps[j,i]

        if j>0:
            jg = j-1

            if (Ps[jg,ig]==0):
                if Li[jg,ig]==1:
                    ## we are looking at new place on the phase line
                    # we will want to check this later
                    Ch2.append(ig)
                    Ch2.append(jg)

                    if Fp[jg,ig]==1:
                        if Fp[j,i]==0:
                            # going from no fringe to fringe- add phase!
                            Ps[jg,ig]=Ps[j,i]+1
                        else:
                            Ps[jg,ig]=Ps[j,i]
                    else:
                        Ps[jg,ig]=Ps[j,i]

        if j<maxJ-1:
            jg = j+1

            if (Ps[jg,ig]==0):
                if Li[jg,ig]==1:
```

```
                    ## we are looking at new place on the phase line
                    # we will want to check this later
                    Ch2.append(ig)
                    Ch2.append(jg)

                    if Fp[jg,ig]==1:
                        if Fp[j,i]==0:
                            # going from no fringe to fringe- add phase!
                            Ps[jg,ig]=Ps[j,i]+1
                        else:
                            Ps[jg,ig]=Ps[j,i]
                    else:
                        Ps[jg,ig]=Ps[j,i]


if i<maxI-1:

    ## right
    ig = i+1
    jg = j
    if (Ps[jg,ig]==0):
        if Li[jg,ig]==1:
            ## we are looking at new place on the phase line
            # we will want to check this later
            Ch2.append(ig)
            Ch2.append(jg)

            if Fp[jg,ig]==1:
                if Fp[j,i]==0:
                    # going from no fringe to fringe- add phase!
                    Ps[jg,ig]=Ps[j,i]+1
                else:
                    Ps[jg,ig]=Ps[j,i]
            else:
                Ps[jg,ig]=Ps[j,i]

    if j>0:
        jg = j-1

        if (Ps[jg,ig]==0):
            if Li[jg,ig]==1:
                ## we are looking at new place on the phase line
                # we will want to check this later
                Ch2.append(ig)
                Ch2.append(jg)

                if Fp[jg,ig]==1:
                    if Fp[j,i]==0:
                        # going from no fringe to fringe- add phase!
                        Ps[jg,ig]=Ps[j,i]+1
                    else:
                        Ps[jg,ig]=Ps[j,i]
```

```
                else:
                    Ps[jg,ig]=Ps[j,i]

    if j<maxJ-1:
        jg = j+1

        if (Ps[jg,ig]==0):
            if Li[jg,ig]==1:
                ## we are looking at new place on the phase line
                # we will want to check this later
                Ch2.append(ig)
                Ch2.append(jg)

                if Fp[jg,ig]==1:
                    if Fp[j,i]==0:
                        # going from no fringe to fringe- add phase!
                        Ps[jg,ig]=Ps[j,i]+1
                    else:
                        Ps[jg,ig]=Ps[j,i]
                else:
                    Ps[jg,ig]=Ps[j,i]



if j>0:
    ig = i
    jg = j-1

    if (Ps[jg,ig]==0):
        if Li[jg,ig]==1:
            ## we are looking at new place on the phase line
            # we will want to check this later
            Ch2.append(ig)
            Ch2.append(jg)

            if Fp[jg,ig]==1:
                if Fp[j,i]==0:
                    # going from no fringe to fringe- add phase!
                    Ps[jg,ig]=Ps[j,i]+1
                else:
                    Ps[jg,ig]=Ps[j,i]
            else:
                Ps[jg,ig]=Ps[j,i]

if j<maxJ-1:
    ig = i
    jg = j+1

    if (Ps[jg,ig]==0):
        if Li[jg,ig]==1:
            ## we are looking at new place on the phase line
            # we will want to check this later
```

```
                    Ch2.append(ig)
                    Ch2.append(jg)

                    if Fp[jg,ig]==1:
                        if Fp[j,i]==0:
                            # going from no fringe to fringe- add phase!
                            Ps[jg,ig]=Ps[j,i]+1
                        else:
                            Ps[jg,ig]=Ps[j,i]
                    else:
                        Ps[jg,ig]=Ps[j,i]



   Ch = list(Ch2)

print("phase line trace complete at ", time.time()-start)
## Begin Step 2

#Ch[0,0]=1
#Ps[0,0]=1
count=0


for i in xrange(0,maxI):
   for j in xrange(0,maxJ):
       if Ps[j,i]>0:
           Cr[j,i]=1
           Ch.append(i)
           Ch.append(j)

#Ps[250,250]=1
#Cr[250,250]=1
#Ch = [250,250]


while len(Ch)>0:

   Ch2=[]

   while len(Ch)>0:


       j = Ch.pop()
       i = Ch.pop()



       if i>0:

           ## left
```

```
    ig = i-1
    jg = j

    if Ps[jg,ig]==0:

        #otherwise we'll copy like to like:
        if Fp[j,i]==Fp[jg,ig]:
            Ps[jg,ig] = Ps[j,i]

        if Ps[jg,ig]>0:
            if Cr[jg,ig]==0:
                Ch2.append(ig)
                Ch2.append(jg)
                Cr[jg,ig]=1

    if j>0:
        jg = j-1

        if Ps[jg,ig]==0:

            #otherwise we'll copy like to like:
            if Fp[j,i]==Fp[jg,ig]:
                if Fp[j,i]==1:
                    Ps[jg,ig] = Ps[j,i]

            if Ps[jg,ig]>0:
                if Cr[jg,ig]==0:
                    Ch2.append(ig)
                    Ch2.append(jg)
                    Cr[jg,ig]=1

    if j<maxJ-1:
        jg = j+1

        if Ps[jg,ig]==0:

            #copy like to like:
            if Fp[j,i]==Fp[jg,ig]:
                if Fp[j,i]==1:
                    Ps[jg,ig] = Ps[j,i]

            if Ps[jg,ig]>0:
                if Cr[jg,ig]==0:
                    Ch2.append(ig)
                    Ch2.append(jg)
                    Cr[jg,ig]=1


if i<maxI-1:

    ## right
    ig = i+1
```

```
    jg = j
    if Ps[jg,ig]==0:

        #copy like to like:
        if Fp[j,i]==Fp[jg,ig]:
            Ps[jg,ig] = Ps[j,i]

        if Ps[jg,ig]>0:
            if Cr[jg,ig]==0:
                Ch2.append(ig)
                Ch2.append(jg)
                Cr[jg,ig]=1

    if j>0:
        jg = j-1

        if Ps[jg,ig]==0:

            #copy like to like:
            if Fp[j,i]==Fp[jg,ig]:
                if Fp[j,i]==1:
                    Ps[jg,ig] = Ps[j,i]

            if Ps[jg,ig]>0:
                if Cr[jg,ig]==0:
                    Ch2.append(ig)
                    Ch2.append(jg)
                    Cr[jg,ig]=1

    if j<maxJ-1:
        jg = j+1

        if Ps[jg,ig]==0:

            #copy like to like:
            if Fp[j,i]==Fp[jg,ig]:
                if Fp[j,i]==1:
                    Ps[jg,ig] = Ps[j,i]

            if Ps[jg,ig]>0:
                if Cr[jg,ig]==0:
                    Ch2.append(ig)
                    Ch2.append(jg)
                    Cr[jg,ig]=1



if j>0:
    ig = i
    jg = j-1

    if Ps[jg,ig]==0:
```

```
                #copy like to like:
                if Fp[j,i]==Fp[jg,ig]:
                    Ps[jg,ig] = Ps[j,i]

                if Ps[jg,ig]>0:
                    if Cr[jg,ig]==0:
                        Ch2.append(ig)
                        Ch2.append(jg)
                        Cr[jg,ig]=1

        if j<maxJ-1:
            ig = i
            jg = j+1

            if Ps[jg,ig]==0:

                #copy like to like:
                if Fp[j,i]==Fp[jg,ig]:
                    Ps[jg,ig] = Ps[j,i]

                if Ps[jg,ig]>0:
                    if Cr[jg,ig]==0:
                        Ch2.append(ig)
                        Ch2.append(jg)
                        Cr[jg,ig]=1



   Ch = list(Ch2)

   #for i in xrange(0,maxI):
   #    for j in xrange(0,maxJ):
   #        Cr[j,i]=0
   #        #Ps[j,i]=Ps[j,i]
   #        if Ps[j,i]>0:
   #            Cr[j,i]=1
   #            #Ch.append(i)
   #            #Ch.append(j)

   count+=1

   if count>(maxI+maxJ):
       break


##
print("initial phase filling complete at ", time.time()-start)
## run down the verticals to interpolate phase

for i in xrange(0,maxI):
   phi=1
```

```
    jOld = 0
    for j in xrange(0,maxJ):

        if Fp[j,i]==1:

            m = 1.0*(Ps[j,i]-Ps[jOld,i])/(j-jOld)
            for k in xrange(0,j-jOld):
                Ps[k+jOld,i]= Ps[jOld,i]+k*m

            jOld = j


print("vertical phase interpolation complete at ", time.time()-start)


for k in xrange(0,15):
    for i in xrange(1,maxI-1):
        for j in xrange(1,maxJ-1):
            if Fp[j,i]!=1:
                Ps[j,i]= 0.25*(Ps[j,i+1]+Ps[j,i-1]+Ps[j+1,i]+Ps[j-1,i])
    print("phase relaxation ",k, " at ", time.time()-start)


for k in xrange(0,2):
    for i in xrange(1,maxI-1):
        for j in xrange(1,maxJ-1):
            Ps[j,i]= 0.25*(Ps[j,i+1]+Ps[j,i-1]+Ps[j+1,i]+Ps[j-1,i])
    print("phase relaxationB ",k, " at ", time.time()-start)

print("phase relaxation complete at ", time.time()-start)



np.savetxt('phasepreShot2754.txt',Ps)
#np.savetxt('phaseShot2754.txt',Ps)

im = plt.imshow(Ps, cmap=cm.gray)
plt.colorbar()
plt.show()
```

B.4 Discussion of Small-Shear Analysis

For this section, we will assume the fringe pattern has already been processed to give numerical phase data. This is of the form $\Phi(x,y) = \phi(x,y) - \phi(x+\delta_x, y+\delta_y)$, we know Φ and wish to know ϕ. The δs are due to the lateral shear of one image

versus another. To simplify things, we can rotate the image to put the shear along one axis. Considering a function of one variable, and symmetrizing the shift, let's write:

$$g(x) = f(x + \frac{\delta}{2}) - f(x - \frac{\delta}{2}) \tag{B.1}$$

Now we can Fourier transform this equation to get:

$$G(k) = F(k)\mathrm{e}^{2\pi \mathrm{i} kx} - F(k)\mathrm{e}^{-2\pi \mathrm{i} kx} = 2\mathrm{i}\sin(2\pi \mathrm{i} kx)\, F(k) \tag{B.2}$$

So therefore:

$$F(k) = \frac{G(k)}{2\mathrm{i}\sin(2\pi \mathrm{i} kx)} \tag{B.3}$$

If we can find the inverse Fourier transform of F(k), we have recovered our desired f. Equation B.3 looks to be dangerous when trying to implement discrete methods for doing this with numerical inputs. In a DFT, this $\sin$ term will have $\frac{kn}{N}$ with integer k, n running up to $N-1$. By choosing a prime record length N, we can avoid dividing by zero in the discrete analogue of Equation B.3.

BIBLIOGRAPHY

[1] D. J. Ampleford, S. V. Lebedev, S. N. Bland, S. C. Bott, J. P. Chittenden, C. A. Jennings, V. L. Kantsyrev, A. S. Safronova, V. V. Ivanov, D. A. Fedin, P. J. Laca, M. F. Yilmaz, V. Nalajala, I. Shrestha, K. Williamson, G. Osborne, A. Haboub, and A. Ciardi. Dynamics of conical wire array z-pinch implosions. *Physics of Plasmas*, 14(10):102704–102704–13, October 2007.

[2] General Atomics. *High Energy Density Capacitors*, 2014 (accessed April 28, 2014). `http://www.ga.com/high-energy-density-capacitors`.

[3] Paul Murray Bellan. *Fundamentals of plasma physics*. Cambridge University Press, Cambridge; New York, 2008.

[4] Francis F Chen. *Introduction to plasma physics and controlled fusion. 1. Plasma physics.* Plemum Pr., New York u.a., 2nd edition, 1984.

[5] P. D. Desai, H. M. James, and C. Y. Ho. Electrical resistivity of aluminum and manganese. *Journal of Physical and Chemical Reference Data*, 13(4):1131–1172, October 1984.

[6] R. P. Drake. Perspectives on high-energy-density physics. *Physics of Plasmas*, 16(5):055501–055501–7, March 2009.

[7] Falize, S. Bouquet, and C. Michaut. Radiation hydrodynamics scaling laws in high energy density physics and laboratory astrophysics. *Journal of Physics: Conference Series*, 112(4):042016, May 2008.

[8] Falize, C. Michaut, and S. Bouquet. Similarity properties and scaling laws of radiation hydrodynamic flows in laboratory astrophysics. *The Astrophysical Journal*, 730(2):96, April 2011.

[9] P.-A. Gourdain, I. C. Blesener, J. B. Greenly, D. A. Hammer, P. F. Knapp, B. R. Kusse, S. A. Pikuz, and T. C. Shelkovenko. High energy density plasmas generated by radial foil explosions. *Plasma Physics and Controlled Fusion*, 52(5):055015, May 2010.

[10] P.-A. Gourdain, I. C. Blesener, J. B. Greenly, D. A. Hammer, P. F. Knapp, B. R. Kusse, and P. C. Schrafel. Initial experiments using radial foils on the cornell beam research accelerator pulsed power generator. *Physics of Plasmas*, 17(1):012706–012706–7, January 2010.

[11] P.-A. Gourdain, J. B. Greenly, D. A. Hammer, B. R. Kusse, S. A. Pikuz, C. E. Seyler, T. C. Shelkovenko, and P. F. Knapp. Magnetohydrodynamic instabilities in radial foil configurations. *Physics of Plasmas*, 19(2):022701–022701–6, February 2012.

[12] P.-A. Gourdain, J.B. Greenly, D.A. Hammer, P. F. Knapp, B. R. Kusse, S.A. Pikuz, P.C. Schrafel, and T.C. Shelkovenko. The impact of cathode diameter on radial foil explosions. *IEEE Transactions on Plasma Science*, 38(12):3363–3369, 2010.

[13] P.-A. Gourdain and C. E. Seyler. Impact of the hall effect on high-energy-density plasma jets. *Physical Review Letters*, 110(1):015002, January 2013.

[14] J. B. Greenly, J. D. Douglas, D. A. Hammer, B. R. Kusse, S. C. Glidden, and H. D. Sanders. A 1MA, variable risetime pulse generator for high energy density plasma research. *Review of Scientific Instruments*, 79(7):073501–073501–5, July 2008.

[15] C. D. Gregory, J. Howe, B. Loupias, S. Myers, M. M. Notley, Y. Sakawa, A. Oya, R. Kodama, M. Koenig, and N. C. Woolsey. Astrophysical jet experiments with colliding laser-produced plasmas. *The Astrophysical Journal*, 676(1):420, March 2008.

[16] J. D. Huba. NRL plasma formulary. Naval Research Laboratory, Washington, D.C., 2013.

[17] John David Jackson. *Classical Electrodynamics*. Wiley, 1999.

[18] S. V. Lebedev, A. Ciardi, D. J. Ampleford, S. N. Bland, S. C. Bott, J. P. Chittenden, G. N. Hall, J. Rapley, C. A. Jennings, A. Frank, E. G. Blackman, and T. Lery. Magnetic tower outflows from a radial wire array z-pinch. *Monthly Notices of the Royal Astronomical Society*, 361(1):97–108, July 2005.

[19] Matthew Martin. *Generalized Ohm'S Law At The Plasma-Vacuum Interface*. PhD thesis, Cornell University, August 2010. 2015-08-05.

[20] J. Clerk Maxwell. A dynamical theory of the electromagnetic field. *Philosophical Transactions of the Royal Society of London*, 155:459–512, January 1865.

[21] L. L. McCready, J. L. Pawsey, and Ruby Payne-Scott. Solar radiation at radio frequencies and its relation to sunspots. *Proceedings of the Royal Society*

of London. Series A. Mathematical and Physical Sciences, 190(1022):357–375, August 1947.

[22] Kyle J. Peterson, Daniel B. Sinars, Edmund P. Yu, Mark C. Herrmann, Michael E. Cuneo, Stephen A. Slutz, Ian C. Smith, Briggs W. Atherton, Marcus D. Knudson, and Charles Nakhleh. Electrothermal instability growth in magnetically driven pulsed power liners. *Physics of Plasmas*, 19(9):092701–092701–15, September 2012.

[23] S. A. Pikuz, V. M. Romanova, N. V. Baryshnikov, Min Hu, B. R. Kusse, D. B. Sinars, T. A. Shelkovenko, and D. A. Hammer. A simple air wedge shearing interferometer for studying exploding wires. *Review of Scientific Instruments*, 72(1):1098–1100, January 2001.

[24] S. A. Pikuz, P. C. Schrafel, T. A. Shelkovenko, and B. R. Kusse. A torquing shearing interferometer for cylindrical wire array experiments. *Review of Scientific Instruments*, 79(10):10E716–10E716–3, October 2008.

[25] LC Robinson and LE Sharp. Microwave interferometry for plasma studies. *Australian Journal of Physics*, 16(3):439–446, January 1963.

[26] D. D. Ryutov, M. S. Derzon, and M. K. Matzen. The physics of fast z pinches. *Reviews of Modern Physics*, 72(1):167–223, January 2000.

[27] D. D. Ryutov, N. L. Kugland, H. S. Park, C. Plechaty, B. A. Remington, and J. S. Ross. Basic scalings for collisionless-shock experiments in a plasma without pre-imposed magnetic field. *Plasma Physics and Controlled Fusion*, 54(10):105021, October 2012.

[28] D. D. Ryutov, B. A. Remington, H. F. Robey, and R. P. Drake. Magnetohydrodynamic scaling: From astrophysics to the laboratory. *Physics of Plasmas*, 8(5):1804–1816, May 2001.

[29] Peter C Schrafel. Visible laser interferometry for density measurements of exploding wire and wire array plasmas with experiments on lcp-3 and cobra. Undergraduate honors thesis, 2008.

[30] C. E. Seyler and M. R. Martin. Relaxation model for extended magnetohydrodynamics: Comparison to magnetohydrodynamics for dense z-pinches. *Physics of Plasmas*, 18(1):012703–012703–13, January 2011.

[31] S. A. Slutz, M. C. Herrmann, R. A. Vesey, A. B. Sefkow, D. B. Sinars, D. C.

Rovang, K. J. Peterson, and M. E. Cuneo. Pulsed-power-driven cylindrical liner implosions of laser preheated fuel magnetized with an axial field. *Physics of Plasmas*, 17(5):056303–056303–15, March 2010.

[32] F. Suzuki-Vidal, S. V. Lebedev, A. Ciardi, S. N. Bland, J. P. Chittenden, G. N. Hall, A. Harvey-Thompson, A. Marocchino, C. Ning, C. Stehle, A. Frank, E. G. Blackman, S. C. Bott, and T. Ray. Formation of episodic magnetically driven radiatively cooled plasma jets in the laboratory. *Astrophysics and Space Science*, 322(1-4):19–23, August 2009.

[33] F. Suzuki-Vidal, S. V. Lebedev, M. Krishnan, J. Skidmore, G. F. Swadling, M. Bocchi, A. J. Harvey-Thompson, S. Patankar, G. C. Burdiak, P. de Grouchy, L. Pickworth, S. J. P. Stafford, L. Suttle, M. Bennett, S. N. Bland, J. P. Chittenden, G. N. Hall, E. Khoory, R. A. Smith, A. Ciardi, A. Frank, R. E. Madden, K. Wilson-Elliot, and P. Coleman. Interaction of radiatively cooled plasma jets with neutral gases forlaboratory astrophysics studies. *High Energy Density Physics*, 9(1):141–147, March 2013.

[34] F. Suzuki-Vidal, S.V. Lebedev, S.N. Bland, G.N. Hall, A.J. Harvey-Thompson, J.P. Chittenden, A. Marocchino, S.C. Bott, J. Palmer, and A. Ciardi. Effect of wire diameter and addition of an axial magnetic field on the dynamics of radial wire array -pinches. *IEEE Transactions on Plasma Science*, 38(4):581–588, April 2010.

[35] Francisco Suzuki-Vidal, Sergey V. Lebedev, Simon N. Bland, Gareth N. Hall, George Swadling, Adam J. Harvey-Thompson, Jeremy P. Chittenden, Alberto Marocchino, Andrea Ciardi, Adam Frank, Eric G. Blackman, and Simon C. Bott. Generation of episodic magnetically driven plasma jets in a radial foil z-pinch. *Physics of Plasmas*, 17(11):112708–112708–11, November 2010.

[36] V. T. Tikhonchuk, Ph Nicola, X. Ribeyre, C. Stenz, G. Schurtz, A. Kasperczuk, T. Pisarczyk, L. Juha, E. Krousky, K. Masek, M. Pfeifer, K. Rohlena, J. Skala, J. Ullschmied, M. Kalal, D. Klir, J. Kravarik, P. Kubes, and P. Pisarczyk. Laboratory modeling of supersonic radiative jets propagation in plasmas and their scaling to astrophysical conditions. *Plasma Physics and Controlled Fusion*, 50(12):124056, December 2008.